Exploring Tumor-Associated Macrophage Heterogeneity and Their Responses to MEK Inhibition in Pancreatic Ductal Adenocarcinoma

Inaugural-Dissertation

zur

Erlangung des Doktorgrades

Dr. rer. nat.

der Fakultät für

Biologie

an der

Universität Duisburg-Essen

vorgelegt von

Christian Neander

aus Ratingen

am 03.02.2020

Die der vorliegenden Arbeit zugrundeliegenden Experimente wurden am Brückeninstitut für Experimentelle Tumortherapie & Abteilung für Translationale Onkologie Solider Tumore (DKFZ/DKTK Partnerstandort Essen) der Universität Duisburg-Essen oder an einer anderen gleichwertigen Einrichtung durchgeführt.

1.Gutachter:

2.Gutachter:

3.Gutachter:

Vorsitzender des Prüfungsausschusses:

Tag der mündlichen Prüfung:

Abstract

Pancreatic ductal adenocarcinoma (PDAC) is a highly aggressive tumor entity, which is routinely treated with gemcitabine-based chemotherapy. However, patient overall survival remains poor due to frequently occuring therapy resistance, reflecting the urgent need for identification of new treatment targets. In light of this, clinical trials started to investigate MEK inhibitors (MEKi), since the vast majority of PDAC patients harbor oncogenic *KRAS* mutation. Recently, PDAC tumors were molecularly stratified into two different tumor subtypes, epithelial and mesenchymal, with the latter being more aggressive and demonstrating worse prognosis and survival. Besides, there are emerging studies focusing not only on cell-autonomous tumor cell characteristics, but also on tumor-stroma interactions for tumor progression and therapy resistance. Tumor-associated macrophages (TAMs) are the predominant immune cell infiltrate within the highly immunosuppressive pancreatic tumor microenvironment (TME) and are involved in a multitude of pro-tumorigenic and immunosuppressive mechanisms, making them a promising target for anti-cancer therapy. Furthermore, TAMs display high heterogeneity and plasticity in terms of pro- and anti-inflammatory phenotypes upon various stimuli in the TME. Despite increasing advances made in our understanding of this disease, the effects of MEK inhibition on TAMs as well as the effects of different PDAC subtypes on macrophage phenotypes are largely unknown. This work aimed at investigating the effects of MEK inhibition on the TME of different PDAC subtypes with particular focus on macrophages and at the exploring tumor subtype-specific TAM heterogeneity.

To investigate the effects of MEK inhibition on different macrophage phenotypes, pro-inflammatory M1-like, anti-inflammatory M2-like and unstimulated M0 macrophages were induced *in vitro* from mouse bone marrow. *In vitro* examination revealed no de-/ repolarization of macrophages upon MEKi treatment. Anti-inflammatory M2-like macrophages showed a higher sensitivity to MEKi, while pro-inflammatory M1-like macrophages were less sensitive to MEKi-induced cell death. Metabolic flux analysis revealed that MEKi reduced M2-like macrophage-associated oxidative phosphorylation, but less so in the other macrophage subsets.

For the examination of tumor subtype-specific TAM heterogeneity and potential TAM phenotype-specific effects of MEKi, TAMs were induced by culturing with tumor-conditioned medium (TCM) from different epithelial (epiTAMs) or mesenchymal (mesTAMs) PDAC cells. TAM heterogeneity was analyzed on transcriptomic, metabolic and immunophenotypic levels. Following TCM stimulation, epiTAMs and mesTAMs showed metabolic adaptation with increased oxidative phosphorylation and decreased glycolytic rates, but could not be classified based on phenotypic marker expression of classical M1 and M2 macrophage marker proteins. Transcriptomic analysis of epiTAMs and mesTAMs

revealed differential gene expression with epiTAMs showing enrichment of interferon-gamma response. In comparison, mesTAMs were enriched in a gene set associated with hypoxia, however, epiTAMs and mesTAMs showed no tumor subtype-specific difference in hypoxia-inducible factor 1A (HIF1A) signaling induction after TCM stimulation. Furthermore, mesTAMs were shown to be more sensitive to MEKi-induced cell death in comparison to epiTAMs and *in vivo* analysis of MEKi-treated spontaneous PDAC mouse model (*CKP*) showed macrophage depletion in tumors upon MEKi treatment.

In summary, this work shows that TAMs polarized with TCM from different PDAC subtypes could not be distinguished by conventional M1 and M2 macrophage markers, supporting the existence of a continuous spectrum of TAMs with a mixture of pro- and anti-inflammatory phenotypes, depending on the context, such as stimuli and signals, from the tumor microenvironment. Instead, they showed subtype-related dependency of MAPK signaling. Furthermore, it was demonstrated that trametinib-mediated MEK inhibition had macrophage phenotype-specific effects *in vitro* and induced cell death of tumor-associated macrophages in a PDAC mouse model, thereby reducing the immunosuppressive microenvironment, which potentially opens an avenue for combinatorial treatment regimens of MEK inhibition and immunotherapy-based approaches.

Zusammenfassung

Das duktale Pankreaskarzinom (PDAC) ist eine aggressive Tumorentität, welche standardmäßig chemotherapeutisch behandelt wird. Aufgrund der nahezu immer auftretenden Therapieresistenz haben PDAC-Patienten eine geringe Überlebensdauer, weshalb ein dringender Bedarf für die Entwicklung neuartiger therapeutischer Interventionsmöglichkeiten besteht. Vor diesem Hintergrund wurden MEK-Inhibitoren in klinischen Studien als potentielle Therapie-Option analysiert, da die Mehrheit der PDAC-Patienten eine onkogene *KRAS*-Mutation aufweist. Transkriptomisch lassen sich duktale Pankreaskarzinome in zwei unterschiedliche Tumor-Subtypen gruppieren, klassische und quasi-mesenchymale Tumoren, wobei letztere mit einer aggressiveren Tumorprogression und einer schlechteren Prognose für die betroffenen Patienten assoziiert sind. Aktuelle Strategien fokussieren sich jedoch nicht ausschließlich nur auf die Zell-autonomen Eigenschaften der Tumorzellen, sondern heben ebenfalls die Bedeutung der Tumor-Stroma Interaktion für Tumorprogression und Therapieresistenz-Bildung hervor. Innerhalb des immunsuppressiven PDAC-Mikromilieus stellen Tumor-assoziierte Makrophagen (TAMs) den Hauptanteil der Tumor-infiltrierenden Immunzellen dar. TAMs können den Tumor durch eine Vielzahl pro-tumorigener und immunsuppressiver Mechanismen unterstützen und stellen deshalb ein vielversprechendes neues Therapieziel dar. Darüber hinaus zeigen TAMs eine hohe Heterogenität und Plastizität in Bezug auf pro- und anti-inflammatorische Phänotypen als Antwort auf verschiedene Stimuli innerhalb des Tumor-Mikromilieus. Trotz eines verbesserten Verständnisses dieser malignen Erkrankung sind die Effekte von MEK-Inhibitoren auf TAMs im duktalen Pankreaskarzinom bisher unbekannt. Des Weiteren ist nicht bekannt, wie die verschiedenen Tumor-Subtypen den Phänotyp von TAMs beeinflussen. Die vorliegende Arbeit fokussiert sich deshalb auf die Untersuchung des Einflusses von MEK-Inhibitoren auf das Tumor-Mikromilieu der unterschiedlichen Tumor-Subtypen mit speziellem Fokus auf Makrophagen, sowie auf die Untersuchung der Tumor-Subtyp spezifischen TAM-Heterogenität.

Um die Effekte des MEK-Inhibitors Trametinib auf unterschiedliche Makrophagen-Phänotypen zu untersuchen, wurden pro-inflammatorische M1-ähnliche, anti-inflammatorische M2-ähnliche und unstimulierte M0 Makrophagen aus murinen Vorläuferzellen *in vitro* generiert. *In vitro* Experimente konnten zeigen, dass die MEK-Inhibition nicht zu einer Makrophagende- bzw. -repolarisierung führt. Des Weiteren zeigten anti-inflammatorische M2-ähnliche und unstimulierte M0 Makrophagen eine erhöhte Sensitivität gegenüber MEK-Inhibitor induziertem Zelltod, während pro-inflammatorische M1-ähnliche Makrophagen eine reduzierte Sensitivität aufwiesen. Metabolismus-Analysen zeigten, dass die MEK-Inhibition die oxidative Phosphorylierung von M2-ähnlichen Makrophagen reduzierte, während sie in den anderen Makrophagen-Phänotypen nur geringfügig beeinflusst wurde.

Zur Untersuchung der Tumor-Subtyp spezifischen TAM-Heterogenität und potentiellen Phänotyp spezifischen Effekten der MEK-Inihibition wurden TAMs *in vitro* durch Stimulierung mit Tumor-konditioniertem Medium (TCM) von verschiedenen epithelialen (epiTAMs) und mesenchymalen (mesTAMs) Tumorzell-Linien generiert. Die TAM-Heterogenität wurde anschließend transkriptomisch, metabolisch und immunophänotypisch analysiert. Die TCM-Stimulierung induzierte in epiTAMs und mesTAMs eine metabolische Anpassung mit einer erhöhten oxidativen Phosphorylierung und einer reduzierten Glykolyse. Obwohl epiTAMs und mesTAMs phänotypisch nicht durch klassische M1 und M2 Makrophagen-Markerproteine unterschieden werden konnten, zeigten sie differentielle Genexpression nach TCM-Stimulierung, wobei epiTAMs mit pro-inflammatorischen Gensets, z.B. Interferon-gamma Antwort, assoziiert waren. Im Gegensatz zu epiTAMs waren mesTAMs mit einem Hypoxie-Genset assoziiert und *in vitro* Experimente konnten zeigen, dass epiTAMs und mesTAMs nach TCM-Stimulierung den Hypoxie-induzierbaren Faktor 1A (HIF1A) Signalweg Tumor-Subtyp unabhängig aktivierten. Des Weiteren waren mesTAMs sensitiver gegenüber MEK-Inhibitor induziertem Zelltod im Vergleich zu epiTAMs. *In vivo* Experimente in PDAC-Mäusen, die für 2 Tage oder mehrere Wochen mit einem MEK-Inhibitor behandelt wurden, zeigten Tumore mit reduziertem Makrophagen-Gehalt.

In der vorliegenden Arbeit konnte gezeigt werden, dass TAMs, die mit TCM von verschiedenen Tumor-Subtypen polarisiert wurden, nicht durch klassische M1 und M2 Makrophagen-Markerproteine unterschieden werden konnten. Die Ergebnisse deuteten darauf hin, dass ein kontinuierliches Spektrum an TAM-Phänotypen existierte. Diese TAM-Phänotypen wiesen in Abhängigkeit von den jeweiligen Signalen des Tumor-Mikromilieus eine gleichzeitige Expression von pro- und anti-inflammatorischen Markern auf.

Im Gegensatz zur Markerexpression zeigten TAMs eine Tumor-Subtyp spezifische MAPK-Signalweg Abhängigkeit. Die Trametinib-vermittelte MEK-Inhibition hatte Makrophagen-Phänotyp spezifische Effekte *in vitro* und induzierte den Zelltod von TAMs in einem murinen PDAC Mausmodell, wodurch das immunsuppressive Tumor-Mikromilieu reduziert wurde. Diese Ergebnisse eröffnen die Möglichkeit für die Testung neuer Kombinationstherapien aus MEK-Inhibitoren und Immuntherapie-basierten Ansätzen zur Behandlung dieser verheerenden Tumorentität.

Table of Contents

List of Figures

List of Tables

Abbreviations

°C	degree Celsius
ARG1	Arginase1
BMDM	Bone marrow-derived macrophages
bp	base pairs
BSA	Bovine serum albumin
CD	Cluster of differentiation
cDNA	copy deoxyribonucleic acid
Cish	Cytokine Inducible SH2 Containing Protein
CRE	Causes Recombination
DAPI	Diamidinophenylindole
ddH_2O	double distilled water
DMEM	Dulbecco`s Modified Eagle`s Medium
DMOG	Dimethyloxaloylglycine
DMSO	Dimethylsulfoxid
DNA	Deoxyribonucleic acid
dNTP	deoxyribonucleotide triphosphate
ECAR	Extracellular acidification rate
EDTA	Ethylenediaminetetraacetic acid
Egln3	Hypoxia-Inducible Factor Prolyl Hydroxylase 3
epiMCM	epithelial TCM incubated on macrophages
epiTAMs	epithelial tumor-conditioned medium tumor associated macrophages
EtOH	Ethanol
F4/80	EGF-like module-containing mucin-like hormone receptor-like 1
FACS	Fluorescence activated cell sorting
FBS	Fetal calf serum
FITC	Fluorescein
g	gram
GEMM	Genetically engineered mouse model
GSEA	Gene Set Enrichment Analysis

H	hour(s)
HCl	Hydrochlorid acid
HLA	Human leucocyte antigen
IFNγ	Interferon gamma
Ig	Immunglobulin
IL	Interleukin
IPMN	Intraductal papillary-mucinous neoplasm
IRF4	Interferon regulatory factor 4
Jmjd3	Jumonji Domain Containing 3
KRAS	Kirsten Rat Sarcoma Viral Oncogene Homolog
LPS	Lipopolysaccharide
MCSF	Macrophage colony stimulating factor
MDSCs	Myeloid derived suppressor cells
MEKi	Trametinib
Mgl2	C-Type Lectin Domain Containing 10A
mesMCM	mesenchymal TCM incubated on macrophages
mesTAMs	mesenchymal tumor-conditioned medium tumor associated macrophages
MFI	Mean fluorescence intensity
min	minute(s)
mRNA	messenger RNA
MSR1	Macrophage scavenger receptor 1
NEAA	non-essential amino acids
NOS2	NO synthase 2
o.n.	overnight
OCR	Oxygen consumption rate
PanIN	pancreatic intraepithelial neoplasia
PBS	Phosphate buffered saline
PDAC	Pancreatic ductal adenocarcinoma
PE	Phycoerythrin
PFA	Paraformaldehyde

PI	Propidium Iodide
rev. mesTAMs	mesTAMs incubated for 48h with epithelial TCM
RFU	Relative fluorescence unit
RNA	Ribonucleic acid
rpm	round per minute
RT	room temperature
RPMI	Roswell Park Memorial Institute medium
SD	standard deviation
sec	seconds(s)
Selp	Selectin P
Slc2a1	Glucose Transporter Type 1
TAMs	tumor associated macrophages
TCM	Tumor conditioned medium
TNFα	Tumor necrosis factor alpha
Tris	Tris(hydroxymethyl)aminomethane
VEGFa	Vascular Endothelial Growth Factor
α-	anti-

Introduction

The Pancreas

The pancreas is located in the abdominal cavity adjacent to duodenum and spleen. It functions as an exocrine-endocrine gland and is anatomically divided into a pancreatic head (*Caput pancreatis*), which is connected to the duodenum and the hilum of the spleen, a pancreatic body (*Corpus pancreatis*) and a pancreatic tail (*Cauda pancreatis*). Histologically, the pancreas can be separated into an endocrine and an exocrine compartment. The endocrine islets of Langerhans, which are crucial for nutrient metabolism and blood glucose homeostasis and the exocrine compartment, which is responsible for digestive enzyme production. Islets of Langerhans represent a composition of heterogeneous cell types: glucagon secreting α-cells, insulin secreting β-cells, somatostatin producing δ-cells, grehlin secreting ε-cells and pancreatic polypeptide secreting PP-cells. The exocrine compartment comprises 90% of the pancreas and consists of three different cell types: digestive enzyme producing acinar cells, centro-acinar cells and bicarbonate secreting ductal cells, which neutralize the gastric juice. (Edlund 2002; Pan and Wright 2011).

Pancreas-Associated Diseases and Malignancies

The pancreas is an essential dual-functional organ and diseases affecting its physiological functions and homeostasis can have severe impact on the health status of an individual. Pancreas-associated diseases include of metabolic diseases, e.g. *Diabetes mellitus* type 1 and 2, and inflammatory diseases e.g. acute and chronic pancreatitis. Furthermore, several tumor entities have been described, which differ in their histopathological characteristics. In general, pancreatic endocrine tumors like cystic serous and mucinous neoplasms, squamous cell carcinomas, solid pseudo papillary tumors, pancreatic lymphoma as well as acinar cell carcinoma contribute only to a small amount of pancreatic cancers, while a majority of pancreatic cancer patients (85%) suffers from pancreatic ductal adenocarcinoma (PDAC) (Mulkeen, Yoo, and Cha 2006; Ryan, Hong, and Bardeesy 2014).

Development of Pancreatic Ductal Adenocarcinoma

PDAC can potentially develop from three different non-invasive precursor lesions, although the underlying mechanism of their transition to an invasive carcinoma is still missing. While intraductal papillary mucinous neoplasms (IPMNs) and mucinous cystic neoplasms (MCNs) constitute the minority of pancreatic precursor lesions, pancreatic intraepithelial neoplasms (PanINs) are considered as the most abundant precursor lesion type (Hezel et al. 2006). PanINs are categorized by

a two-tier classification system into low-grade (PanIN1 and PanIN2) and high-grade (PanIN3, *carcinoma in situ*) lesions based on a progressive desmoplastic reaction accompanied by increasing genetic aberrations and epithelial rearrangements (Bardeesy and DePinho 2002).

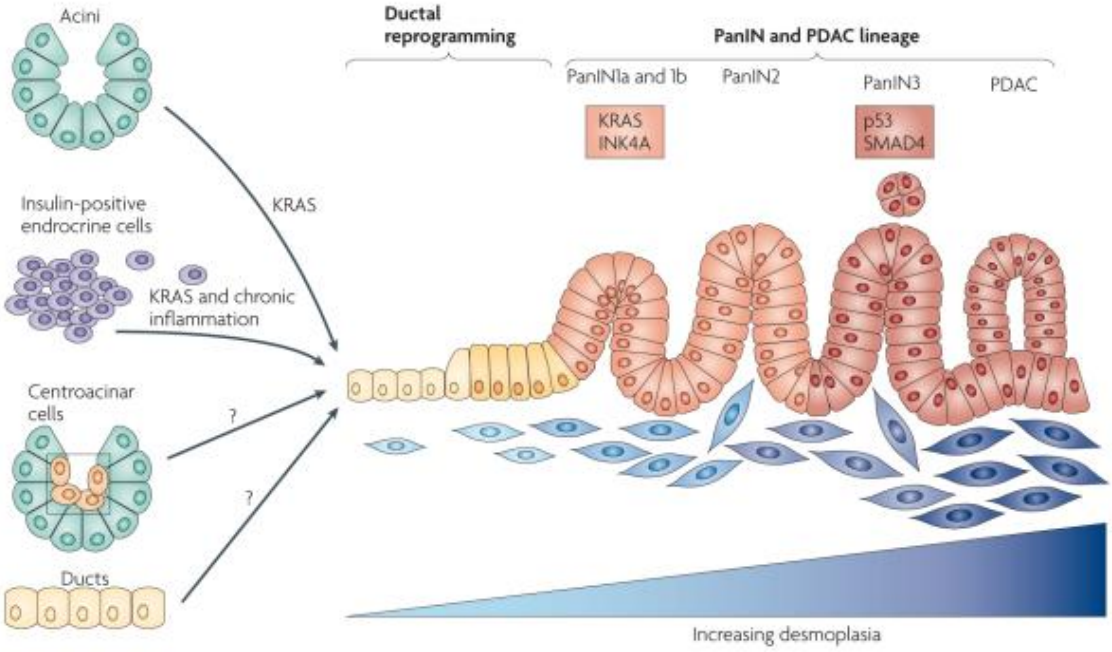

Figure 1.1: Tumor progression model of PDAC. PDAC tumor progression model showing tumor initiation from diverse differentiated exocrine and endocrine pancreatic cell types tier-wise over PanIN precursor lesions to pancreatic ductal adenocarcinoma. An oncogenic *KRAS* mutation is accentuated as a crucial event during PDAC tumor initiation, while PDAC progression is accompanied by an increased infiltration of stromal and immune cells, called desmoplasia. Furthermore, tumor progression is accompanied by additional inactivating mutations in key tumor suppressor genes, e.g. p53 as well as by a loss of the epithelial architecture. The question marks at duct and centroacinar cells indicate that they have not been adressed for their ability to give rise to invasive PDAC through dysregulation of an oncogenic *KRAS* mutation. (Morris, Wang, and Hebrok 2010).

Low-grade lesions frequently occur in the normal adult pancreas, while high-grade lesions are almost exclusively present in patients with PDAC (Sipos et al. 2009).Furthermore, atypical flat lesions (AFL) have been suggested to be another type of precursor lesion, which develops from the centro-acinar compartment via acinar-to-ductal metaplasia (ADM) (Aichler et al. 2012).

Although the cell of origin is controversial, ample evidence shows that ductal cells and acinar cells undergoing ADM are the origin of PDAC (Habbe et al. 2008; Mazur and Siveke 2012; Morris IV et al. 2010; Morris, Wang, and Hebrok 2010).

Pancreatic Ductal Adenocarcinoma

Epidemiology and Treatment Modalities

PDAC is ranked as the 4th leading cause of cancer-related death in the western world and it is predicted to rise to the 2nd most common cause of cancer related death in the United States by 2030 (Jemal et al. 2008; Rahib et al. 2014; Siegel, Miller, and Jemal 2017). The rising incidence is associated with an epidemic in obesity and metabolic syndrome and 5-year survival rates remain constantly below 9%, despite tremendous research efforts in the clinical and preclinical field (McGuigan et al. 2018; Siegel, Miller, and Jemal 2017). High mortality rates are due to the lack of early diagnosis, rapid tumor dissemination as well as ineffective treatment options for advanced tumor stages. Furthermore, the majority of patients (70%) is diagnosed at metastatic stage, which is partly due to a lack of markers for early detection and the long asymptomatic progress of this tumor entity. Surgical resection is the only curative treatment option for PDAC patients in the early stage, while chemotherapy remains the standard-of-care treatment for patients with irresectable or metastatic PDAC. Despite different chemotherapeutic regimens, overall survival of PDAC patients remains poor, reflecting the urgent need for new treatment modalities.

Hallmarks of Pancreatic Ductal Adenocarcinoma

On the molecular level, PDAC is hallmarked by an oncogenic *KRAS* mutation, which is present in over 90% of all tumors (Hezel et al. 2006; Witkiewicz et al. 2015). The dysregulated constitutive activation of *KRAS* is mainly driven by missense mutations, but can also be achieved by gene amplification. In human PDAC, G12D and G12V mutations are the most common *KRAS*-activating mutations. Besides mutations in codon G12, mutations in codon G13 and Q61 have been described and current data indicate that these allele mutations are disparate to the G12 mutations, e.g. in terms of MAP kinase activity (Prior, Lewis, and Mattos 2012). The high frequency of oncogenic *KRAS* mutations in PDAC patient led to investigations for small molecule inhibitors, which target the MAPK pathway downstream of *KRAS*, since *KRAS* seems to be undruggable until today. A body of studies investigated the efficacy of mitogen-activated protein kinase kinase 1/2 (MEK1/2) inhibitors (MEKi) in different *KRAS*-driven tumor entities, showing that subgroups of patients benefited from the inhibitor treatment in some of the investigated entities (Corcoran et al. 2015). A phase I/II study investigated the efficacy of the MEKi refametinib in combination with chemotherapy in advanced pancreatic cancer with an objective response rate of 23% (Van Laethem et al. 2017). However, MEKi monotherapy (trametinib) failed to improve clinical parameters in clinical trials. A randomized, double-blind, placebo-controlled trial investigated the potential effect of trametinib in combination with standard-of-care chemotherapy gemcitabine in patients with untreated metastatic pancreatic

adenocarcinoma. This study showed no significant difference in overall and progression-free survival and in overall response rate in patients who received gemcitabine in combination with trametinib in comparison to gemcitabine and placebo-based combinatorial treatment (Infante et al. 2014). Recent research focused on application of MEKi in combination with immunotherapeutic approaches, since pharmacological MEK inhibition was shown to potentiate anti-tumor T cells by impairing T cell receptor-driven apoptosis (Ebert et al. 2016) . Importantly, combination of MEKi and antibody-mediated blockade of PD-L1 resulted in durable anti-tumor immune response in comparison to monotherapeutic treatments in mice with subcutaneously injected colon cancer cells, justifying the rationale to investigate this type of combinatorial therapy approach to other tumor entities.

In addition to *KRAS* mutations, PDAC also frequently harbor inactivating mutations in tumor suppressor genes, e.g. *TP53* (72%), *CDKN2A* (30%) and *SMAD4* (32%) during tumor progression (Raphael et al. 2017). The prevalence of other mutations in PDAC remains below 10%, which reflects the high degree of genetic heterogeneity in this disease.

Another important hallmark of PDAC is a prominent desmoplastic reaction, which dramatically increases during tumor progression from preneoplastic lesions to an invasive carcinoma (Bardeesy and DePinho 2002). The desmoplastic reaction is characterized by a tremendous infiltration of stromal and immune cells as well as an excessive production of extracellular matrix components, which results in the establishment of a multifaceted tumor microenvironment. Pancreatic stellate cells and cancer-associated fibroblasts (CAFs) contribute to one part of the diverse tumor microenvironment by producing extracellular matrix proteins, e.g. collagen, whereas endothelial vascular cells are associated with intratumoral vessel formation (Apte et al. 2004; Hidalgo 2010). Furthermore, the major compartment of tumor-infiltrating cells is contributed by immune cells from both the innate and adaptive lineage of the immune system. In PDAC, the number of tumor-infiltrating non-tumor cells surpasses the number of malignant tumor cells inside the tumor bulk (Chu et al. 2007).

Subtypes in Pancreatic Ductal Adenocarcinoma

Investigations of the cancer transcriptomes revealed the existence of different PDAC subtypes, which were associated with distinct clinical outcomes and therapeutic responses. While Collisson et al. showed the existence of three different tumor subtypes (classical, quasimesenchymal, exocrine-like) using microarray analysis, Moffitt and co-workers defined two tumor subtypes (classical and basal-like) and additionally described two stromal subtypes (normal and activated) by using microarray analysis of microdissected tumor samples with virtual separation of tumor, stroma and normal tissue

by gene deconvolution (Collisson et al. 2011; Moffitt et al. 2015). The investigations from Collisson et al. revealed that patients with a quasimesenchymal tumor had worse overall survival in comparison to exocrine-like and classical PDAC. Furthermore, Moffitt et al. showed a reduced survival for patients with basal-like tumors. In addition to Collisson and Moffitt, Bailey et al. showed the existence of four tumor subtypes (squamous, pancreatic progenitor, immunogenic, aberrantly differentiated endocrine exocrine (ADEX)) by integrative genomic analysis using RNA sequencing (Bailey et al. 2016). In Baileys‘ dataset, the squamous subtype was associated with poor overall survival in comparison to the other subtypes. In addition, Puleo et al. further stratified PDAC based on gene expression of both tumor cells and the microenvironment and revealed five subtypes (pure basal-like, stroma activated, desmoplastic, pure classical, immune classical) (Puleo et al. 2018). The pure basal-like subtype showed worst survival, followed by the stroma activated and desmoplastic subtype, while immune classical and pure classical were associated with better prognosis. More recently, Maurer et al. attempted to harmonize the results obtained from the different studies regarding the number of subtypes by performing RNA sequencing of laser capture microdissected samples from PDAC tissue and adjacent stroma (Maurer et al. 2019) . Maurer et al. revealed the existence of 2 PDAC subtypes (classical and basal-like) and identified additionally 2 stromal subtypes (immune-rich and ECM-rich). These stromal subtypes partly aligned with epithelial subtypes with classical tumors being associated with an immune-rich stromal subtype and a better overall survival, while basal-like tumors were associated with an ECM-rich stroma und worse survival. Noteworthy, the immune-related subtypes of different studies indicates divergent immune cell composition. While Baileys‘ immunogenic subtype contains high amounts of tumor-promoting macrophages, Puleos‘ classical immune subtype is highly infiltrated by natural killer, T and B cells, implying a more cytotoxic environment (Bailey et al. 2016; Puleo et al. 2018).

Importantly, the tumor stroma plays a pivotal role in separating between different tumor subtypes, highlighting the relevance of stromal content, e.g. fibroblasts and immune cells, with regards to clinical outcomes.

Tumor-Infiltrating Leukocytes

In PDAC tumor tissue, roughly 50% of tumor bulk cells express the leukocyte common antigen CD45 (Clark et al. 2007). Analysis of spontaneous and genetically engineered mouse models of PDAC show that immune cells are present since early stage of tumor development. They are found in preneoplastic lesions and the quantity of immune cell infiltrate increases during tumor progression to invasive carcinoma (Cheung et al. 2018; Clark et al. 2007). In pancreatic cancer, infiltrating immune cells have been shown to act mainly in an immunosuppressive and tumor-promoting

manner, which underlines the relevance of current research efforts to delineate and understand the cross-talk between infiltrating immune and tumor cells.

Tumor-Associated Myeloid Cells

Hematopoiesis is a continuous differentiation process in which multipotent hematopoietic stem cells (HSCs) differentiate into diverse blood cell types (Zhang et al. 2018). During this differentiation process, common myeloid progenitor cells (CMPs) can differentiate into cells from the myeloid lineage. This myeloid lineage cells can either stay in an immature state, e.g. as monocytes and myeloid-derived suppressor cells (MDSCs) or they develop into terminally differentiated mature macrophages, granulocytes and dendritic cells (DCs) (Gabrilovich, Ostrand-Rosenberg, and Bronte 2012). Myeloid cells, except for some DC subsets, are characterized by their expression of integrin α-M (CD11b). The subsequent chapter will particularly focus on MDSCs and macrophages, since they have been shown to play a major role in modulating anti-tumor immune response in PDAC.

Myeloid-Derived Suppressor Cells (MDSCs)

The term „myeloid-derived suppressor cells“ was established approximately 10 years ago in the scientific community and described a poorly defined population of myeloid cells with immunosuppressive potential (Gabrilovich et al. 2007). To date, two different groups of MDSCs have been described, which can be separated by phenotypical, morphological and biochemical properties: monocytic MDSCs (M-MDSCs) and granulocytic or polymorphonuclear MDSCs (PMN-MDSCs). Morphologically, MDSCs show high accordance to monocytes and granulocytic neutrophils, with M-MDSCs being morphologically similar to monocytes, while PMN-MDSCs showing similarity to neutrophils (Gabrilovich, Ostrand-Rosenberg, and Bronte 2012). During chronic infection and permanent inflammation, e.g. in cancer, myeloid cells get exposed to relatively weak and long-lasting stimulation of inflammatory cytokines and growth factors, resulting in the development of myeloid cells with an immature morphology and phenotype. These immature myeloid cells are characterized by a weak phagocytic activity, high expression of prostaglandin E2 (PGE2) and arginase, high levels of nitric oxide (NO) and reactive oxygen species (ROS) as well as by the expression of anti-inflammatory cytokines (Umansky et al. 2016; Youn et al. 2012). This pathological activation status obtains high immunosuppressive potential and can support tumor progression by inhibiting an effective adaptive anti-tumor immune response. M-MDSCs can be separated from tumor associated macrophages (TAMs) by lacking expression of macrophage marker protein F4/80 (Gabrilovich and Nagaraj 2009). In humans, MDSCs can be distinguished from neutrophils and monocytes based on phenotypic markers.

PMN-MDSCs can be separated from neutrophils by expression of LDL receptor 1 (LOX-1) (Condamine et al. 2016). Additionally, M-MDSCs and monocytes can be separated by the expression level of MHC class II molecules, which are highly expressed in monocytes, but poorly expressed on M-MDSCs. In the tumor microenvironment, MDSCs can downregulate STAT3 activity via activation of CD45 phosphatase, which supports differentiation of M-MDSCs into tumor-associated macrophages (Kumar et al. 2016). Furthermore, M-MDSCs not only quickly differentiate into immunosuppressive tumor-associated macrophages, but also into inflammatory dendritic cells, which have been shown to possess tumor-promoting as well as tumor-suppressive properties (Ma et al. 2013; Marigo et al. 2016; Ribechini et al. 2017).

Both, PMN-MDSCs and M-MDSCs, possess high immunosuppressive capacities, which distinguishes them from monocytes and neutrophils. Numerous studies revealed a positive correlation of peripheral blood MDSCs with tumor stage in multiple cancer types (Angell et al. 2016; Arihara et al. 2013; Sun et al. 2012). Additionally, high numbers of PMN-MDSCs and M-MDSCs have been shown to be negatively correlated to chemo- and radiotherapy in a variety of solid tumors (Diaz-Montero et al. 2009; Tada et al. 2016; Wang and Yang 2016). However, most studies particularly focused on peripheral blood circulating MDSCs. Future studies should additionally address tumor-infiltrating MDSCs to obtain a more comprehensive insight into the roles of MDSCs in cancer.

Macrophages

Ontogeny and Development

The existence of tissue resident macrophage populations in adults, which were not derived from the monocytic lineage implicates ontogenic heterogeneity of these cells. Recent studies have shown that adult tissue resident macrophages derive from embryonic progenitor cells, which seed into different tissues before birth. This prenatally seeded macrophages persist over time, maintain its pool into adulthood by self-renewal and have been shown to be distinct from HSC-derived macrophages in terms of transcription factor dependency and patterns of differentiation (Ginhoux et al. 2010; McGrath et al. 2003; Takahashi, Yamamura, and Naito 1989). It is important to note that this embryonic progenitor-derived macrophages differ from adult HSC-derived monocytes since they do not require CSF1R for their generation (Ginhoux et al. 2010; Hoeffel et al. 2012). Recent studies revealed that this ontogenic heterogeneity of macrophages within adult tissues can vary in the steady state with some tissues being permanently replaced by bone marrow-derived monocytes, e.g. alveolar macrophages in the lung and Langerhans cells in the dermis, whereas other tissues, e.g. microglia in the brain, remain largely of embryonic origin (Guilliams et al. 2013; Hoeffel et al. 2012).

Physiological Roles of Macrophages

Macrophages represent a heterogeneous population of cells, which are characterized by their tremendous functional and phenotypical plasticity. During development, macrophages and their precursor cells seed into various tissues. Once migrated into these tissues, macrophages receive tissue-specific environmental cues, resulting in tissue-specific activation of gene expression, thereby contributing to functional heterogeneity of different macrophage pools throughout the body. This functional heterogeneity is an important feature of macrophages to meet the diverse demands of the different niches they are occupying.

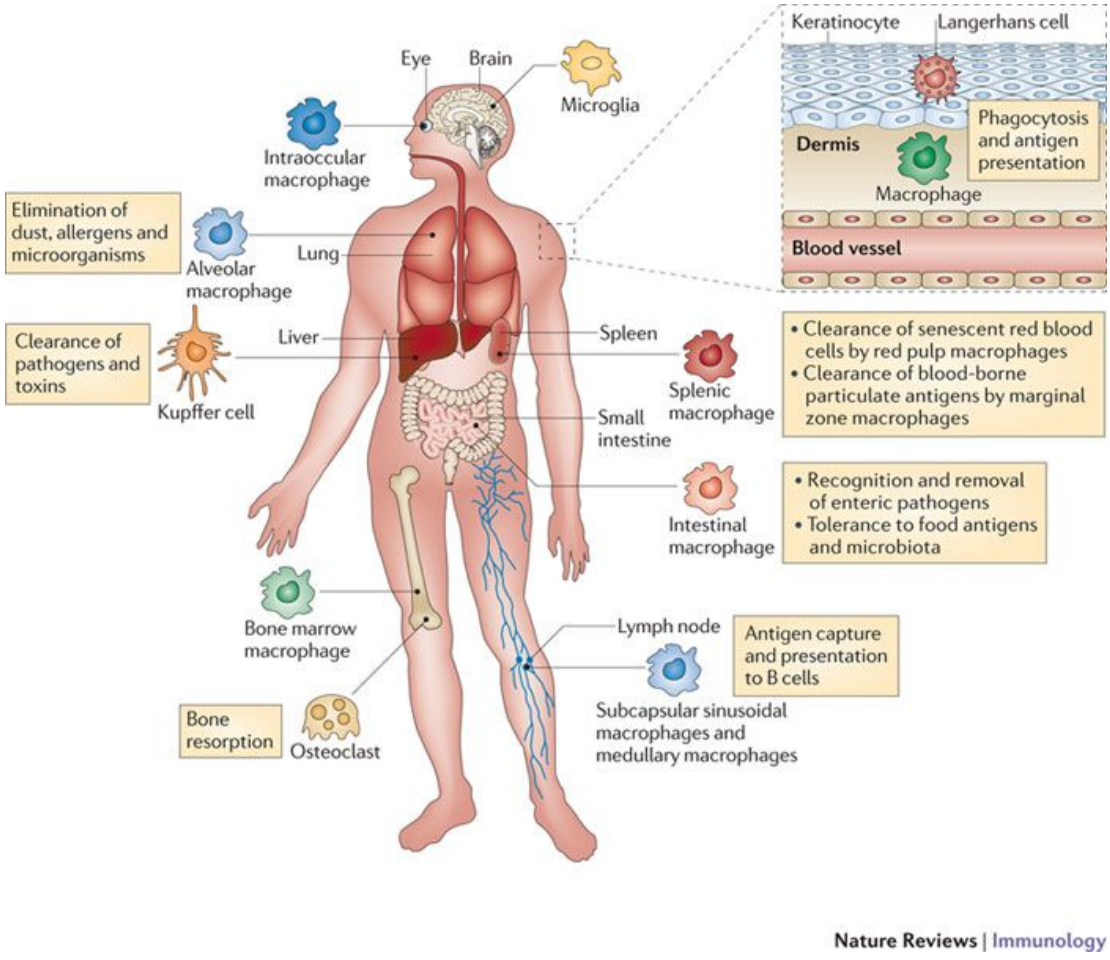

Figure 1.2: Tissue-specific macrophage heterogeneity. Hematopoietic stem cells (HSCs) generate HSC-derived monocytes, which migrate via the circulatory system to almost all tissues within the human body. Migrated monocytes obtain tissue-specific environmental cues after extravasation and differentiate into macrophages, which perform tissue-specific as well as immune surveillance activities Figure from: (Murray and Wynn 2011).

In general, macrophages are divided into subpopulations based on anatomical localization and functional phenotype (Gordon and Taylor 2005). These macrophage populations are specialized to their specific microenvironments and conduct tissue-specific functions. Alveolar macrophages reside in the lung and eliminate allergens, microorganisms and dust, whereas Kupffer cells in the liver efficiently eliminate toxins and pathogens from the portal and arterial circulation (Allard, Panariti, and Martin 2018; Dixon et al. 2013). Bone-resident osteoclasts play pivotal role in bone resorption

and remodeling, while macrophages residing sinusoidal or medullary in lymph nodes capture antigens and present them to B cells, T cells and dendritic cells (Gray and Cyster 2012; Xu and Teitelbaum 2013). Furthermore, intestinal macrophages recognise and remove enteric pathogens, while regulating homeostasis and tolerance for microbiota and food antigens (Bain and Schridde 2018). Splenic macrophages are further subdivided based on their intrasplenic localization into red pulp macrophages, which eliminate senescent red blood cells and marginal zone macrophages, which internalize blood-borne pathogens (Borges Da Silva et al. 2015). In the brain, microglia have been shown to be involved in synapse maturation and remodeling, while Langerhans cells and dermis-resident macrophages patrol the skin to present antigens and, if necessary, activate cells of the adaptive immune system (Clayton et al. 2017; Paolicelli et al. 2011; Schafer et al. 2012).

Besides tissue-specific functions, macrophages possess the ability to phagocytose apoptotic cells, debris, pathogens and tumor cells and are the first line of defense of innate immunity. To recognize foreign particles and apoptotic cells, macrophages contain a repertoire of pattern recognition receptors (PRRs) e.g. Toll-like receptors (TLRs), C-type lectin receptors (CLRs), scavenger receptors, retinoic acid-inducible gene 1 (RIG1) -like helicase receptors (RLRs) and NOD-like receptors (NLRs) to monitor their surroundings. Additionally, they can express multiple secreted molecules e.g. complement and Fc receptors, which bind opsonin molecules to activate a complement cascade or support phagocytosis of tagged pathogen surfaces (Gordon and Taylor 2005). Furthermore, they are considered as antigen-presenting cells (APCs) that act at the crosslink between innate and adaptive immunity by presenting ingested antigens via major histocompatibility complexes (MHCs) to T cells. Macrophages can not only initiate $CD8^+$ T cell mediated immunity by antigen presentation, but they can also have immunosuppressive capacities by inhibiting $CD8^+$ T cell activation through expression of immune checkpoint molecules or by secretion of immunosuppressive cytokines (Olazabal et al. 2008; Su et al. 2018). In general, macrophage activation is a tightly regulated process, which is influenced by the predominant signals of the respective microenvironment.

Heterogeneous Macrophage Phenotypes

Macrophages can be activated by a plethora of well-known stimuli derived from their microenvironment. In the past, macrophage activation was considered to be a dichotomy with pro-inflammatory (classically activated) M1 macrophages being polarized by interferonγ (IFNγ) and/or lipopolysaccharide (LPS) on one side and anti-inflammatory (alternatively activated) M2 macrophages polarized by interleukin-4 (IL4) and interleukin-13 (IL13) on the other (Nathan et al. 1983; Stein et al. 1992). In this context, M1 macrophages enhanced T_H1 type immune responses by production of pro-inflammatory mediators, e.g. IL1β, IL6, IL12 TNFα and iNOS, whereas M2

macrophages supported a T_H2 type immune responses by production of Arg1, Arg2, mannose receptor 1 (CD206), Fizz1, IL10, Mgl1, polyamines as well as different scavenger receptors. Furthermore, alternatively activated M2 macrophages show a downregulation of IL12 and other pro-inflammatory cytokines (Gordon 2003; Mosser and Edwards 2008; Sica et al. 2006). In addition of being activated by soluble factors binding to its respective receptors, macrophages can be activated by receptor binding to foreign structures or antibodies as well. Upon binding, receptors become phosphorylated to activate intracellular downstream signaling, leading to activation of transcription factors. In turn, transcription factors activate specific gene expression programs, resulting in generation of a functional macrophage phenotype. During macrophage activation, there are several transcription factors playing pivotal role in determining functional phenotype development by supporting either pro- or anti-inflammatory macrophage signaling. Transcription factors of the signal transducers and activators of transcription (STAT) family have been shown to be involved in both, pro- and anti-inflammatory phenotype induction. While STAT1 is induced by IFNγ and promotes an M1 phenotype by iNOS and IL12 transcription, STAT6 is known to be induced by IL4 and IL13 and support an M2 phenotype by supporting expression of other M2-associated transcription factors e.g. KLF4 (Darnell, Kerr, and Stark 1994; Lawrence and Natoli 2011). Under inflammatory stress, nuclear factor κB (NFκB) and activator protein1 (AP1) are activated to promote M1 polarization, while expression of peroxisome proliferator-activated receptors (PPARs) in general represses the transcrptional activity of STATs, NFκB and AP1, thereby impairing M1 polarization (Fujioka et al. 2004; Ricote et al. 1998). Furthermore, several interferon-recognition factors (IRFs) e.g. IRF3, IRF5 and IRF9 have been shown to promote M1 polarization, whereas IRF4 is activated by parasitic or fungal infections, resulting in promotion of M2 polarization (Satoh et al. 2010; Schindler and Darnell 1995; Takaoka et al. 2005; Toshchakov et al. 2002). Hypoxia-inducible factors (HIFs) also show ambivalent role in macrophage activation with HIF1α being induced by NFκB and promoting M1 polarization via iNOS transcription, whereas HIF2α is induced in M2 polarized macrophages limiting nitric oxide (NO) synthesis (El Chartouni, Schwarzfischer, and Rehli 2010). Besides distinct cytokine and transcription factor profiles, macrophages have been characterized based on their metabolism. It was shown that anti-inflammatory M2 macrophages possess high mitochondrial oxidative phosphorylation with reduced glycolysis, while pro-inflammatory M1 macrophages showed an increased glycolytic metabolism with concomitant reduction in mitochondrial activity (Van den Bossche, Baardman, and de Winther 2015). In general, macrophage metabolism is tightly associated with the functional activation state in order to meet the energetic demands required to respond to their environmental cues. While high glycolysis rates have been associated to phagocytosis, secretion of pro-inflammatory cytokines, anabolic pentose phosphate pathway and production of ROS, increased OXPHOS rates have been linked to anti-inflammatory cytokine production, fatty-acid

oxidation and promotion of arginase activity, thereby supporting anti-inflammatory functions of these cells (Freemerman et al. 2014; Ip et al. 2017; Pavlou et al. 2017; Vats et al. 2006).

However, increasing evidence has shown that macrophage activation is far more complex, with macrophages showing evidence of both pro- and anti-inflammatory genes being expressed simultaneously, but hitherto, little is known about how different signals are concomitantly integrated to achieve a functional phenotype of these cells (Bardi, Smith, and Hood 2018; Martinez and Gordon 2014). In general, it is assumed that macrophages form a continuum of partly reversible activation states rather than two different extreme phenotypes. This fact is specifically relevant for the *in vivo* situation, where these cells are simultaneously exposed to a plethora of different stimulatory and inhibitory signals, which are derived from diverse cell types in varying concentrations. To closely mimic the *in vivo* situation *in vitro*, a body of studies are recently using cell conditioned medium, e.g. from tumor cells, to mimic the diversity of signals influencing macrophage activation state.

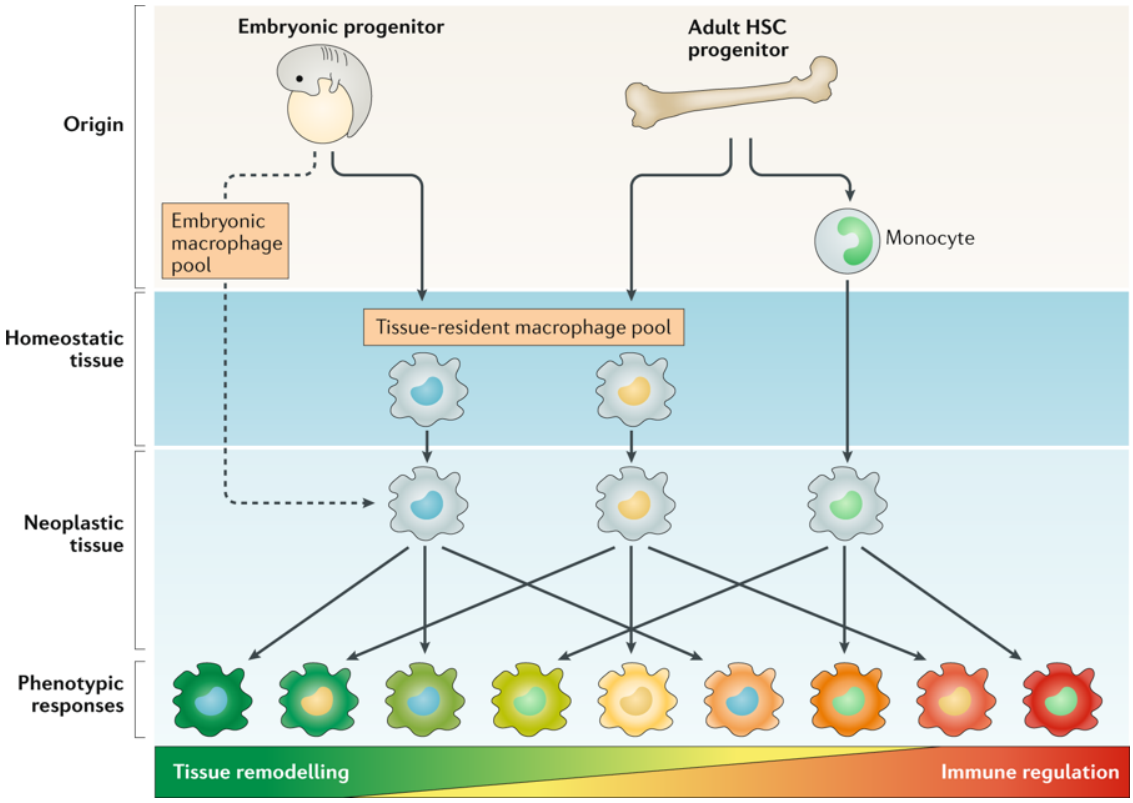

Figure 1.3: Heterogeneity of macrophage phenotypes. Tissue macrophages derive from embryonic progenitor cells as well as from adult HSCs with both contributing to the tissue-resident macrophage pool to different extents depending on the respective tissue. Once migrated into the tissue, macrophages are exposed to a plethora of different stimuli derived from different cell types e.g. in tumor tissue. The developmental origin as well as their tissue of residence fine-tunes macrophage response to polarization cues, indicated by the different colours of macrophage phenotypes. Figure from: (DeNardo and Ruffell 2019).

Pathophysiological Roles of Macrophages

Macrophage activation is a tightly regulated process, which, when dysregulated, can cause severe damage and dysregulated macrophage activation is associated with different pathophysiological conditions. During obesity progression in the adipose tissue, macrophages switch from an anti-inflammatory M2 to a M1 phenotype with strong pro-inflammatory activity (Odegaard and Chawla 2011). Anti-inflammatory macrophages were shown to play important role in allergic responses and asthma, even though their function remains controversial with some studies showing a inflammation-supportive function, while others describe a suppressive capacity of these cells (Bhatia et al. 2011; Stolarski et al. 2010). In addition, macrophages are associated with autoimmune and chronic inflammatory diseases e.g. rheumatoid arthritis, Crohn's disease and multiple sclerosis and with atherosclerosis fibrotic diseases (Kawane et al. 2006; Murphy et al. 2003; Smith et al. 2009; Woollard and Geissmann 2010; Wynn and Barron 2010). Furthermore, numerous studies revealed the supporting role of macrophages in promoting tumor growth, therapy resistance and metastatic spreading by multiple mechanisms.

Tumor-Associated Macrophages (TAMs)

Solid tumors are frequently infiltrated by immune cells with macrophages being one of the most abundant infiltrating cell types. In general, macrophage infiltration is associated with poor prognosis in most tumor entities, which is, in part, due to their ability to suppress responses to standard therapies, e.g. radiotherapy, chemotherapy or anti-angiogenic inhibitors (Engblom, Pfirschke, and Pittet 2016; Noy and Pollard 2014; Ruffell and Coussens 2015). Macrophages have been shown to regulate tumor cell death and survival directly, but there are also indirect ways in which they can promote tumor progression by T cell suppression (Olson et al. 2017; Pyonteck et al. 2013). L-arginine is pivotal for anti-tumor T cell activity and fitness and murine macrophages have been shown to metabolize L-arginine through expression of ARG1, leading to L-arginine depletion (Geiger et al. 2016; Kusmartsev and Gabrilovich 2005). However, ARG1 is not expressed in human macrophages, but in granulocytes, challenging the relevance of a macrophage-driven L-arginine metabolism for T cell regulation in human (Munder et al. 2005; Zea et al. 2005). Furthermore, macrophages can influence T cell responses by expression of iNOS with some studies showing an immunosuppressive role of iNOS, whereas others report a T cell promoting role, highlighting the context-dependency under different conditions (Klug et al. 2013; Marigo et al. 2016; Movahedi et al. 2010). Another way of direct T cell suppression is mediated by expression of immune checkpoint ligands. Programmed cell death 1 ligand 1 (PDL1) is expressed on macrophages in different tumor entities and has been shown to suppress tumor-specific T cell activation *in vitro* and *in vivo* (Kuang et al. 2009; Lin et al.

2018). Additionally, macrophages have been shown to express B7-H4, which promotes macrophage immunosuppressive capacity *in vitro* (Kryczek et al. 2006; Li et al. 2018). In addition to expression of immune checkpoint ligands, macrophages can influence tumor-infiltrating T cells by secretion of immunosuppressive cytokines e.g. TAMs are known to be important for IL-10 production, resulting in suppression of T cell stimulation (Ruffell et al. 2014; Smith et al. 2018).

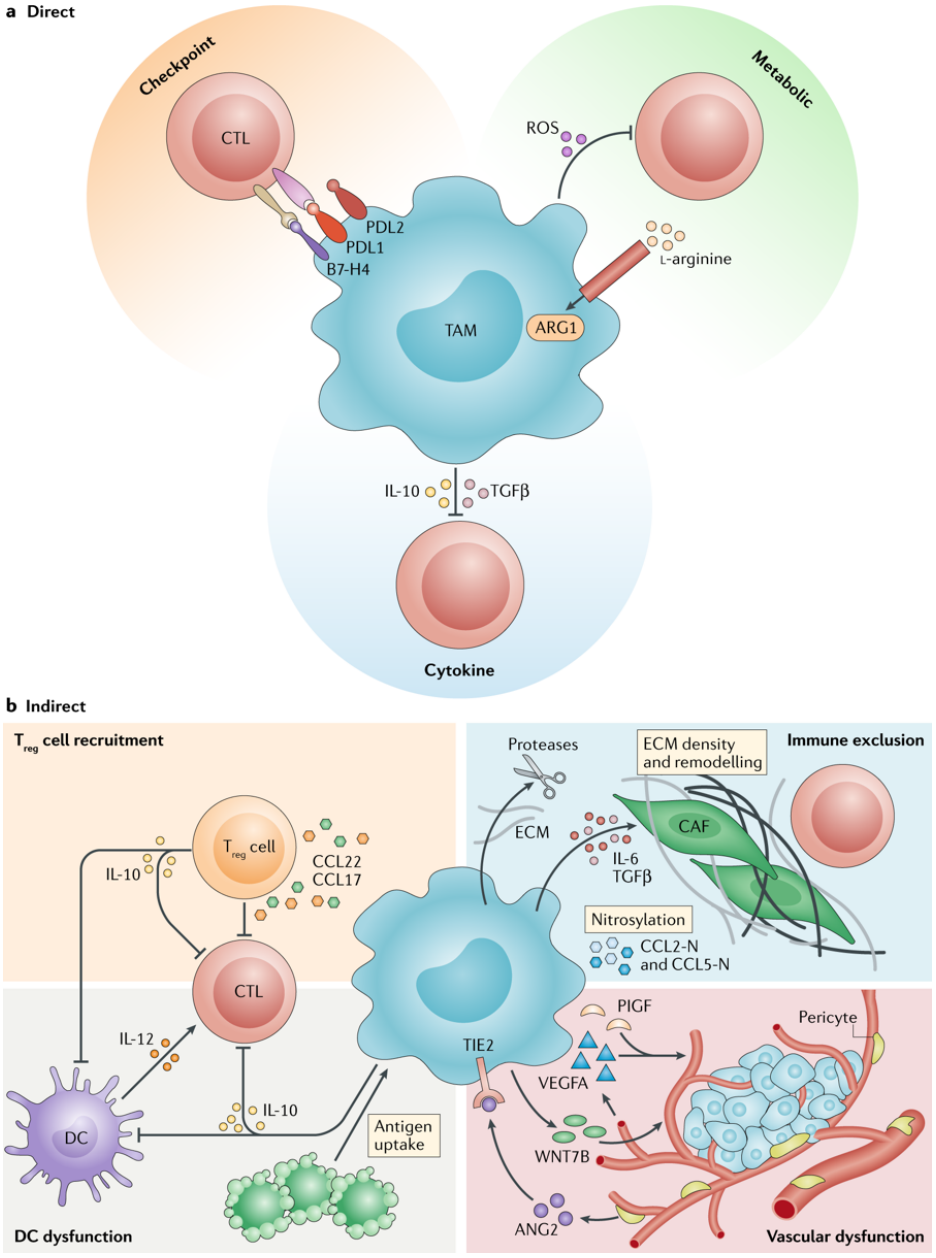

Figure 1.4: Direct and indirect mechanisms of tumor-associated macrophage (TAM)-mediated T cell regulation. A: TAMs directly interact with cytotoxic T cells (CTLs) to regulate their function. TAMs express immune checkpoint ligands, e.g. PDL1, which inhibit T cells. Furthermore, macrophages secrete immunosuppressive cytokines e.g. IL-10 to influence T cell activation. Metabolically, macrophages deplete metabolites by metabolizing L-arginine via ARG1 and production of reactive oxygen species (ROS). B: TAMs indirectly impair T cell function by influencing the tumor microenvironment. TAMs recruit regulatory T cells and promote dendritic cell dysfunction by production of IL-10. TAMs remodel the extracellular matrix (ECM) by metalloproteases or by secretion of TGFβ influencing cancer-associated fibroblasts (CAFs), resulting in exclusion of intratumoral T cells. Additionally, TAMs regulate vascular structure by expression of e.g. VEGFA. ANG2, angiopoietin 2; CCL, CC-chemokine ligand; VEGFA, vascular endothelial growth factor A; WNT7B, Wnt family member 7B (Figure from: (DeNardo and Ruffell 2019).

Besides affecting tumor-infiltrating T cells directly, macrophages can influence T cell-mediated adaptive anti-tumor immune response by indirect mechanisms. Several studies have shown that macrophages regulate T cell recruitment with inhibition of macrophage recruitment via CSF1R or CCR2 inhibition resulting in enhanced recruitment of T cells, although the underlying molecular mechanisms are currently unknown (Mitchem et al. 2013; Shiao et al. 2015). Macrophages are not only important for T cell recruitment, but also for intra-tumoral T cell localization. In pancreatic cancer, macrophages have been shown to prevent T cell infiltration by increasing fibrosis through promoting recruitment of myofibroblasts (Nielsen et al. 2016). Additionally, it is conceivable that macrophages regulate desmoplasia through activation of TGFβ and expression of different matrix metalloproteases (Kessenbrock, Plaks, and Werb 2010). T cell regulation can also be achieved by macrophage-mediated regulation of other cell types. It was shown that macrophages secrete CCL22 to enhance regulatory T cell (Treg) recruitment to the tumor site, which subsequently suppressed cytotoxic T cells. Furthermore, macrophages produce IL-10, which suppresses IL-12 expression by inta-tumoral dendritic cells, dampening anti-tumor T cell response (Curiel et al. 2004; Ruffell et al. 2014).

In pancreatic cancer, tumor-associated macrophages play a pivotal role in supporting the tumor. Macrophage-targeted therapy by CSF1 receptor (CSF1R) blockade reprogrammed tumor-infiltrating macrophages by increasing antigen presentation in a PDAC mouse model, resulting in productive antitumor T cell response (Zhu et al. 2014). Importantly, macrophage-directed CSF1R therapy increased immune checkpoint molecule expression on T cells and combination therapy of CSF1R and PD1 or CTLA-4 blockade resulted in potent murine PDAC tumor regression. Another preclinical study demonstrated that macrophages contributed functionally to the aggressive squamous tumor subtype and that macrophage CSF1R inhibition resulted in tumor shrinkage through decreased tumor cell proliferation and increased T cell-mediated cell death induction (Candido et al. 2018). Inhibition of tumor-infiltrating myeloid cells by a small-molecule CD11b agonist reduced tumoral myeloid cell recruitment and changed their phenotypes, leading to increased response to radiation and chemotherapy and sensitizing murine tumors to checkpoint blockade (Panni et al. 2019). In addition to preclinical studies, clinical trials assessed the safety and effectiveness of tumor-associated macrophage targeted therapies in pancreatic cancer patients. A phase Ib non-randomized trial in patients with locally advanced pancreatic cancer revealed that a combination therapy of the CCR2 small molecule inhibitor PF-04136309 and FOLFIRINOX chemotherapy was tolerated and that 16 out of 33 patients had an objective treatment response, while 32 achieved local tumor control (Nywening et al. 2016). Another clinical trial investigated the maximum-tolerated dose, safety and anti-tumor activity of a combinatorial treatment approach utilizing the agonist CD40 antibody CP-870,893 in combination with gemcitabine chemotherapy in patients with advanced pancreatic ductal

adenocarcinoma. The trial revealed that the combination therapy was well-tolerated and was associated with an anti-tumor activity in PDAC patients (Beatty et al. 2013).

To summarise, tumor-associated macrophages act as one of the key immunosuppressive cell populations within the PDAC microenvironment that can affect tumor immune escape by a multitude of mechanisms, making them a promising target anti-cancer therapies.

Aim of Study

Pancreatic ductal adenocarcinoma (PDAC) is a highly aggressive tumor entity, which is characterized by a high therapy resistance, reflecting the urgent need for identification of new treatment targets. In the past, clinical trials started to investigate MEK inhibitors (MEKi), since the vast majority of PDAC patients harbor an oncogenic *KRAS* mutation. Besides affecting tumor cells, MEKi has been described to induce profound changes within the tumor microenvironment (TME). PDAC is hallmarked by a dense immune cell-rich fibrotic stroma with tumor-associated macrophages (TAMs) being the predominant immune cell infiltrate. Importantly, TAMs are involved in a multitude of pro-tumorigenic and immunosuppressive mechanisms, making them a promising target for anti-cancer therapy. However, despite recent advances in our understanding of the effects of MEKi on the TME, little is known about the influence of MEKi on TAMs in PDAC.

Furthermore, PDAC tumors were transcriptomically stratified into two different tumor subtypes, epithelial and mesenchymal, with the latter being more aggressive and demonstrating worse prognosis and survival. In addition to tumor cells, TAMs also display high heterogeneity and plasticity in terms of pro- and anti-inflammatory phenotypes upon various stimuli in the TME. It was shown that different PDAC tumor subtypes are, at least in part, associated with distinct stromal subtypes, although the influence of different PDAC tumor subtypes on the phenotype of TAMs is unknown.

This work aimed at investigating the effects of MEKi on macrophages in the PDAC microenvironment and further examined how different tumor subtypes influence the phenotype and MEKi sensitivity of TAMs in PDAC.

Materials & Methods

Materials

Equipment and machines

4200 TapeStation	Agilent
Aspiration pipets	NeoLab
Autostainer XL	Leica Camera AG
AxioScan.Z1 Slide Scanner	Carl Zeiss AG
C1000 Touch™ Thermal Cycler	Bio-Rad GmbH
Cell culture bench SAFE 2020	Thermo Fisher Scientific
Cell culture microplate	Agilent
Cell scraper S	TPP AG
Cell Sorter S3e™	Bio-Rad GmbH
Cellstar® reaction tubes 15 ml	Greiner BIO-ONE
Cellstar® reaction tubes 50 ml	Greiner BIO-ONE
ChemiDoc™ MP Imaging System	Bio-Rad GmbH
Counting Slides	Bio-Rad GmbH
Decloaking chamber	Biocare Medical
Discardit™ II 10 ml	BD Bioscience
Eclipse™ Needle 25G	BD Bioscience
Electrophoresis chamber	PEQLAB Biotechnologie GmbH
Electrophoresis power supply EV265	Consort GmbH
Extracellular Flux Analyzer XF^e96	Agilent
FACSCelesta flow cytometer	BD Bioscience
Feeding Needle 22 G	Fine Science Tools
Ficoll Paque Plus	GE Healthcare
Freezer ES Series (-20° C)	Thermo Fisher Scientific
Fridge ES Series (4 °C)	Thermo Fisher Scientific
Gel Doc System XR+	Bio-Rad GmbH
Heating bath	Lab ARMOR™
Heating magnetic stirrer AREC.T	VELP Scientifica

Heraeus FRESCO17 centrifuge	Thermo Fisher Scientifc
Heraeus Megafuge 8R centrifuge	Thermo Fisher Scientific
Heraeus Megafuge 16R centrifuge	Thermo Fisher Scientifc
Hot Bead Sterilizer FST 250	Fine Science Tools
Ice bath containers	Biocision
Incubator HERAcell 240i	Thermo Fisher Scientific
LightCycler® 480	Roche GmbH
LightCycler® 480 Multiwell Plate 96	Roche Diagnostics GmbH
LightCycler® 480 Sealing Foil	Roche Diagnostics GmbH
MACS Multistand	Miltenyi Biotech
Multichannel pipet 50 µl – 300 µl	Gilson
LS Column	Miltenyi Biotech
Maxwell RSC	Promega
Microwave NM-E201WM	Panasonic
Mini PROTEAN® Tetra System	Bio-Rad GmbH
Multidrop combi	Thermo Fisher Scientfic
Multipipete® E3	Eppendorf GmbH
myTEMP™ Mini Digital Incubator	Benchmark
Nanodrop 2000c Spectrophotometer	Thermo Fisher Scientifc
Neubauer counting chamber	Marienfeld GmbH
Nitrile Medical Examination Gloves	ABENA
Parafilm „M“	Bemis
Petri Dish 10 cm, not TC-treated	Corning Incorp.
Pipets, 1 µl - 1000 µl	Gilson
Pipetboy	Hirschmann
Plate 6 Well, not TC-treated	Corning Incorp.
Plate printer D300e	Tecan
Polystyrene Round-Bottom Tube 5 ml	Corning Incorp.
Power Pac™ Basic	Bio-Rad
Pre-Separation Filter 70 µm	Miltenyi Biotech

Precision scale Entris 22	Sartorius
Precision scale Entris 82	Sartorius
Preparation devices	Fine Science Tools
Primovert microscope	Carl Zeiss AG
Quadro MACS magnet	Miltenyi Biotech
Quantus Fluorometer	Promega GmbH
Reaction tube roller RS-TR05	Phoenix Instruments
Rotation microtome RM2245	Leica Camera AG
Safe-Lock Tubes 1.5 and 2.0 ml	Eppendorf GmbH
Safe Seal-Tips® professional	Biozym
Spark 10M	Tecan
Steriflip-HV	Merck Millipore
T100™ Thermal Cycler	Bio-Rad GmbH
Table centrifuge SU1550	Sustainable Lab Instruments
TC20™ Automated Cell Counter	Bio-Rad GmbH
TC T75 flasks, vented cap	Sarstedt
Terralin® liquid	Schülke
Thermomixer C	Eppendorf GmbH
Tissue culture dish 10 cm	Corning Incorp.
Tissue embedding system EG1150 C/H	Leica Camera AG
Tissue processor TP1020	Leica Camera AG
Trans-Blot® Turbo™ Transfer System	Bio-Rad GmbH
Trypan blue (0.4%)	Bio-Rad GmbH
Ultra-Low temperature freezer U275-G	Eppendorf GmbH
Vortex-Genie2™	Scientific Industries
Water bath HI1210	Leica Camer AG

Chemicals & Enzymes

1-Thioglycerol	Promega
Agarose	Biozym Scientific
Ammoniumchloride	Sigma-Aldrich GmbH
Antibody Diluent / Block	PerkinElmer
Aqua ad injectabile	B. Braun Melsungen AG
Bromphenol blue	Sigma-Aldrich GmbH
Blocking solution	Zytomed Systems
Collagenase	Gibco
DAPI	Thermo Fisher Scientific
Dispase	Gibco
DMEM Medium	Life Technologies Corp.
DMOG	Sigma-Aldrich GmbH
DNase I	Roche GmbH
Dulbecco's PBS, cell culture grade	Life Technologies Corp.
EDTA	Sigma-Aldrich GmbH
Ethanol 70% / 96%	University hospital pharmacy
Extracellular Flux Assay Kits	Agilent
Fetal Bovine Serum	Gibco
Gemcitabine	Biozol Diagnostica
Glucose 1.1 M	Thermo Fisher Scientific
Glutamine	Sigma-Aldrich GmbH
Glycerol	Sigma-Aldrich GmbH
Isofluoran CP	CP-Pharma
KAPA2G™ Fast HS Genotyping Mix	KAPA Biosciences Inc.
LightCycler® 480 SYBR Green I	Roche GmbH
Master Mix	Roche GmbH
Maxwell® simply RNAcells Kit	Promega GmbH
Mayer's hemalaun solution	Merck KgaA
Na-Pyruvate	Biochrom AG

Na-hydroxide	Carl Roth GmbH
Non-Essential Amino Acids	Biochrom AG
Nuclease free water	Promega GmbH
Opal Fluorophores	PerkinElmer
Paraformaldehyde (4%)	Santa Cruz Biotech
Penicillin/ Streptomycin	Life Technologies Corp.
PeqGOLD DNA Ladder Mix	Peqlab GmbH
PERTEX® mounting medium	Medite GmbH
Plus Automation Amplification Diluent	PerkinElmer
Poly (ethylene glycol) 200	Sigma-Aldrich GmbH
Potassiumhydrogencarbonate	Sigma-Aldrich GmbH
PrimeScript™ RT Master Mix	Takara Bio
Propidium iodide	Thermo Fisher Scientific
Proteinase K	Roche GmbH
Red Blood Cell Lyzing Buffer Hybri-Max™	Sigma-Aldrich GmbH
RNase Zap™	Sigma-Aldrich GmbH
Roti®-Histol	Carl Roth GmbH
RPMI-Medium 1640 (1x) + GlutaMAX™	Life Technologies Corp.
Saponin	Sigma-Aldrich GmbH
Shot bottles 100 ml – 1000 ml	DWK Life Sciences GmbH
Sodiumdodecylsulfate	Carl Roth GmbH
SuperSignal™ West Dura Extended Duration Substrate	Thermo Scientific
Trametinib	Biomol
Trans-Blot® Turbo™ 5x Transfer buffer	Bio-Rad GmbH
Tris-Ultra	Carl Roth GmbH
Triton® X 100	Carl Roth GmbH
Trypsin	Life Technologies Corp.
Tween20	Carl Roth GmbH
VECTASHIELD® mounting medium	Vector Labs Inc.

XF Base Medium Minimal DMEM	Agilent Technologies
XF Calibrant solution	Agilent Technologies
β-Mercaptoethanol	Sigma-Aldrich GmbH

Buffers & Solutions

ACK lysis buffer	8.28 g ammoniumchloride 1 g potassiumhydrocarbonate 37.2 mg di-sodium EDTA adjust pH to 7.2-7.4 with 37% HCl add to 1000 ml with ddH_2O
FACS buffer	D-PBS 2% FBS
Homogenization buffer	Homogenization solution 2% 1-Thioglycerol
Permeabilization buffer	D-PBS 0.1% w/v Saponin
Running buffer (10x)	144 g Glycin 30 g Tris 10 g SDS add to 1000 ml with ddH_2O
SDS loading buffer (6x)	7 ml 0.5 M Tris-HCl pH 6.8 3 ml 30% glycerol 1 g SDS 1.2 mg bromphenol blue add β-mercaptoethanol always freshly

TAE buffer, pH 8.0	100 ml EDTA, 0.5 M 57.1 ml glacial acetic acid 242 g Tris ddH_2O add to 1 l
1x TBS-T	20 mM Tris 150 mM NaCl 0.1% Tween 20
Transfer buffer (1x)	200 ml Trans-Blot® Turbo™ 5x Transfer buffer 200 ml ethanol 600 ml ddH_2O
Tumor dissociation buffer	10 ml Tumor medium 0.1 g Collagenase (≥ 125 CDU/mg) 0.1 g Dispase (1,76 Units/mg) 100 µl DNase I (10 mg/ml)

Culture Media

Macrophage medium	RPMI Medium 1640 (1x) + GlutaMAX™ 20% FBS 1% Non-Essential Amino Acids 1% Sodium Pyruvate 1% Penicillin/Streptomycin
Macrophage differentiation medium	Macrophage medium 50 ng/µl murine M-CSF

Macrophage polarization medium (M1)	Macrophage medium 1 µg/ml LPS 40 ng/µl IFNγ
Macrophage polarization medium (M2)	Macrophage medium 40 ng/µl IL-4 40 ng/µl IL-13
Tumor medium	DMEM (1x) 10% FBS
MitoStress assay medium	XF Base Medium Minimal DMEM 1% Na-pyruvate (100x) 1% Glutamine 1% 1.1M Glucose adjust pH 7.4 with 0.1 M NaOH
GlycoStress assay medium	XF Base Medium Minimal DMEM 2 mM Glutamine adjust pH 7.4 with 0.1 M NaOH

Primers

Genotyping Primers

Table 2.1: Genotyping primers

Primer	Sequence
Cre	ACCAGCCAGCTATCAACTCG
$Kras^{LSL-G12D}$	CACCAGCTTCGGCTTCCTATT
$p53^{fl}$	CACAAAAACAGGTTAAACCCA

qRT-PCR Primers

Table 2.2: qRT-PCR Primers

Primer	Sequence
qmArg1_for	ATCGGAGCGCCTTTCTCAAA
qmArg1_rev	GGTCTCTCACGTCATACTCTGT
qmIL12p35_for	TCCCGAAACCTGCTGAAGAC
qmIL12p35_rev	CTGGTTTGGTCCCGTGTGAT
qmIL12p40_for	GAGTGGGATGTGTCCTCAGAA
qmIL12p40_rev	GTCCAGTCCACCTCTACAACA
qmIL1b_for	TGCCACCTTTTGACAGTGATG
qmIL1b_rev	ATGTGCTGCTGCGAGATTTG
qmIL6_for	ACTTCACAAGTCGGAGGCTT
qmIL6_rev	TGCAAGTGCATCATCGTTGT
qmJmjd3_for	CTGTAGCCCATAGGACCCAC
qmJmjd3_rev	GTCTCCGCCTCAGTAACAGC
qmMgl1_for	GGAAGCCAAGACTTCACACTG
qmMgl1_rev	CTGGACGGAAACCAAGACAC

qmCD206_for	AACAAGAATGGTGGGCAGTC
qmCD206_rev	TTTGCAAAGTTGGGTTCTCC
qmiNOS_for	CGTGAAGAAAACCCCTTGTGC
qmiNOS_rev	GGAACATTCTGTGCTGTCCCA
qmIL10_for	AGGCGCTGTCATCGATTTCT
qmIL10_rev	ATGGCCTTGTAGACACCTTGG
qmCyclophilinA_for	ATGGTCAACCCCACCGTG
qmCyclophilinA_rev	TTCTGCTGTCTTTGGAACTTTGTC
qmIL1A_for	CGCTTGAGTCGGCAAAGAAAT
qmIL1A_rev	CTTCCCGTTGCTTGACGTTG
qmMGL2_for	ACTTCCAGAACTTGGAGCGG
qmMGL2_rev	ACTGGGAAGGAATTAGAGCAAACT
qmCISH_for	GGGACATGGTCCTTTGCGTA
qmCISH_rev	GTACCACCCAGATTCCCGAAG
qmSELP_for	AGCAGGGACACTGACAATCC
qmSELP_rev	ACCGGGTTTCTTAAGGGGTT
qmSLC2A1_for	GAGGAGCTCTTCCACCCTCT
qmSLC2A1_rev	TCCTCCTGGACTTCACTGC
qmVEGFA_for	ACTGGACCCTGGCTTTACTG
qmVEGFA_rev	ACTTGATCACTTCATGGGACTTCT
qmPHD3_for	GGCCGCTGTATCACCTGTAT
qmPHD3_rev	GGCTGGACTTCATGTGGATT

Antibodies

Flow Cytometry Antibodies

Table 2.3: Flow cytometry antibodies

Antigen	Dilution	Clone	Manufacturer	Conjugate	Isotype	Reactivity
CD14	1:100	HCD14	Biolegend	PE	Mouse IgG1	Human
CD16	1:100	3G8	Biolegend	PE	Mouse IgG1	Human
CD86	1:100	IT2.2	Biolegend	PE/Cy5	Mouse IgG2b	Human
CD163	1:100	GHI/61	Biolegend	FITC	Mouse IgG1	Human
CD206	1:100	15-2	Biolegend	PE/Cy5	Mouse IgG1	Human
HLA-DR	1:100	L243	Biolegend	FITC	Mouse IgG2a	Human
CD11b	1:80	M1/70	Biolegend	PE/Cy5	Rat IgG2b	Mouse
CD11b	1:80	M1/70	Biolegend	eFluor450	Rat IgG2b	Mouse
CD80	1:20	16-10A1	BioLegend	BV-421	Armenian Hamster IgG	Mouse
CD206	1:30	C068C2	BioLegend	BV650	Rat IgG2a	Mouse
CD301	1:80	LOM-14	BioLegend	PE/Cy7	Rat IgG2b	Mouse
F4/80	1:100	BM8	Biolegend	FITC	Rat IgG2a	Mouse
NOS2	1:100	CXNFT	eBioscience	PE	Rat IgG2a	Mouse

Magnetic Activated Cell Sorting Antibodies

Table 2.4: MACS antibodies

Antigen	Conjugate	Manufacturer	Reactivity
CD14	Microbead-coupled	Miltenyi Biotech	Human

Immunohistochemistry Antibodies

Table 2.5: Immunohistochemical antibodies

Antigen	Clone	Manufacturer	Isotype	Dilution	Reactivity
CD11b	Polyclonal	Abcam	Rabbit IgG	1:500	Mouse
F4/80	BM8	BMA biomedicals	Rat IgG2a	1:200	Mouse
CD206	Polyclonal	Abcam	Rabbit IgG	1:200	Mouse
CD163	EPR19518	Abcam	Rabbit IgG	1:500	Mouse
Nos2	Polyclonal	Abcam	Rabbit IgG	1:200	Mouse

Immunofluorescence Antibodies

Table 2.6: Immunofluorescence antibodies

Antigen	Clone	Manufacturer	Dilution & Opal Fluorophor	Reactivity
pERK1/2	D13.14.3E	Cell Signaling	1:500 , Opal 570 /620	Human
CD68	KP1	Abcam	1:100 , Opal 520	Human
GATA6	H-92	Santa Cruz	1:50 , Opal 620	Human
KRT81	36-Z	Santa-Cruz	1:100 , Opal 570	Human
panCK	PCK-26	Abcam	1:400 , Opal 647	Human

Western Blot Primary Antibodies

Table 2.7: Western blot primary antibodies

Antigen	Clone	Manufacturer	Dilution	Reactivity
HIF1A	Polyclonal	Cayman Chemical	1:1000	Mouse
β-Actin	Polyclonal	Abcam	1:10000	Mouse

Western Blot Secondary Antibodies

Table 2.8: Western blot secondary antibodies

Specificity	Clone	Manufacturer	Dilution	Reactivity
IgG (H+L)	Polyclonal	Jackson Immuno Research	1:30000	Rabbit

Recombinant Proteins

Table 2.9: Recombinant proteins

Recombinant protein	Manufacturer
Interferon γ, murine	PeproTech GmbH
Interleukin-4, murine	PeproTech GmbH
Interleukin-13, murine	PeproTech GmbH
Lipopolysaccharide (E.coli O55:B5)	Sigma-Aldrich GmbH
Macrophage Colony-Stimulating Factor, murine	PeproTech GmbH

Mouse Strains

Tumors from *Ptf1a*$^{wt/Cre}$*; Kras*$^{wt/LSL-G12D}$*; Trp53*$^{fl/fl}$ (termed *CKP* hereafter) mice were used as spontaneous PDAC tumor model and have been previously described (Ardito et al. 2012; Mazur et al. 2015).C57BL/6 mice were used to obtain bone marrow-derived macrophages.

Table 2.10: List of mouse strains

Gene	Genetic modification	Strain	Reference
Ptf1a^{cre}	*Cre* knock-in	*Ptf1a*$^{tm1(cre)Hnak}$	(Nakhai et al. 2007)
Trp53	*LoxP*-sites knock-in	*Trp53*^{tm1Brn}	(Marino et al. 2000)
Kras	*LSL-KRASG12D* knock-in	*Kras*^{tm1Dsa}	(Jackson et al. 2001)

Table 2.11: Mouse strains

Strains intercrossed	Strain (abbreviated)	Action	Genotype
Ptf1a$^{cre/+}$ *Kras*$^{LSL\text{-}G12D/+}$ *Trp53*$^{-/-}$	CKP	Cre-induced spontaneous PDAC through pancreas-specific activation of oncogenic KRAS^{G12D} and homozygous loss of tumor protein p53	*Ptf1a*$^{wt/Cre}$; *Kras*$^{wt/LSL\text{-}G12D}$; *Trp53*$^{fl/fl}$
-	C57BL/6	Wildtype	Wildtype

Software

2200 TapeStation Controller	Agilent
Cytoscape	Cytoscape Consortium
D300eControl	Tecan
Definiens Architect XD 64	Definiens
Enrichment Map	The Bader Lab
FACS Diva™ 8.0.1.1	BD Biosciences Inc.
FlowJo 10.5.3	Tree Star Inc.
GraphPad Prism 8	GraphPad Software Inc.
GSEA v3.0	Broad Institute Inc.
Ingenuity Pathway Analysis	QIAGEN
LightCycler® 480 SW 1.5	Roche GmbH
NanoDrop 200 1.4.1	Thermo Fisher Scientific
Pro Sort Ink.	Bio-Rad GmbH
RSC Software	Promega
RStudio version 3.6.0	RStudio Inc.

Servier Medical Art	Les Laboratoires Servier
SPARKCONTROL Dashboard	Tecan
Tick@Lab	A-Tune Software AG
Wave 2.4.1	Agilent
ZEN 2.6 (blue edition)	Carl Zeiss AG

Methods

Nucleic Acid-Related Techniques

Isolation of RNA From Cells

Macrophages were washed and rinsed with ice-cold PBS before removal from cell culture dishes on ice by cell scraping and cells were centrifuged for 4 min at 1400 rpm on 4 °C. Following centrifugation, cell pellets were resuspended in 200 µl homogenization buffer containing 5% 1-Thioglycerol and 200 µl lysis buffer was added. After vortexing, samples were applied to the Maxwell RSC machine and total RNA was isolated by running the simplyRNA cell program. Isolated RNA was captured in 35 µl RNase free H_2O and, if not immediately processed, stored at -80 °C until further analysis. To avoid sample contamination by RNases, working space and equipment were cleaned with RNaseZAP™ before respective experiments.

Quantification of RNA Concentration

Following total RNA isolation, RNA concentrations were determined either spectrophotometrically with NanoDrop2000c or fluorometrically with Maxwell RSC machine using the integrated Quantus™ fluorometer. For determining RNA concentrations with NanoDrop2000c, 1 µl of isolated RNA sample was applied onto the spectrophotometer and measured values were normalized onto prior measured blank control. Samples with a 260/280 ratio higher than approximately 1.9 as well as a 260/230 ratio higher than 2.0 were taken into account for further experimental analysis. For RNA concentration determination using the Quantus™ fluorometer, QuantiFluor® RNA dye was diluted 1:200 with 1x TE and 100 µl of diluted RNA dye was added to 98 µl 1xTE and 2 µl of isolated RNA sample. Concomitantly, 100 µl of RNA dye was added to 100 µl 1xTE for blank control. Furthermore, 100 µl RNA dye was added by 95 µl 1xTE and 5 µl RNA (100 ng/µl) for preparation of a RNA standard. All samples were mixed thoroughly and incubated on RT in the dark for 5 min prior to measurement in the fluorometer.

Reverse Transcriptase Polymerase Chain Reaction

Isolated total RNA was reversely transcribed to cDNA by PrimeScript™ RT reagent Kit from TaKaRa according to the manufacturer's protocol. Prior to reverse transcription, RNA samples were diluted in ddH_2O to equalize RNA amounts in each sample. 500 ng of RNA were reversely transcribed in a 10 µl reaction mixture on ice. If higher amounts of RNA were reversely transcribed, reaction mixture volume was adjusted respectively. Per reaction, 2 µl of 5x PrimeScript Buffer were mixed with 0.5 µl PrimeScript RT Enzyme Mix I, 0.5 µl Oligo dT Primer (50 µM), 0.5 µl Random 6 mers (100 µM) and

respective volume of RNA sample. Samples were filled up to 10 µl with RNase free ddH_2O. Reverse transcription was conducted by incubating reaction mix for 15 min at 37 °C followed by 5 sec at 85 °C for enzyme inactivation. Samples were diluted 1:5 with ddH_2O and either used immediately for quantitative real-time PCR or stored at -80 °C.

Primer Design

Primer for qRT-PCR were designed using NCBI Primer Blast website (www.ncbi.nlm.nih.gov/tools/primer-blast) and ordered at Eurofins MWG Operon GmbH. Whenever possible, exon-junction spanning primer pairs were preferred and PCR products were designed to a size of approximately 100-150 bp. Lyophilized primers were dissolved in ddH_2O to a stock concentration of 100 µM.

Quantitative Real-Time Polymerase Chain Reaction

Quantitative real-time PCR (qRT-PCR) was performed to investigate gene expression and treatment-induced gene expression changes by using a Roche LightCycler® 480 with LightCycler® 480 SYBR Green I Master Kit in a 96 well format. Primers for qRT-PCR were designed as described above. Primer pairs were combined to a 0.5 µM stock solution and 0.5 µl were added to 5 µl SYBR Green Master Mix per reaction. Additionally, 4.5 µl of cDNA dilution was added to each reaction and the 10 µl reaction solution was centrifuged for 1 min at 1000 rpm. All quantitative real-time PCRs were run at 59 °C annealing temperature with 45 amplification cycles. A melting curve was implemented to prove single product amplification and a no-template control containing H_2O was included in each experiment to exclude contamination and primer-dimer amplification. Data were analyzed using ΔC_T calculations where Cyclophilin A served as reference control for normalization. Amplification efficacy was experimentally determined or assumed as 2. Expression values for genes from M0 macrophages are displayed as ΔC_T value. Fold change expression of respective macrophage subsets were calculated by normalizing ΔC_T values to the unstimulated M0 state. Fold changes were averaged and analyzed by Mann-Whitney test. For fold change expression after MEKi treatment, ΔC_T values of vehicle treated subsets were subtracted from ΔC_T values of respective MEKi treated subsets. Fold changes were averaged and analyzed by Mann-Whitney test.

Table 2.12: qRT-PCR target genes, primer names and product sizes

Target gene	Primer	Product size
Arg1	qmArg1_for, qmArg1_rev	118 bp
Cd206	qmCD206_for, qmCD206_rev	128 bp
Cish	qmCish_for, qmCish_rev	102 bp
CyclophilinA	qmCyclophilinA_for, qmCyclophilinA_rev	102 bp
Il12a (p35)	qmIL12p35_for, qmIL12p35_rev	119 bp
Il12b (p40)	qmIL12p40_for, qmIL12p40_rev	120 bp
Il1a	qmIL1A_for, qmIL1A_rev	271 bp
Il1ϐ	qmIL1b_for, qmIL1b_rev	136 bp
Il6	qmIL6_for, qmIL6_rev	111 bp
Il10	qmIL10_for, qmIL10_rev	104 bp
Jmjd3	qmJmjd3_for, qmJmjd3_rev	108 bp
Mgl1	qmMgl1_for, qmMgl1_rev	111 bp
Mgl2	qmMgl2_for, qmMgl2_rev	254 bp
Nos2	qmiNOS_for, qmiNOS_rev	108 bp
Selp	qmSELP_for, qmSELP_rev	218 bp
Slc2a1	qmSlc2a1_for, qmSlc2a1_rev	191 bp
Vegfa	qmVegfa_for,qmVegfa_rev	185 bp
Phd3	qmPhd3_for, qmPhd3_rev	167 bp

Table 2.13: qRT-PCR amplification program

	Temperature	Duration
Preincubation	95 °C	5 min
Amplification	95 °C	20 s
(45 cycles)	59 °C	20 s
	72 °C	20 s
Melting curve	95 °C	5 min
	65 °C	1 min
	97 °C	contin.
Cooling	37 °C	30 s

RNA Integrity Measurement

RNA samples which were further processed for RNA sequencing were additionally analyzed for their RNA integrity by measuring the RNA integrity number (RIN) in an Agilent 4200 TapeStation using an RNA ScreenTape assay. Therefore, RNA samples were thawed on ice and a running ladder was prepared by mixing 5 µl RNA sample buffer with 1 µl RNA Ladder. Furthermore, 1 µl of RNA sample was mixed with 5 µl RNA sample buffer and spun down for 10 sec. Samples were vortexed, centrifuged and denaturized by heating them at 72 °C for 3 min followed by placing them on ice for 2 min. Afterwards, samples were spun down prior to loading them into the 4200 TapeStation instrument. Following the run, samples were controlled for their RIN value and samples were diluted to a final concentration of 100 ng/µl in 5 µl RNase free H_20 to be further analyzed by RNA sequencing.

Genotyping PCR

Genetically engineered mice (CKP) were genotyped from lyzed biopsies obtained from ear punches at an average of four weeks of age. 1 µl genomic DNA lysate was added to 20 µl PCR reaction, which contained primers at 0.5 µM and 10 µl of either 2x RedTaq® Ready Mix, for $Ptf1a^{Cre}$ and $Kras^{LSL\text{-}G12D}$, or 2x KAPA2G Fast HS Genotyping Mix for $p53^{fl}$ allele. PCR was performed with initial denaturation for 5 min at 95 °C followed by 38 cycles composed of 30 sec 95 °C denaturation, 30 sec 58 °C primer annealing and 1 min 72 °C for prolongation.

Table 2.14: *CKP* genotyping wildtype and mutated product size

Target gene	Primer	Wildtype product size	Mutated product size
Cre	mG_Cre001	324 bp	199 bp
Kras$^{LSL-G12D}$	mG Kras_wt_UP1	280 bp	180 bp
p53^{fl}	p53-loxP-1	288 bp	332 bp

Agarose Gel Electrophoresis

Genotyping PCR products were loaded on a 2% agarose/TAE buffered gel for separation of amplified DNA fragments. For visualization of DNA, 5 µl of 1 mg/ml ethidiumbromide solution was added per 100 ml agarose gel and 15 µl of each amplified sample was loaded into a gel pocket. For size estimation of separated fragments, 10 µl of peqGOLD DNA Ladder Mix was included in each electrophoresis run. Samples were separated by 120 V and DNA fragments were visualized under under UV light and documented in a BioRad gel documentation chamber.

Cell Culture Techniques

Isolation of Murine Bone Marrow-Derived Precursor Cells

Murine bone marrow-derived cells were isolated from healthy C57BL/6 mice aged between 8 and 12 weeks. Mice were killed by cervical dislocation and immediately subjected to isolation of bone marrow from *femur* and *tibia*. Bone marrow cells were collected by flushing the bone cavity with cold RPMI medium. Flow-through was collected and centrifuged at RT for 5 min at 1400 rpm. The supernatant was aspirated and red blood cells were lyzed using 500 µl Red Blood Cell Lysis Buffer per mouse for 7 min at RT. Lysis was stopped by addition of 30 ml cold RPMI medium. Cells were centrifuged at RT for 5 min at 1400 rpm and cells were resuspended in macrophage medium (RPMI, 20% FBS, 1% NEAA, 1% sodium pyruvate) containing 50 ng/ml murine M-CSF. Following, cells were counted and cell viability was determined by counting trypan blue stained and unstained cells using a Neubauer counting chamber. After cell number determination, cells were seeded and cultured in macrophage differentiation medium.

Murine Macrophage Differentiation From Bone Marrow-Derived Precursor Cells

Bone marrow-derived precursor cells were differentiated to macrophages by cultivating them for 5 days in macrophage differentiation medium containing 50 ng/ml M-CSF. After 3 days, medium was replenished with 3 ml fresh macrophage differentiation medium. Macrophage differentiation was assessed by CD11b and F4/80 co-expression using flow cytometry and cultured cells were named as bone marrow-derived macrophages (BMDMs) hereafter.

Induction of Murine Pro-Inflammatory M1-like Macrophages

For murine pro-inflammatory M1-like BMDM polarization, macrophages were incubated in macrophage polarization medium containing 1 µg/ml LPS and 4 ng/ml IFNγ (M1) without M-CSF overnight at 37 °C.

Induction of Murine Anti-Inflammatory M2-like Macrophages

For murine anti-inflammatory M2-like BMDM polarization, macrophages were incubated in macrophage polarization medium containing 40 ng/ml IL4 and 40 ng/ml IL13 (M2) without M-CSF for 48 h at 37 °C.

Isolation of Human Monocytes from Peripheral Blood

Human $CD14^+$ monocytes were isolated from buffy coats of healthy donor individuals from the Department of Transfusion Medicine at the University Hospital Essen. For monocyte isolation, human blood was separated using Ficoll gradient centrifugation as well as magnetic activated cell sorting (MACS) cell separation for $CD14^+$ cells. The donor's blood was slowly layed onto Ficoll at a 1:1 ratio, prior to centrifugation at RT for 20 min at 400xg without break to enable separation of leukocyte fraction. The leukocyte layer at the interfaces were collected and centrifuged at 1400 rpm for 5 min and then subjected to red blood cell lysis with 5 ml ACK lysis buffer for 90 sec at RT. Lysis was stopped by addition of 25 ml RPMI medium and cells were centrifuged again at RT for 5 min at 1400 rpm. Cells were resuspended in 1 ml 1% BSA/RPMI medium and counted. Afterwards, $1x10^8$ cells were resuspended in 800 µl 1% BSA/RPMI medium and 200 µl of CD14 antibody-coupled magnetic beads were added to the suspension. The cells were incubated with the CD14-directed antibody-coupled beads for 45 min on ice. Following, cells were washed with 19 ml 1% BSA/RPMI medium, centrifuged at RT for 5 min at 1400 rpm and resuspended in 5 ml 1% BSA/RPMI medium. LS columns were placed into a Quadro MACS magnet and pre-wetted with 5 ml PBS. Afterwards, the cell

suspension was applied onto the column, where $CD14^+$ cells, which were bound to microbead-conjugated anti-CD14 antibody were retained inside the column The columns were removed from the Quadro MACS magnet and placed onto a collection tube containing 2 ml of 1% BSA/RPMI medium. The columns were pre-wet with 5ml PBS. Columns were then flushed with 5 ml 1% BSA/RPMI medium using a plunger for collecting the $CD14^+$ cells. After collection, cells were centrifuged at RT for 5 min at 1400 rpm. The cell pellet was resuspended in 1 ml 1% FBS/RPMI medium. Cells were counted and $2x10^5$ monocytes were seeded into a 6 well in 3 ml 10% FBS/DMEM medium as control or in 3 ml tumor-conditioned medium from human pancreatic cancer cell lines (see following chapter).

Induction of Murine and Human Tumor-Associated Macrophages

Indirect Co-Culture

To induce murine tumor-associated macrophage (TAM) phenotype, BMDMs (M0 macrophages) were incubated for 48 h with conditioned medium from murine pancreatic cancer cell lines 60400, 70301, 70202 and 60590. To induce human TAMs, isolated monocytes were incubated for 72 h in conditioned medium from human pancreatic cancer cell lines HupT4, HPAC, PaTuS, MiaPaCa2, PSN-1 and PaTuT. For obtaining tumor-conditioned medium for mouse and human, tumor cells were routinely split to reach approximately 70% - 80% confluency after 72 h. Tumor-conditioned medium was collected and centrifuged for 5 min at 1400 rpm. Afterwards, medium was either used immediately for macrophage polarization or stored at -80 °C for further experiments. To investigate differences regarding tumor subtype-specific TAM polarization, cells were incubated with conditioned medium from epithelial or mesenchymal murine or human pancreatic cancer cell lines. The classification of murine cancer cells into different subtypes was based on transcriptomic analysis, as well as expression of epithelial and mesenchymal marker proteins E-Cadherin and N-Cadherin determined by western blot analysis previously in our group. The classification of human pancreatic cancer cell lines into epithelial or mesenchymal subtype was based on gene expression of E-cadherin and vimentin analyzed by qRT-PCR and published data (Daemen et al. 2015). Cells were always incubated with fresh tumor conditioned medium at the beginning of each experiment and prior to MEKi treatment.

Direct Co-Culture

Tumor cells from epithelial and mesenchymal PDAC subtypes were seeded and then co-cultured with murine BMDMs to enable direct physical interaction. Therefore, tumor cells and macrophages were seeded into 6 well plates at different tumor-immune cell ratios and incubated for 72 h at 37 °C. After incubation, cells were harvested and subjected to flow cytometric analysis for marker expression.

Tumor Digestion into Disaggregated Cells

Spontaneous PDAC mouse model CKP mice were sacrificed by cervical dislocation and pancreatic tumors were collected. All mice were routinely examined for metastatic seeding to the liver lobes and lung by histology. Tumors were minced and centrifuged at RT for 5 min at 300 rpm. Tissue pellets were digested with 5 ml tumor dissociation buffer and incubated for 20 min in a 37 °C incubator with constant shaking. Tissues were centrifuged at RT for 5 min at 300 rpm and supernatant, which contained disaggregated cells, was transferred into a collection tube containing 10 ml of cold 10% FBS/DMEM medium. The digestion/centrifugation circle was repeated twice. Afterwards, cell suspension was filtered through a 70 µm cell strainer to allow single cell separation. The cell suspension was centrifuged at RT for 5 min at 800 rpm and cell pellet was resuspended in 5 ml ACK lysis buffer for 7 min to lyse red blood cells. The reaction was stopped by adding 25 ml cold 10% FBS/DMEM medium, and cells were then centrifuged and the pellet was resuspended in 10 ml 10% FBS/DMEM medium. Cell number and viability were determined by staining with trypan blue (0,4%) and counted with a Neubauer counting chamber. For subsequent immunofluorescent staining, $1x10^5$ cells were transferred into each FACS tube for further analysis. Furthermore, only digested samples with cell viability higher than 85% were taken for further experiments.

Immunohistological Stainings

Preparation of Paraffin-Embedded Tumor Tissue

After dissection, pancreatic tumors and spleen were collected in tissue cassettes and incubated in 4% PFA/PBS overnight at 4 °C. The PFA-fixed tissues were dehydrated overnight using a Leica ASP300S dehydrator and embedded in paraffin using a Leica EG 1150 H. Paraffin embedded tissue blocks were stored at 4 °C or at RT before slicing. 2 µm sections were cut from the blocks using a Thermo Scientific Microm HM 355S microtome. Afterwards, sections were placed onto microscope slides and dried at RT overnight.

Hemalaun & Eosin Staining

Paraffin embedded sections were routinely examined by H&E staining. Hemalaun is an acidophilic substance which stains nuclei within the section whereas eosin is basophilic and stains cytoplasm. Slides were incubated for 2 min in Roti®-Histol three times for paraffin removal. Afterwards, slides were treated three times with absolute ethanol followed by two times with ddH_2O. The slides were incubated for 5 min in Mayers's hemalaun solution and washed three times with ddH_2O. Following, sections were dipped in ammonia water and two times in ddH_2O. Next, slides were dipped two times in HCl-H_2O before tap water flushing. Sections were incubated briefly in ammonia water, rinsed two times with ddH_2O and dipped in 70% ethanol. Cytoplasmic staining was achieved by incubating sections for 2 min in eosin solution followed by dipping slides three times in absolute ethanol. Tissue was then mounted with PERTEX® mounting medium and covered with cover slip.

Immunohistochemistry

Immunohistochemical staining was performed using Dako REAL™ Alkaline Phosphatase Detection System following manufacturer's instructions. Slides were placed into oven (60 °C) overnight and dewaxed using an autostainer. Antigen retrieval of formalin-fixed paraffin-embedded (FFPE) sections was achieved by heat-induced epitope retrieval in a microwave using citrate buffer (pH 6) for CD11b and CD206, Tris/EDTA (pH 9) for CD163 and Nos2, and proteinase K treatment for F4/80. Slides were transferred into boiling buffer and incubated for 5 min at maximum power in the microwave before incubation for 20 min at 360 W. Afterwards, slides were cooled down by incubation for 30 min at RT. Slides were washed with ddH_2O for 5 min and tissue was circled with a hydrophobic pen. Slides were washed with ddH_2O for 5 min and with 0.01% TBS-T for 5min. Following blocking with Dako non-serum blocking buffer for 1 h at RT, slides were incubated with respective primary antibody for 1 h at RT (Table 2.5). Slides were washed three times with TBS-T for 5 min and rinsed in TBS before incubation with AP one-step polymer secondary antibody for 30 min at RT. After washing with TBS-T for 5min three times and with TBS once, signal was developed with Zytomed AP Permanent Red Kit. The signal developing reaction was stopped by transfering the slides into ddH_2O and slides were counterstained with hematoxylin, dehydrated in the autostainer and mounted. Respective isotype controls were used for each antibody and spleen was stained as positive control to ensure proper marker staining (Table 2.5).

Multiplex Immunofluorescence

Immunofluorescent staining was performed using PerkinElmer Opal Multiplex Immunohistochemistry Kit following manufacturer's instructions. Slides were placed into oven (60 °C) overnight and dewaxed using an autostainer Following, slides were incubated for 20 min on RT in 4% PFA/PBS and antigen retrieval was achieved by heat-induced epitope retrieval in a microwave using citrate buffer (pH 6) for pERK1/2 and Tris/EDTA (pH 9) for CD68, GATA6 and panCK. Slides were transferred into boiling buffer and incubated for 5 min at maximum power in the microwave before incubation for 20 min at 360 W. Afterwards, slides were cooled down by incubation for 30 min at RT. Slides were rinsed with ddH_2O and tissue was circled using a hydrophobic pen. Slides were washed 5 min with ddH_2O followed by 5 min with TBS-T. Following washing, slides were incubated with 3% H_2O_2 for 10 min at RT, washed twice with ddH_2O and once with TBS-T and blocked for 7 min. The slides were washed with TBS-T for 5 min and blocked for 30 min before incubation with primary antibody for 1 h at RT (Table 2.6). Slides were washed three times with TBS-T for 5 min before incubation for 30 min at RT with the HRP-coupled secondary antibody. After washing three times with TBS-T for 5 min, slides were stained with the respective Opal fluorophores (1:200 in Plus Automation Amplification Diluent) for 10 min at RT in the dark. Slides were washed 3 times with TBS-T for 5 min and the steps including antigen retrieval, blocking and antibody/ OPAL incubation were repeated until all targets of interest were detected, using a different OPAL fluorophore for each target protein (Table 2.6). Slides were rinsed with ddH_2O and transferred into boiling pH 6 antigen retrieval buffer and incubated for 5 min at maximum power in the microwave before incubation for 10 min at 360 W. Afterwards, slides were cooled down by incubation for 30 min at RT, washed twice for 5 min with TBS-T and once for 5 min with TBS. Slides were mounted with DAPI and applied for scanning.

Microscopy & Cellular Quantification

Digital Whole Slide Scanning

Whole slide scanning and digitalization was performed using the Zeiss AxioScan.Z1 with 2.5x and 10x magnification. Images were captured using Zeiss ZEN 2.6 (blue edition) software.

Cellular Quantification of Immunohistochemical Staining

For cellular quantification of positive cells within a stained tissue section, slides were quantified by the Definiens Architect XD 64 software. Total cell and positive cell number from 5 representative images of a stained tissue section were quantified to determine the percentage of positive cells per

mouse. Areas of extensive immune cell infiltration, e.g. infiltrating lymph nodes or tertiary lymphoid structures, were avoided.

Flow Cytometric Analysis

Flow Cytometry

Multi-color flow cytometry experiments were performed on a BD Celesta flow cytometer. Three lasers (violet 488 nm, blue laser 405 nm, yellow/green laser 561 nm) and 13 filter sets allow for simultaneous detection up to 10 colors. Intra- and inter-laser beam spillover correction was calculated by FlowJo 10.5.3 software. Compensation matrices were, if needed, calculated by single stainings. To avoid unspecific background signal from unspecific antibody binding, respective isotype controls were used for each measurement. Fluorophore-conjugated antibodies were used in accordance to manufacturer's protocols. Samples were run in a volume of 150 µl-200 µl with up to $5x10^5$ cells per tube. PBS was used for cell resuspension prior to measurement.

Cell Surface Staining

For cell surface staining, $5x10^5$ cells per tube were centrifuged in PBS at 1400 rpm for 5 min at 4 °C. The supernatant was aspirated and cells were stained with fluorophore-conjugated antibodies for 30 min on ice in the dark. Following incubation, cells were washed with PBS and centrifuged at 1400 rpm for 5 min at 4 °C. Afterwards, the cell pellet was either resuspended in 150 µl-200 µl PBS and underwent flow cytometric analysis or subjected to subsequent staining for intracellular antigens.

Intracellular Staining

For intracellular staining, cells were permeabilized immediately after surface staining in 3 ml 0.1% Saponin/PBS for 20 min on ice in the dark with vigorous vortexing every 5 min. After permeabilization, cells were centrifuged on 4 °C for 5 min at 1400 rpm and antibodies were pre-diluted in permeabilization buffer to concentrations according to manufacturer's protocols (Table 2.3). The samples were stained for 30 min on ice in dark before addition of 3 ml 0.1% Saponin/PBS. After centrifugation, cells were resuspended in 150 µl-200 µl PBS and were subjected to flow cytometric analysis immediately.

Bioinformatic analysis

RNA Sequencing of *in vitro* Macrophages

RNA sequencing was conducted by the core facility for Next Generation Sequencing of the medical faculty of University Bonn. 50 ng total RNA were used with QuantSeq 3'mRNA-Seq Library Prep Kit FWD from Lexogen for library preparation of samples from *in vitro* polarized murine macrophages. The RNA was sequenced by Illumina HiSeq2500 in High Output Mode with 50 bases single-read mode with $1x10^7$ reads. All samples were sequenced on the same flow-cell. Reverse transcription, RNA removal and bead purification were conducted according to manufacturer's protocol.

Differential Gene Expression Analysis

RNA sequencing data were obtained as FASTQ files from the medical faculty of University Bonn. Biological samples were quantified using kmer-based tool salmon (v. 0.10.2) (Patro et al. 2017). First, a kmer-index was build over the 3'UTR regions of the reference genome GRCm3.p6 (Ensembl release 93) and transcript level quantification was performed applying the quasi-mapping algorithm of salmon. Following, phyton library pandas (v. 0.24.2) was applied for merging results per sample and the analysis was performed by the workflow management system snakemake (v. 5.1.4) (Koster and Rahmann 2018). Non-expressed genes were removed by setting the threshold to at least 2 reads/1000000 reads in two out of three biological samples per group. Reads were normalized with the DESeq2 package (v. 1.24.0) and genes were differentially expressed with $p \leq 0{,}05$ and $\log_2$ fold change≥ 1.

Gene Set Enrichment Analysis of Differentially Expressed Genes

Gene expression values for the different macrophage subtypes were ranked based on t-statistics and the pre-ranked gene expression files were analyzed by Gene Set Enrichment Analysis (GSEA). The expression datasets were analyzed against different gene set databases (hallmarks, KEGG, immunologic signatures) with 1000 permutations and phenotype as permutation type. The enrichment statistics was weighted and the treshold for minimum gene set size was set to 15 genes, while the threshold for maximum geneset size was set to 500 genes. Following processing, gene sets with a p-value <0.05 and a false discovery rate (FDR) <0.25 were further analyzed.

Leading Edge Analysis

Following GSEA, Leading Edge Analysis was performed to discover genes, which are part of the leading edge of selected enriched gene sets between the two biological phenotypes. It is assumed, that genes, which appear in the leading edge of multiple subsets have a higher probability to be of interest than those, which appear only in one or a few subsets. For Leading Edge Analysis, gene sets with a p-value <0.05 and a false discovery rate (FDR) <25% were selected and analyzed.

Enrichment Map

Enrichment Map was constructed with Cytoscape for functional enrichment visualization between two phenotypes, where mutually overlapping gene sets, which have been previously analyzed by GSEA, cluster together. Differentially enriched gene sets between two phenotypes are figured as nodes, whereas node size is corresponding to the gene number of the respective gene set. Furthermore, node color indicates the enrichment score for the respective gene set to one of the two biological phenotypes. Nodes can be connected by edges, which symbolize overlapping genes in the connected nodes. Additionally, edge width is correlated with the number of overlapping genes in two connected nodes. For visualization of the network landscape, networks that contain at least 3 different nodes (gene sets) were used for further analysis. p-values for node and edge cutoff p<0.05.

Ingenuity Pathway Analysis

The list of differentially expressed genes between TAM phenotypes was uploaded into Ingenuity Pathway Analysis software from Qiagen. For IPA, 35 molecules for network and 25 networks per analysis were analyzed. Data were compared against all data sources, all species, tissues, cell lines ans mutations. Confidence settings were set to experimentally observed and high based on prediction. Node types included complex, cytokine, disease, enzyme, function, G protein-coupled receptor, group, growth factor, ion channel, kinase, ligand-dependent nuclear receptor, mature microRNA, microRNA, peptidase, phosphatase, transcription regulator, translation regulator, transmembrane receptor, transporter and others. Potential transcriptional regulators are investigated by computation of the activation z-score and overlap p-value. The overlap p-value compares the significant overlap between known target genes regulated by the potential transcriptional regulator and the genes included in the experimental dataset, while the activation z-score predicts the potential activation state of transcriptional regulators by comparing the experimental dataset with a model assigning random regulation directions (activating or inhibiting). The overlap p-value is calculated by Fisher's Exact Test (p≤0.01). Reddish nodes indicate an increased measurement, while greenish nodes indicate a decreased measurement in the dataset in comparison

to the reference datasets. Orange nodes represent predicted activation and blue nodes represent predicted inhibition of respective proteins. Edges show predicted relationships between two nodes. Orange edges: activation, blue edges: inhibition, yellow edges: findings inconsistent with state of downstream molecule.

MEK Inhibitor Treatment

Administration of Trametinib *in vivo*

Mice were randomized into control or treatment group and treated once daily with 100 µl Trametinib (0.492 mg/kg) or respective amount of vehicle control DMSO dissolved in PEG200 for 2 days by oral gavage. Mice were sacrificed after 48 h of treatment and tissues were harvested for subsequent experiments.

Compound Printing

To investigate sensitivity of macrophage subsets to different compounds, 96 well plates were printed with gemcitabine, trametinib or DMSO serving as control. Printing schemes were designed using Tecan D300e Control software. Gemcitabine was printed at a range from 0.1 nM-10 µM, whereas trametinib was either printed at a range of 1.3 nM-10 µM when using murine macrophages or at a range of 0.1 nM-1 µM when using human macrophages. When using murine tumor cells, trametinib was printed at a range of 1.3 nM- 10 µM. All compounds were printed using Tecan Plate printer D300e. DMSO control was set as first priority at each plate printing. After printing, plates were sealed with parafilm and immediately stored at -80 °C.

Cell Viability Assay – CellTiter-Glo®

First, compound printed plates were brought to RT for 30 min in the dark prior to cell seeding. Cultivated tumor cells were trypsinized, counted and seeded onto compound printed plates according to previously optimized cell numbers and incubated for 72 h at 37 °C. When macrophages were seeded, cells were polarized to respective subsets as described and counted. After cell number determination, macrophage subsets were seeded onto compound printed plates according to previously optimzed cell numbers and incubated for 72 h at 37 °C. For investigation of reversibility of MEK inhibitor sensitivity, macrophages were polarized with TCM from epithelial or mesenchymal tumor cells and analyzed by CellTiter-Glo assay. Following, polarized cells from the same mice were incubated for 48 h with the adversative medium from epithelial or mesenchymal tumor cell lines and afterwards analyzed by CellTiter-Glo Luminescent Cell Viability assay. Therefore, 100 µl of 1:4 diluted

CellTiter-Glo® solution was brought to RT in dark and was automatically pipetted into each well using Multidrop combi machine. The plate was shaked for 2 min and incubated for 10 min at RT in the dark before measuring luminescence by Tecan Spark 10M. Measured luminescence values from compound treated cells were normalized to respective DMSO control treated cells. Normalized data were log-transformed and non-linear regression was applied on log-transformed data for curve fit.

Cell Cytotoxicity Assay – Propidium Iodide Staining

For investigation of cell cytotoxicity upon treatment, cells were subjected to flow cytometric analysis after propidium iodide (PI) staining. Macrophages were seeded onto 6 well plates and polarized as described above. Following polarization, cells were incubated with fresh medium containing 17 nM, 60 nM, 2.79 µM trametinib, 0.1% DMSO or left untreated as control for 72 h at 37 °C. After incubation, floating and adherent cells were collected. After collection, cells were centrifuged at RT for 5 min at 1400 rpm and the cell pellet was washed once with 4 ml PBS. Following another centrifugation, the pellet was resuspended in 50 µl PI solution (1 mg/ml) and incubated for 15 min in the dark. Prior to flow cytometric analysis, 100 µl PBS were added to the tube. Samples were measured immediately after PI staining. Gates were set according to untreated samples and relative number of dead cells from trametinib treated samples was normalized to DMSO treated samples.

Metabolic Extracellular Flux Analysis

MitoStress Test of Murine Macrophages

Macrophage oxidation phosphorylation (OXPHOS) was investigated by measuring oxygen consumption rate (OCR) using Seahorse XFe96 Analyzer with Seahorse XF Cell Mito Stress Test Kit following manufacturer's instructions. Bone marrow-derived murine macrophages were polarized with respective media as previously described and seeded on XF-96 cell culture plate and allowed to attach overnight. Furthermore, sensor cartridge was incubated overnight in 200 µl calibration solution at 37 °C. After overnight attachment, medium was aspirated carefully and cells were washed 3x with 140 µl MitoStress assay medium. Cells were incubated for 45 min at 37 °C in MitoStress assay medium. Afterwards, the cell plate was placed into the XFe96 Analyzer and cells were treated sequentially with 2 µM Oligomycin, 1.5 µM FCCP as well as 0.5 µM Rotenone/Antimycin A and subsequent changes in OCR were used to calculate OXPHOS characteristics. Oligomycin inhibits ATP synthase, which leads to a reduction of OCR levels after injection to the cells, while FCCP is an uncoupling agent that disrupts mitochondrial membrane potential, resulting in an uncontrolled flow of electrons through the electron transport chain leading to an OCR maximum. Furthermore, Rotenon/AntimycinA inhibit complex I and complex III, which shuts down mitochondrial respiration

enabling monitoring of non-mitochondrial respiration. Following OCR measurements, cells were fixed in 4% PFA for 10 min at RT and stained with 100 µl DAPI dilution (1:2000) for normalization according to respective cell numbers. DAPI intensity was measured using Tecan Spark10M. Normalization and data analysis was performed using Seahorse Wave Desktop 2.6 software.

For investigation of MEKi-induced subset-specific metabolic changes, macrophages were seeded overnight in XF-96 cell culture plate and treated with 10 nM trametinib or respective volume of DMSO for 30 h and then analyzed immediately by Seahorse XF Cell Mito Stress Test Kit following manufacturer's instructions and as previously described. For very experiment, wells which showed evidence of failed inhibitor injections were excluded from the analysis.

GlycoStress Test of Murine Macrophages

Macrophage glycolytic rate was investigated by measuring the extracellular acidification rate (ECAR) using Seahorse XFe96 Analyzer with Seahorse XF Cell Glyco Stress Test Kit following manufacturer's instructions. Bone marrow-derived murine macrophages were polarized with respective media as previously described and seeded on XF-96 cell culture plate and allowed to attach overnight. Furthermore, sensor cartridge was incubated overnight in 200 µl calibration solution at 37 °C. After overnight attachment, medium was aspirated carefully and cells were washed 3x with 140 µl GlycoStress assay medium. Cells were incubated for 45 min at 37 °C in GlycoStress assay medium. Afterwards, the cell plate was placed into the XFe96 Analyzer and cells were treated sequentially with 10 mM Glucose, 1 µM Oligomycin and 50 mM 2-Deoxyglucose and subsequent changes in ECAR were used to calculate glycolytic rate characteristics. While glucose injection fuels glycolysis of the cells, Oligomycin inhibits ATP synthase, resulting in an increased dependence on glycolysis. In comparison, 2-Deoxyglucose is a competitive inhibitor of glucose, which shuts down glycolytic rate. Following ECAR measurements, cells were fixed in 4% PFA for 10 min at RT and stained with 100 µl DAPI dilution (1:2000) for normalization according to respective cell numbers. DAPI intensity was measured using Tecan Spark10M. Normalization and data analysis was performed using Seahorse Wave Desktop 2.6 software. For very experiment, wells which showed evidence of failed inhibitor injections were excluded from the analysis.

Glucose concentration measurement

Measurement of glucose concentration from cell culture supernatants was conducted by the central laboratory of university hospital Essen. For the analysis, 500 µl of fresh, unconditioned medium (medium), tumor conditioned medium (TCM) incubated for 72 h with tumor cells and tumor conditioned medium incubated for 6 h, 24 h and 48 h with tumor conditioned macrophages (TAMCM) were analyzed. Results were provided as glucose concentration in mg/dl.

Protein Related Techniques

Protein Extraction

For protein extraction, cell plates were put on ice and rinsed once with ice-cold PBS. Cells were scraped in ice-cold PBS containing 1x Phosphatase inhibitor and 1x Protease inhibitor and cells were centrifuged at 4 °C for 5 min at 400xg. The resulting pellet was resuspended in lysis buffer (200 µl lysis buffer per 10 cm dish) and incubated for 10 min on ice. Afterwards, cells were centrifuged at 4 °C for 30 min at 12000 rpm and supernatant was transferred into a new tube. Protein concentration was measured with BCA assay following manufacturer's instructions. After determination of protein concentration, samples were stored on -20 °C until experimental usage.

SDS-PAGE

Sodiumdodecylsulfat polyacrylamide gel electrophoresis (SDS-PAGE) is a method to separate proteins based on their molecular weight by application of a voltage field. Isolated proteins are denaturated by heat and denaturating agents, e.g. DTT or β-mercaptoethanol, which dissolve disulfide bonds. Denaturated proteins are masked by negatively charged SDS, allowing for separation of proteins proportional to its molecular weight, where proteins with a higher molecular weight are more restrained than smaller proteins inside the gel. Prior to loading samples onto the gel, samples were mixed with 6x loading buffer containing β-mercaptoethanol and heated for 10 min at 95 °C. After sample preparation, SDS-PAGE gels were produced according to the following tables.

Table 2.15: SDS-PAGE separation gel composition

Separation gel (10 ml)	6%	8%	10%
Aqua dest.	5.3	4.6	4
30% Acrylamid mix	2	2.7	3.3
Tris (1 M, pH 8.8)	2.5	2.5	2.5
SDS (10% Solution)	0.1	0.1	0.1
APS (10% Solution)	0.1	0.1	0.1
TEMED	0.01	0.01	0.01

Table 2.16: SDS-PAGE stacking gel composition

Stacking gel 5% (5 ml)	
Aqua dest.	3.6
30% Acrylamid mix	0.67
Tris (1 M, pH 6.8)	0.625
SDS (10% Solution)	0.05
APS	0.05
TEMED	0.005

After SDS gel preparation, gels were clamped into clamping frames and placed into BioRad electrophoresis chambers. The chambers were filled with 1x running buffer and samples as well as PageRuler PreStained Protein Ladder were loaded into respective gel slots. SDS-PAGE was started by applying 95 V for 10 min, followed by 130 V until proteins were close to running out of the gel.

Western Blot

Separated proteins from SDS-PAGE were transferred to a nitrocellulose membrane using BioRad TransBlot Turbo Transfer System. Filter paper were pre-wetted with cold 1x transfer buffer and filter paper, membrane and gel were placed onto each other in the TransBlot Turbo chamber. The blotting chamber was closed, placed into the TransBlot Turbo device and appropriate program was selected to transfer separated proteins from the gel onto the nitrocellulose membrane within 7 min. Following transfer, the membrane was blocked for 1 h at RT in 5% BSA/TBS-T and incubated with primary antibody overnight at 4 °C in 5% BSA/TBS-T (Table 2.7). After incubation, the membrane was washed 3 times for 5 min each with 1x TBS-T and incubated with secondary antibody diluted 1:30000 in 5% BSA/TBS-T for 1 h at RT (Table 2.8). The membrane was washed 3 times for 5 min each with 1x TBS-T and then developed with ECL substrate according to manufacturer's protocol. Imaging was performed with BioRad ChemiDoc™ MP Imaging System with optimal autoexposure settings.

Enzyme-Linked Immunosorbent Assay

Enzyme-linked immunosorbent assay (ELISA) was used for detection of murine interferonγ (IFNγ) according to manufacturer's instructions. All reagents and samples were brought to RT and assay diluents were prepared according to manufacturer's protocol. 100 µl of IFNγ standard (2.74 pg/ml – 2 ng/ml) and samples were added into anti-IFNγ antibody-coated wells. Wells were covered with foil and incubated for 2.5 h at RT with gentle shaking. Solution was discarded and wells were washed 4 times. After washing, 100 µl of biotinylated detection antibody was added to each well and incubated for 1 h at RT with gentle shaking. Following incubation, wells were washed 4 times and afterwards incubated with 100 µl streptavidin solution for 45 min at RT with gentle shaking. The wells were washed 4 times and 100 µl TMB One-Step Substrate Reagent was added to each well. Following 30 min incubation at RT in the dark with gentle shaking, 50 µl of Stop solution was added to each well and absorption was measured at 450 nm immediately using Tecan Spark 10M.

Statistical Data Analysis

Statistics were calculated using GraphPad Prism 8. Data were analyzed with non-parametric Kruskal-Wallis test with Dunn's test for correction for multiple comparisons using statistical hypothesis testing and with two-tailed non-parametric Mann-Whitney test. Correlation analysis was performed by calculation of Spearman`s rank correlation. p values below 0.05 were considered as statistically significant.

Results

Effect of MEKi on M2-like Macrophages in Murine PDAC

Long-Term MEKi Treatment Decreased M2-like Macrophages *in vivo*

To investigate the effects of MEK inhibition (MEKi) in established PDAC *in vivo*, transcriptomes from DMSO- and MEKi-treated tumors from genetically engineered mouse model of spontaneous PDAC, *CKP*, were analyzed by microarray. Gene set enrichment analysis (GSEA) was performed to identify enriched gene sets in respective biological phenotypes. The *CKP* mouse model recapitulates human PDAC in a multitude of different characteristics, e.g. tumor aggressiveness, heavy stroma and a highly immunosuppressive tumor microenvironment (Cheung et al. 2018). GSEA revealed an enriched gene set of anti-inflammatory M2-like macrophage in DMSO-treated tumors (Fig. 3.1A), while MEKi-treated tumors showed a downregulation of a M2-like macrophage-associated gene set (Fig. 3.1B).

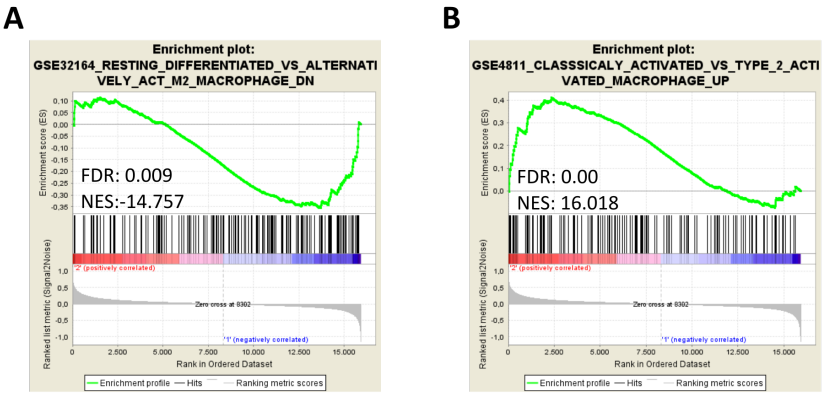

Figure 3.1: Long-term MEKi treatment decreased M2 macrophages *in vivo*. GSEA of DMSO- and MEKi-treated tumors identified differentially enriched gene sets between phenotypes. A: GSEA of DMSO-treated murine bulk tumor tissue based on microarray data ($p<0.05$, FDR<0.25). B: GSEA of MEKi-treated murine bulk tumor tissue based on microarray data ($p<0.05$, FDR<0.25) (n= 6 mice/ group).

Short-Term MEKi Treatment Decreased Anti-Inflammatory Marker Protein Expression *in vivo*

To validate the downregulation of M2-like macrophage-associated gene expression on the protein level, mice were treated for 2 days (short-term) or 2-8 weeks (long-term) with MEKi to investigate immediate and sustained effects of MEK inhibition. (Fig. 3.2)

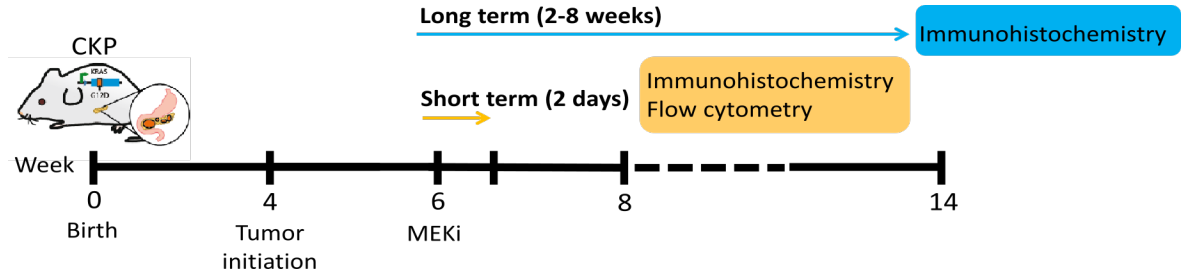

Figure 3.1: Schematic MEK inhibitor treatment schedule. *CKP* mice were enrolled into study at 6 weeks of age, when established tumors were observed. Mice were treated once daily with DMSO or the MEKi (trametinib) by oral gavage for 2 days (short-term) or 2-8 weeks (long-term) to investigate immediate and sustained treatment effects of MEK inhibition. After sacrification, tumors were isolated and analyzed at the transcriptional and protein level.

After sacrification, M2-like macrophage-associated protein expression was assessed in treated *CKP* tumors by immunohistochemistry (IHC) and quantified (Fig. 3.3 A-B). The quantification revealed 30-40% CD11b$^+$ myeloid cells in untreated and DMSO-treated control tumors. After short-term MEKi treatment, the amount of CD11b$^+$ cells decreased dramatically to 5%, but was restored after long-term treatment to 30%. In accordance with this observation, F4/80$^+$ macrophages contributed to 25-30% of whole tumor bulk cells in control tumors, while strongly decreased to 5% after short-term MEKi treatment. Unlike CD11b$^+$ cells, F4/80$^+$ cells did not increase after long-term MEKi treatment, but remained decreased at 5%. The anti-inflammatory marker protein CD206 was expressed on 25-30% of cells in control tumors, while its expression was decreased after short-term MEKi treatment to below 5% and partially restored after long-term MEKi to 15%. The same trend was observed for anti-inflammatory marker protein CD163, which was expressed on 7-10% of bulk tumor cells and decreased after MEKi treatment to approximately 3%. The pro-inflammatory marker protein NOS2 was expressed in 2-4% of cells in control tumors and remained unchanged after short-term MEKi, while it was almost absent in long-term MEKi-treated tumors.

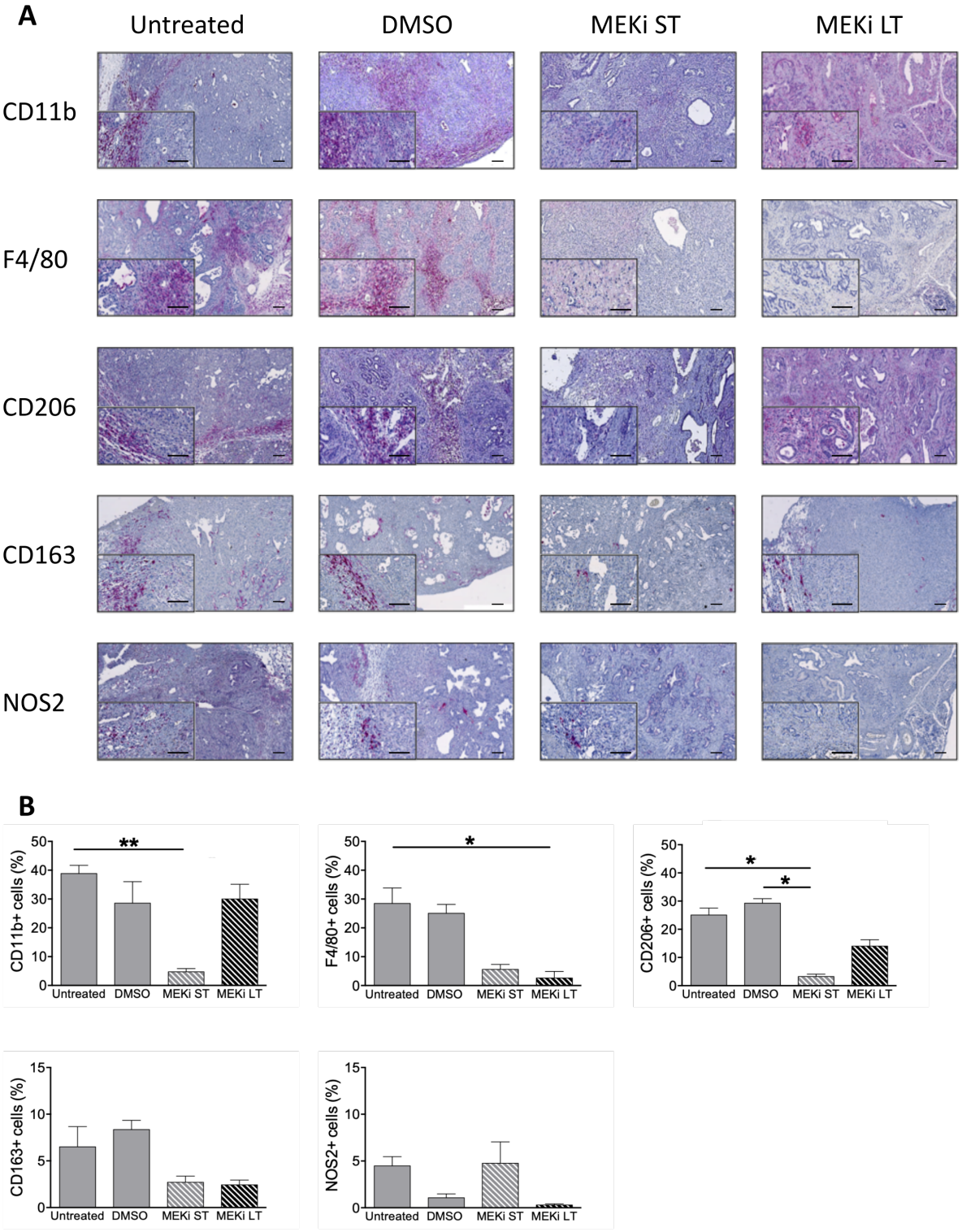

Figure 3.3: Short-term MEKi treatment decreased macrophages and anti-inflammatory marker expression in *CKP* model *in vivo*. A: Representative immunohistochemical stainings of untreated, DMSO, short and long-term MEKi-treated pancreatic tumors for CD11b, F4/80, CD206, CD163 and NOS2 protein from *CKP* mice (n=3-6 mice/group). Magnification: 25x, 100x. Scale bars represent 100 µm. B: Quantification of marker protein positive cells. Bar charts show the percentage of marker protein positive cells as the average of 5 fields from each murine PDAC tumor (10x objective magnification). Mean + SD is shown (Kruskal-Wallis test with Dunn's Post test; *p < 0.05, ** p < 0.01; n=3-6 mice/group). ST: short-term treated, LT: long-term treated.

Flow Cytometric Analysis of M2-like Macrophage Depletion *in vivo*

To validate the IHC results, macrophage abundance in tumor bulks, as well as their expression level of pro- and anti-inflammatory markers, was analyzed by flow cytometry (Fig. 3.4A). Macrophage content was approximately 35% in untreated and DMSO-treated control tumors, but it decreased to 10% after short-term MEKi treatment (Fig. 3.4B). Furthermore, over 90% of macrophages in control tumors expressed CD206 and CD80, whereas CD301 was expressed by approximately 15% of macrophages (Fig. 3.4C-E). After short-term MEKi, the amount of $CD206^+$ macrophages decreased to 60%, while the amount of $CD80^+$ macrophages was reduced slightly to 80%. In contrast, the amount of $CD301^+$ macrophages after MEKi treatment increased to 50%. The pro-inflammatory marker NOS2 was not detectable under all treatment conditions (Fig. 3.4F). In addition to the proportion of the positive population, the expression level of respective markers within the marker positive macrophage populations were analyzed and compared. While CD80 expression level remained constant after MEKi within the positive macrophage population, the expression level of CD206 in $CD206^+$ macrophages was decreased by 50% (Fig. 3.4G-H). In contrast, CD301 expression was increased by 3-fold in $CD301^+$ macrophages after MEKi treatment. (Fig. 3.4I).

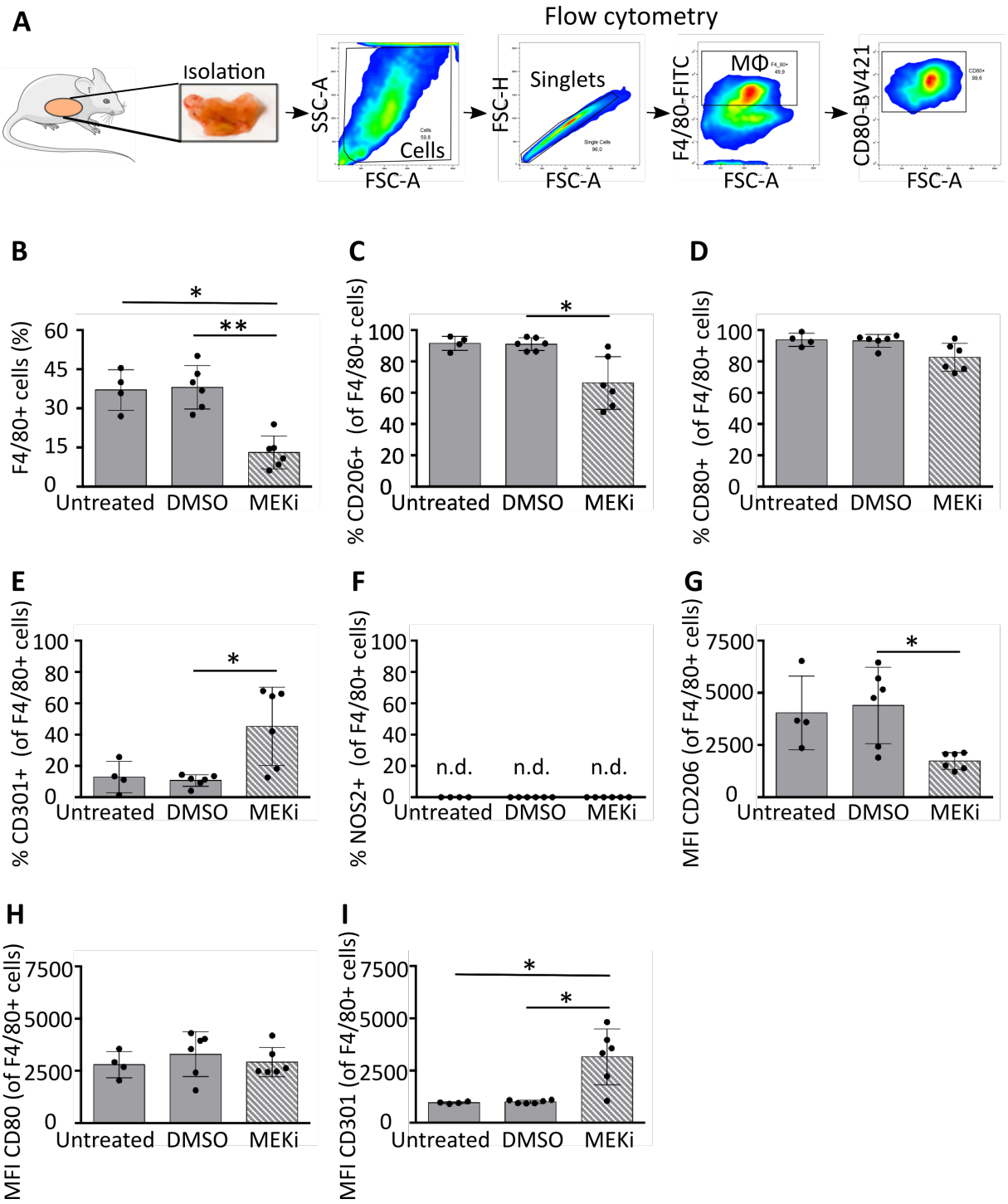

Figure 3.4: MEKi treatment induced M2-like macrophage depletion from PDAC tumors in *CKP* mice. A: Schematic gating strategy for isolated pancreatic bulk tumors. After 48 h of respective treatment and tumor isolation, bulk tumor cells were digested into single cell suspension and analyzed by flow cytometry. Debris and doublets were excluded from gating and macrophages were assessed as F4/80+ cells. Subsequent marker protein expression was assessed based on F4/80+ cell population. B: Quantification of percentage of F4/80+ cells from bulk tumor from untreated, DMSO- or short-term MEKi-treated *CKP* mice by flow cytometry. C-F: Quantification of percentage of (C) CD206+, (D) CD80+, (E) CD301+ and (F) NOS2+ cells within the F4/80+ macrophage population from untreated, DMSO- or short-term MEKi-treated *CKP* mice. G-I: Protein expression level estimation by determination of the mean fluorescence intensity (MFI) of (G) CD206, (H) CD80 and (I) CD301 in the F4/80+ cell population. Filled bars: Untreated and DMSO-treated mice, striped bars: MEKi-treated mice, n.d.: not detectable (Kruskal-Wallis test with Dunn's Post test; *p < 0.05, ** p < 0.01; n=4-6 mice/group).

Macrophage infiltration might change according to tumor stage or size. In order to clarify the influence of tumor size on macrophage abundance, tumor weight was determined and macrophage content was examined by flow cytometry. Importantly, no correlation between tumor weight and macrophage abundance was observed, since tumors of different weight showed similar relative abundance of macrophage contents (Fig. 3.5A-B).

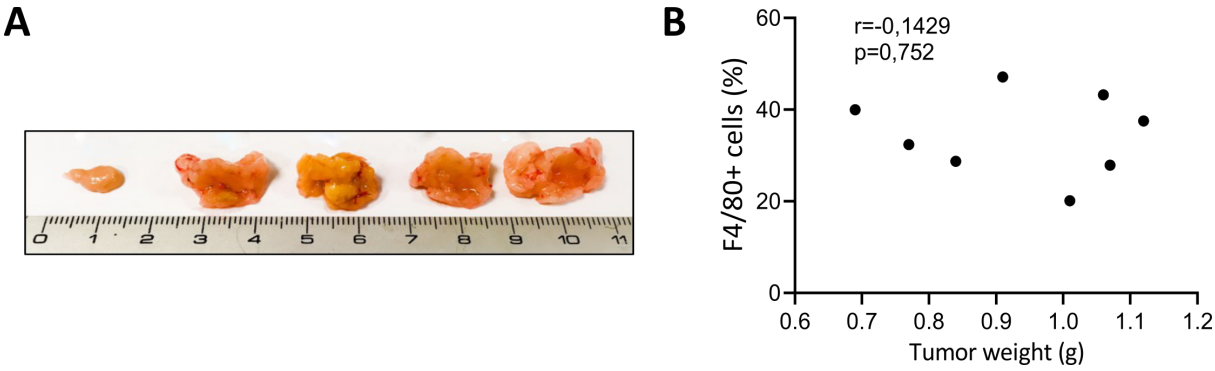

Figure 3.5: Relative macrophage content is not correlated with tumor size. A: Representative PDAC tumors from *CKP* mice of different age, ranging from 6 weeks (left) to app. 9 weeks (right). B: Relative macrophage content from murine PDAC tumors of different tumor weight. After tumor weighing, the percentage of F4/80+ macrophages within bulk tumor tissue was analyzed by flow cytometry. Percentage of F4/80+ cells was correlated to tumor weight by Spearman's correlation (n=8).

Taken together, these *in vivo* data indicated that anti-inflammatory M2-like macrophages were depleted after short- and long-term MEKi treatment of murine PDAC tumors and that the remaining macrophage population showed a reduced expression of anti-inflammatory marker protein CD206. Since the effect of MEKi on M2-like macrophages was present as early as 2 days after treatment initiation, we intended to examine the underlying molecular mechanisms through analyzing the effect of MEK inhibition on macrophages *in vitro*.

Characterization of *in vitro* Polarized Macrophages

Polarized Macrophages Showed Subset-Specific Gene Expression

Prior to investigating the effects of MEK inhibition on different macrophages subsets, macrophage subset generation had to be established *in vitro*. Therefore, murine macrophages were induced from bone marrow-derived precursor cells, following differentiation for 5 days in macrophage colony-stimulating factor (M-CSF) containing medium. After differentiation, cells were polarized to pro-inflammatory M1-like macrophages or anti-inflammatory M2-like macrophages (Fig. 3.6).

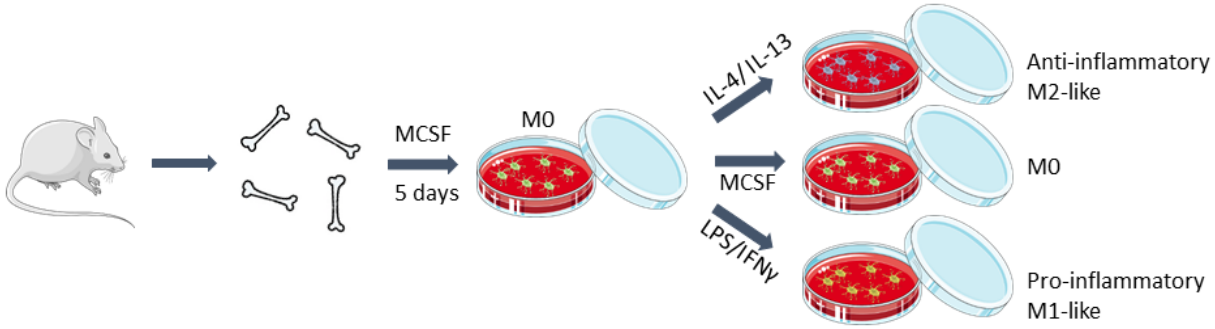

Figure 3.6: Schematic experimental setup for macrophage isolation, differentiation and polarization. Bone marrow-derived progenitor cells were isolated from *femur* and *tibia* of C57BL/6 mice and differentiated *in vitro* into macrophages by incubation for 5 days in M-CSF containing medium. Following, M-CSF containing medium was removed and replaced by medium containing IL-4 and IL-13 for M2-like macrophage polarization, IFNγ and LPS for M1-like macrophage polarization or cells were placed into M-CSF containing medium for staying in the "M0" state.

The polarization was validated by RNAseq and subsequent analysis. Hierarchical clustering separated macrophages based on their polarization state with M0 macrophages being closer related to anti-inflammatory M2-like macrophages than to pro-inflammatory M1-like macrophages (Fig. 3.7A). Furthermore, the different macrophage subsets showed uniquely expressed genes with M1-like macrophages showing expression of pro-inflammatory genes e.g. *Nos2* and *Tnf,* while M2-like macrophages showed expression of well-known anti-inflammatory genes e.g. *Irf4* with pro-inflammatory genes e.g. *Stat1* and *Il1b* being downregulated concomitantly (Fig. 3.7B). Additionally, GSEA revealed M1-like macrophages were enriched for gene sets associated with interferon gamma (IFNγ) response, tumor necrosis factor α (TNFα) signaling, as well as antigen processing/presentation and glycolysis when compared against M0 and M2-like macrophages. In contrast, M2-like macrophages were enriched for gene sets involved in fatty acid metabolism and oxidative phosphorylation (Fig. 3.7C-D).

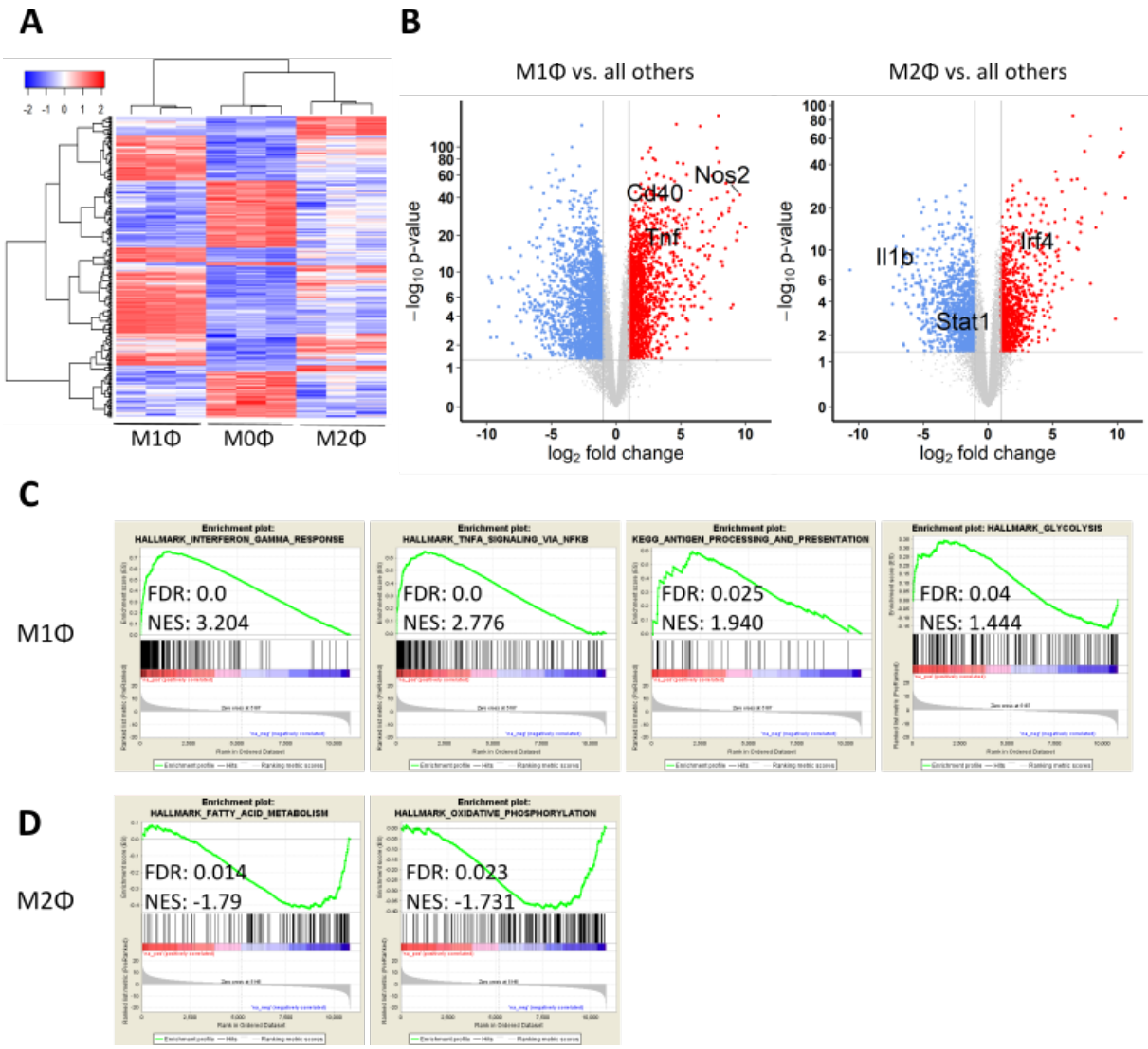

Figure 3.7: M1-like macrophages expressed pro-inflammatory genes, while M2-like macrophages were characterized by anti-inflammatory gene expression. A: Heatmap based on metagenes of M0, M1-like and M2-like polarized murine macrophages. Highly expressed genes are indicated by red and underrepresented genes by blue. Heatmap displays the expression changes between the different macrophage subsets based on the row-wise z-score ($p \leq 0.05$, $-2 \leq \log_2 FC \geq 2$; n=3). B: Volcano plots showing fold changes for genes differentially expressed between M1-like vs. M0/ M2-like macrophages (left) or M2-like vs. M0/M1-like (right), respectively. Highly expressed genes are indicated by red and underrepresented genes by blue. ($p<0.05$, $-2 \leq \log_2 FC \geq 2$; n=3). C-D: GSEA identified gene sets specific for (C) M1-like and (D) M2-like polarized macrophages ($p<0.05$, FDR<0.25; n=3).

Furthermore, polarized macrophages were characterized by gene expression analysis of classical M1-like and M2-like macrophage marker genes using qRT-PCR. Gene expression analysis of M0 macrophages showed a stronger expression of anti-inflammatory genes, e.g. *Cd206* and *Cd301*, which was reflected by lower ΔC_t values in comparison to pro-inflammatory genes, e.g. *Il-12 p35* and *Il-6*, in qRT-PCR (Fig. 3.8A). In M1-like macrophages, pro-inflammatory genes were highly upregulated in comparison to M0 macrophages, with *Nos2* being upregulated 10^5 fold after stimulation, whereas some anti-inflammatory genes e.g. *Cd206* and *Cd301* were downregulated (Fig. 3.8B). In M2-like macrophages, pro-inflammatory genes were only slightly upregulated after stimulation in

comparison to M0 macrophages, whereas the magnitude of upregulation was higher for anti-inflammatory genes, e.g. *Arg1* (Fig. 3.8C).

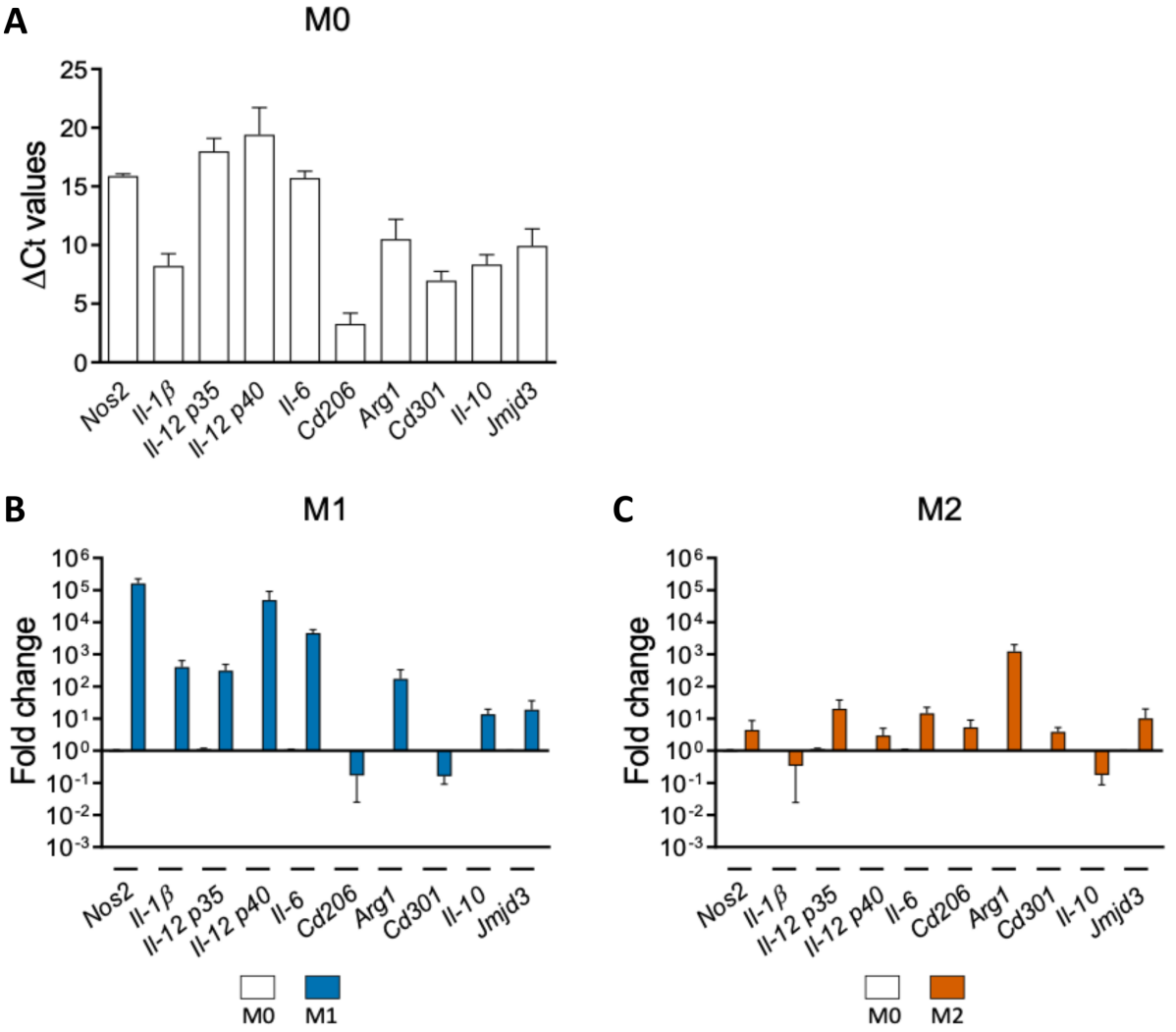

Figure 3.8: Polarized macrophages displayed M1-like and M2-like macrophage specific mRNA expression of immune markers. A: Gene expression analysis of immune-related genes by quantitative real-time PCR. mRNA expression in M0 macrophages was analyzed by calculation of ΔC_t where Cyclophilin A served as reference control for normalization. B-C: Gene expression fold changes of immune-related genes in M1-like and M2-like macrophages after polarization in comparison to M0 macrophages. Fold change expression of M1-like and M2-like macrophages were normalized to M0 macrophages. Fold changes were compared between (B) M1 and M0 and (C) M2 and M0 macrophages for each gene. White: M0, blue: M1, red: M2. (Mann-Whitney test; n=3).

Marker Protein Expression of Polarized Macrophages

To confirm *in vitro* macrophage polarization on the protein level, polarized macrophage subsets were analyzed by flow cytometry for the expression of M1-like and M2-like specific marker proteins. M1-like macrophages showed high expression of pro-inflammatory protein NOS2, while M0 macrophages and M2-like macrophages showed almost no expression (Fig. 3.9A). Additionally, M1-like macrophages highly expressed pro-inflammatory CD80, while its expression was reduced in M0 and M2-like macrophages (Fig. 3.9B). In contrast, M2-like macrophages showed the highest

expression of anti-inflammatory markers CD206 and CD301, which were only weakly expressed in M0 and M1-like macrophages (Fig. 3.9C-D).

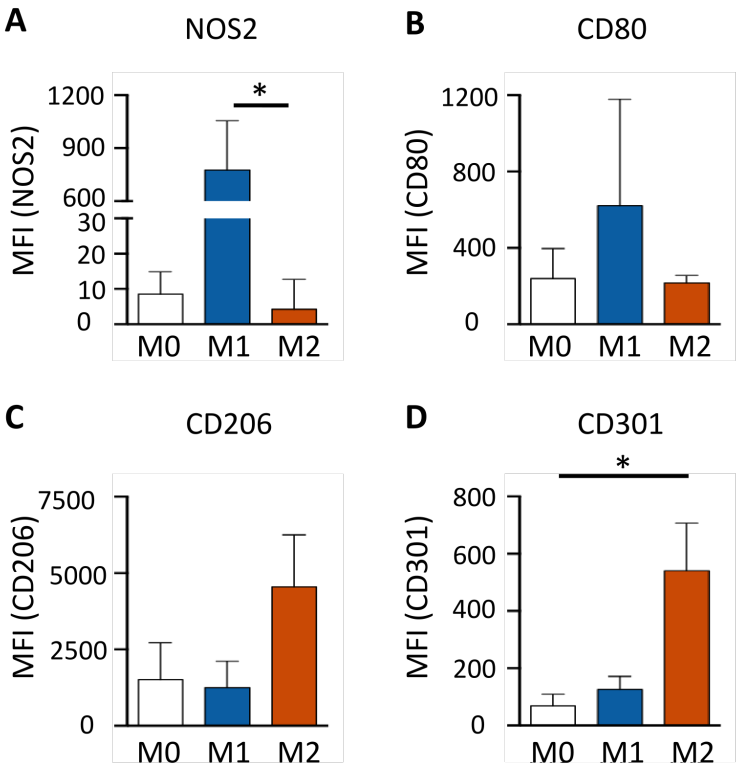

Figure 3.9: Polarized macrophages showed M1-like and M2-like macrophage specific protein expression. A-D: Protein expression level of pro-inflammatory marker proteins (A) NOS2 and (B) CD80 as well as anti-inflammatory marker proteins (C) CD206 and (D) CD301 on murine M0, M1-like and M2-like macrophages was analyzed by flow cytometry. Expression levels are shown as mean fluorescence intensity (MFI). White: M0, blue: M1, red: M2 (Kruskal-Wallis test with Dunn's Post test; *$p < 0.05$; n=3).

Metabolic Characterization of Polarized Macrophages

Macrophage activation states have been shown to be tightly associated with central metabolic pathways. Since GSEA revealed differences in gene sets associated with metabolic pathways between M1-like and M2-like macrophages (Fig. 3.7C-D), we sought to investigate potential metabolic differences following macrophage stimulation by measuring oxygen consumption rate (OCR) for oxidative phosphorylation (OXPHOS) estimation (Fig. 3.10A). M0 macrophages showed a basal oxygen consumption rate of app. 70 pmol/min/RFU with a spare respiratory capacity as well as ATP production of 50 pmol/min/RFU (Fig. 3.10B-C). In contrast, M1-like macrophages showed a decreased basal respiration and no spare respiratory capacity with a reduced ATP production of 20 pmol/min/RFU. Following stimulation, M2-like macrophages revealed an increase in basal respiration of app. 130 pmol/min/RFU as well as an increase in spare respiratory capacity to 120 pmol/min/RFU

(Fig. 3.10B). Additionally, ATP production was increased to 110 pmol/min/RFU in M2-like macrophages (Fig. 3.10C).

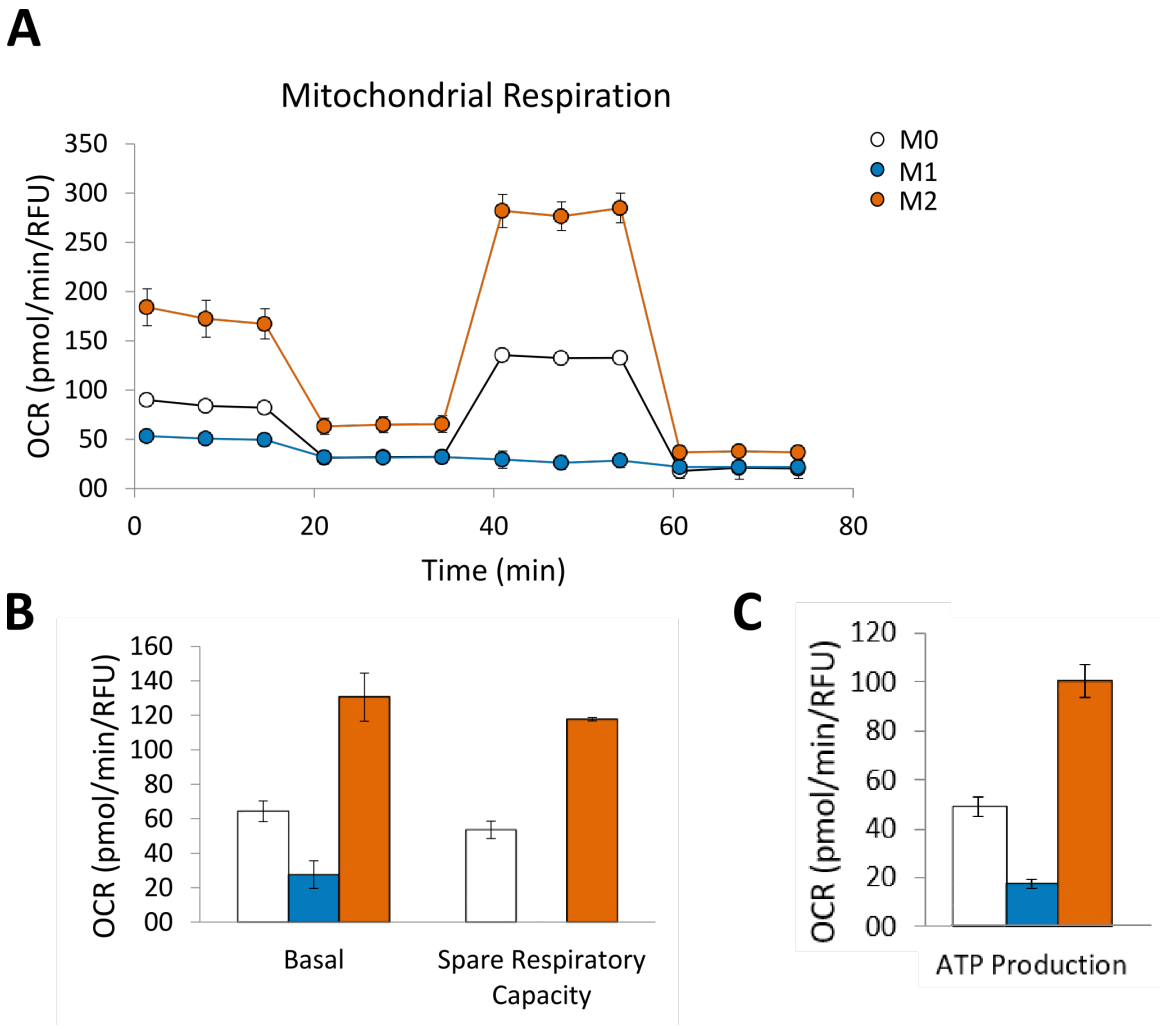

Figure 3.10: Anti-inflammatory M2-like macrophages showed increased mitochondrial respiration. A: Representative experiment showing mitochondrial respiration reflected by oxygen consumption rate (OCR) levels. OCR was detected in murine M0, M1-like and M2-like macrophages under basal conditions followed by addition of oligomycin (2 µM), the uncoupler FCCP (1.5 µM) and the electron transport inhibitor Rotenone/AntimycinA (0.5 µM). B: Determination of basal respiration and spare respiratory capacity by OCR measurement. C: Determination of ATP production by OCR measurement. Cells were fixed and stained with DAPI and values were normalized according to respective cell numbers. White: M0, blue: M1, red: M2 (n=2).

To further focus on metabolic adaptation following macrophage polarization, extracellular acidification rate (ECAR) was measured to estimate glycolytic capacity of polarized cells (Fig. 3.11). M0 macrophages showed a basal ECAR of app. 40 mpH/min/RFU with a glycolytic capacity of 50 mpH/min/RFU and a glycolytic reserve of 10 mpH/min/RFU (Fig. 3.11A-B). M1-like macrophages revealed an increase in glycolysis and glycolytic capacity with app. 100-130 mpH/min/RFU. Additionally, M1-like macrophages had an increased glycolytic reserve of 40 mpH/min/RFU. In contrast, M2-like macrophages showed strongly reduced glycolysis of app. 5 mpH/min/RFU with reduced glycolytic capacity and no detectable glycolytic reserve.

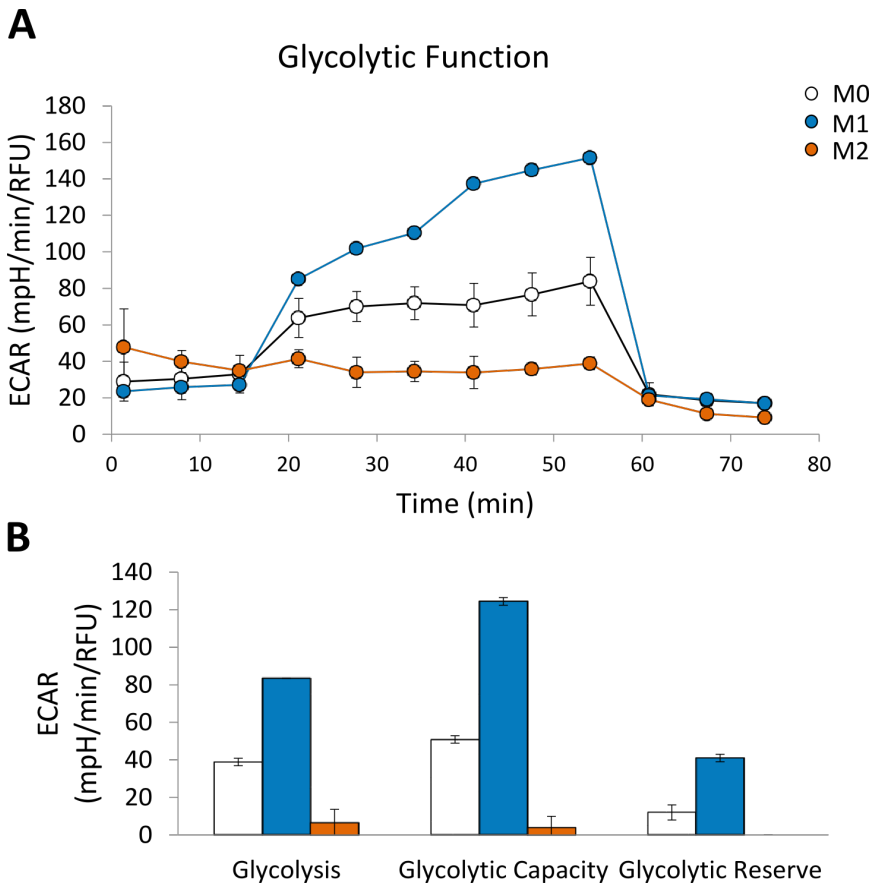

Figure 3.11: Pro-inflammatory M1-like macrophages showed increased glycolysis. A: Representative experiment showing glycolytic function reflected by extracellular acidification rate (ECAR) levels. ECAR was detected in murine M0, M1-like and M2-like macrophages under basal conditions followed by addition of glucose (10 mM), oligomycin (1 µM) and 2-deoxyglucose (50 mM). B: Determination of glycolysis, glycolytic capacity and glycolytic reserve by ECAR measurement. Cells were fixed and stained with DAPI and values were normalized according to respective cell numbers. White: M0, blue: M1, red: M2 (n=2).

Taken together, these data indicated that *in vitro* macrophage polarization affected polarized cells on different levels. While M1-like macrophages showed an increased gene and protein expression of pro-inflammatory markers and were characterized by a glycolytic metabolism, M2-like macrophages were characterized by an increased oxidative phosphorylation and expression of anti-inflammatory genes and proteins.

Effect of MEK Inhibition on *in vitro* Polarized Murine Macrophages

Pro-Inflammatory M1-like Macrophages Showed Low Sensitivity to MEKi-Induced Cell Death

To investigate, whether polarized macrophage subsets showed differences in MEKi sensitivity, cell viability after MEKi treatment was examined by IC_{50} determination and by propidium iodide (PI) staining using flow cytometry. Cell viability analysis showed that M0 macrophages were most

sensitive to MEKi with an IC_{50} of 12 nM, while M2-like macrophages were less sensitive with an IC_{50} of 33.7 nM (Fig. 3.12A). In contrast, pro-inflammatory M1-like macrophages were characterized by a low sensitivity to MEKi-mediated cell death induction, with app. 50-80% of the cells being viable at a MEKi concentration of 10 µM.

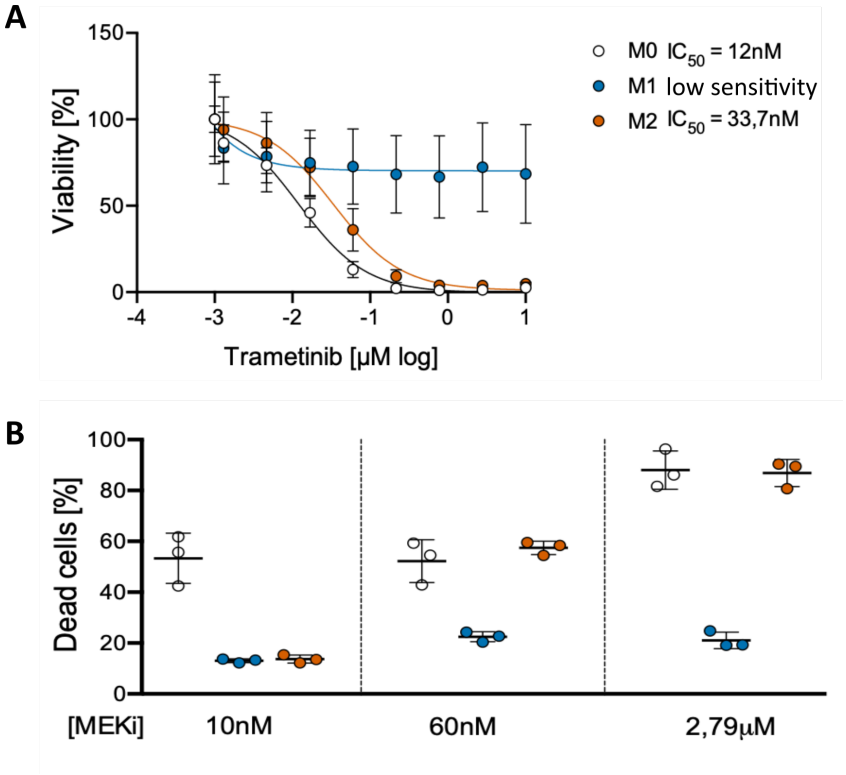

Figure 3.12: Pro-inflammatory M1-like macrophages showed low sensitivity to MEKi-induced cell death. A: Cell viability analysis by IC_{50} determination of murine M0, M1-like and M2-like macrophages. Polarized cells were seeded on pre-printed 96 well plates containing pharmacologically relevant MEKi concentrations (1.3 nM-10 µM) and incubated for 72 h before measuring cell viability by cell titer glo assay (Kruskal-Wallis test with Dunn's Post test of Area Under Curve; n=3). B: MEKi-induced cell death was determined by propidium iodide (PI) staining of dead cells by flow cytometry. Polarized cells were treated with different MEKi concentrations (10 nM, 60 nM and 2.79 µM) and incubated for 72 h before PI staining and subsequent flow cytometric analysis. White: M0, blue: M1, red: M2 (Kruskal-Wallis test with Dunn's Post test; n=3).

The results were further validated by cytotoxicity assay with PI staining using flow cytometry. At 10 nM, MEKi induced cell death in 50% of M0 macrophages, whereas only 15% of M1-like and M2-like macrophages were positive for PI (Fig. 3.12B). At 60 nM, M0 and M2-like macrophages showed approximately 60% of cell death, while only 20% of M1-like macrophages induced cell death. The amount of dead M1-like macrophages remained at 20% at a concentration of 2.79 µM, while over 90% of M0 and M2-like macrophages induced cell death.

Taken together, these data indicated that anti-inflammatory M2-like macrophages were more sensitive to MEKi-induced cell death than pro-inflammatory M1-like macrophages.

MEK Inhibition Affected Immunological Gene Expression

To investigate gene expression changes of murine macrophages following MEKi treatment, polarized macrophages were treated for 48 h with subIC$_{50}$ concentration of the MEKi or DMSO (control) and analyzed by qRT-PCR (Fig. 3.13). Pro-inflammatory genes of M0 macrophages, e.g. *Il-1β*, were weakly influenced by MEKi, except for an upregulation of *Il-12p35*, whereas anti-inflammatory genes *Cd206*, *Arg1* and *Cd301* were downregulated (Fig. 3.13A). In accordance with these results, pro-inflammatory genes of M1-like macrophages were also weakly influenced by MEKi, expect for *Il-12p40* and *Il-6*, which were upregulated (Fig. 3.13B). Additionally, anti-inflammatory genes *CD206, Arg1* and *Il-10* showed a strong downregulation after MEKi. For M2-like macrophages an opposite trend was observed with most of the pro-inflammatory genes, e.g. *Nos2*, being slightly upregulated, while all investigated anti-inflammatory genes showed an upregulation with *Il-10* being to most upregulated gene (Fig. 3.13C).

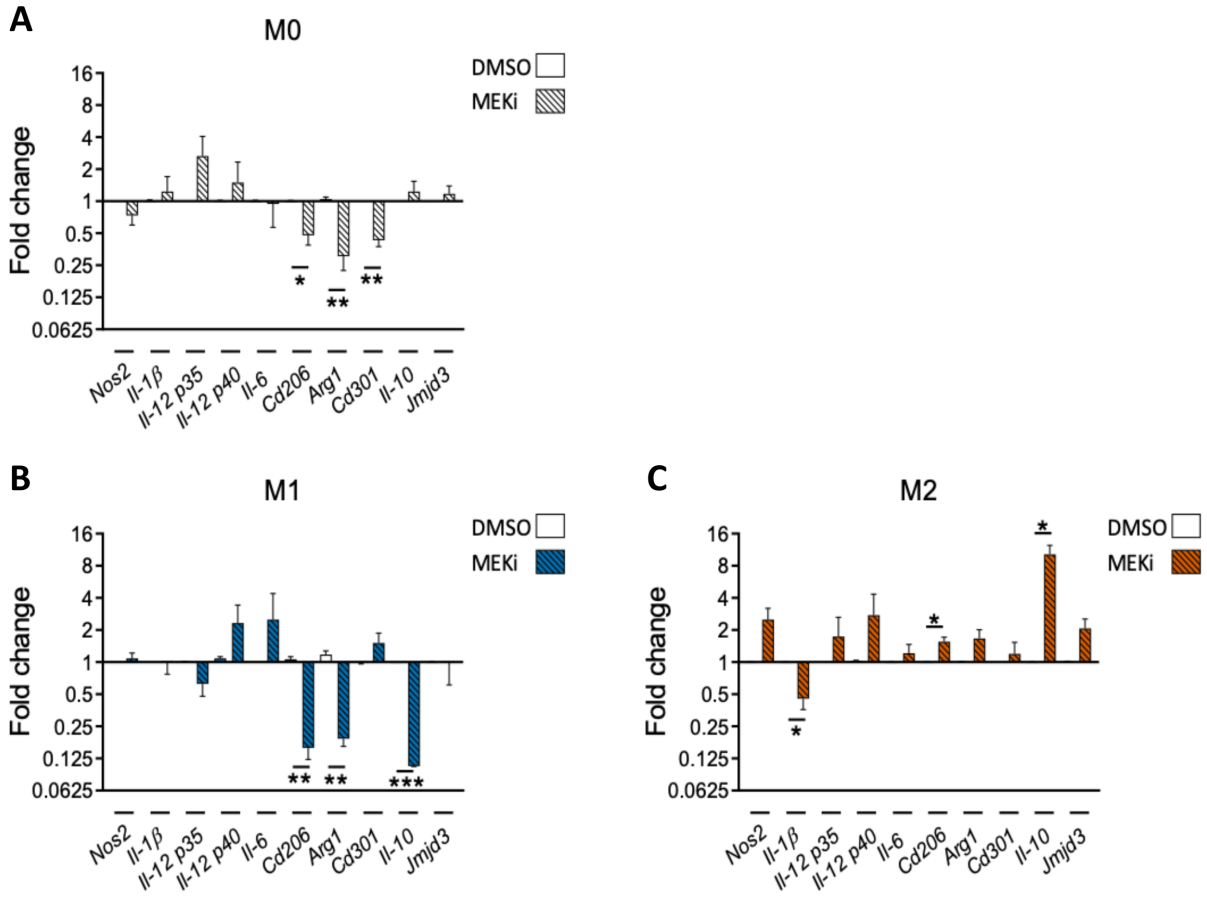

Figure 3.13: Polarized macrophage subsets showed diverse immunological gene expression changes following MEK inhibition. Gene expression fold changes of murine (A) M0, (B) M1-like and (C) M2-like macrophages upon MEKi treatment (10nM) in comparison to DMSO-treated cells. For fold change expression of pro- and anti-inflammatory genes after MEKi treatment, fold changes of MEKi-treated cells were normalized to DMSO-treated control. Fold changes were compared between DMSO- and MEKi-treated cells within each subset for each gene. White: M0, blue: M1, reds: M2, filled bars: DMSO-treated cells, striped bars: MEKi-treated cells (Mann-Whitney test; *p < 0.05, ** p < 0.01, *** p < 0.001; n=3-4).

MEK Inhibition Had Minimal Effect on Marker Protein Expression

To analyze, whether MEKi affected macrophage polarization at the protein level, expression of pro- and anti-inflammatory marker proteins on polarized macrophages upon MEKi and DMSO treatment was examined by flow cytometry. While NOS2 protein level remained almost unchanged in all macrophage subsets, a slight reduction of CD80 protein level was observed in M1-like macrophages after MEKi (Fig. 3.14A-B). Furthermore, CD206 protein level was slightly reduced in M0 macrophages after MEKi, while CD206 protein levels in M1-like and M2-like macrophages remained unchanged (Fig. 3.14C). CD301 protein levels were slightly reduced in M1-like and M2-like macrophages after MEKi, however, CD301 was only weakly expressed in M1-like macrophages (Fig. 3.14D).

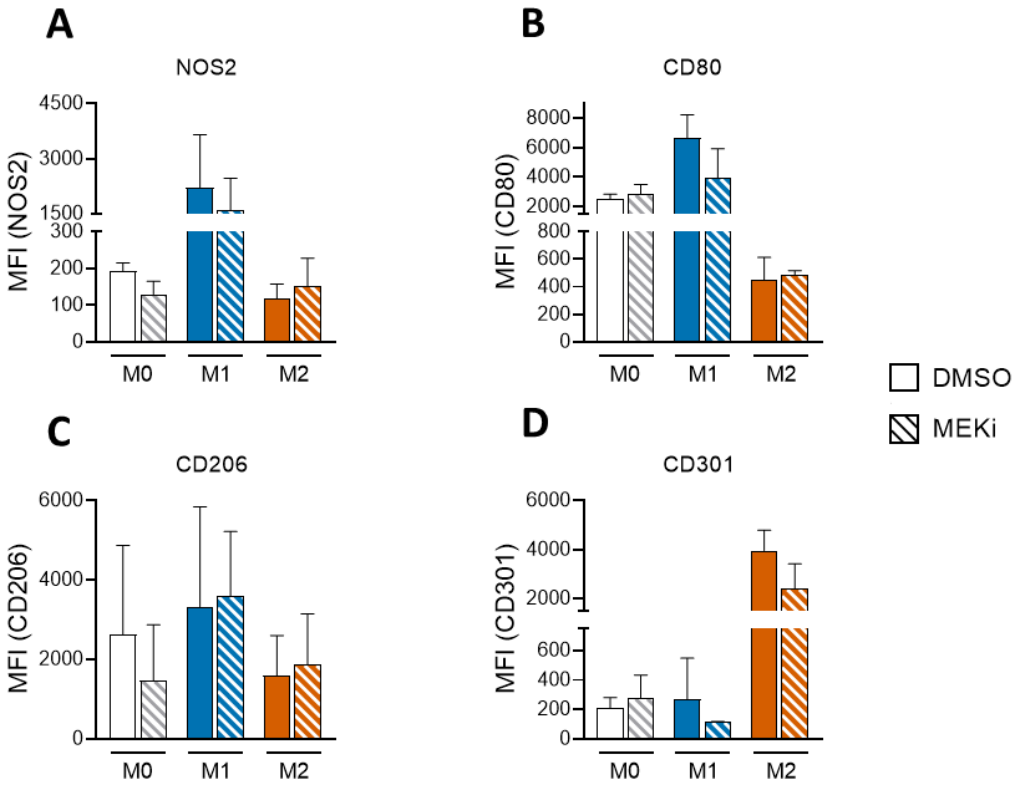

Figure 3.14: MEKi treatment had minimal effect on pro- and anti-inflammatory marker protein expression on polarized macrophages. Polarized murine M0, M1-like and M2-like macrophages were treated with vehicle (DMSO) or MEKi (10 nM) for 48 h and analyzed for protein expression level of pro-inflammatory marker proteins (A) NOS2 and (B) CD80 as well as anti-inflammatory marker proteins (C) CD206 and (D) CD301 by flow cytometry. Protein expression levels are shown as mean fluorescence intensity (MFI) and were compared between DMSO- and MEKi-treated cells within each subset for each protein. White: M0, blue: M1, red: M2, filled bars: DMSO-treated cells, striped bars: MEKi-treated cells (Mann-Whitney test; n=3).

MEK Inhibition Reduced Mitochondrial Respiration in M2-like Macrophages

Cellular metabolism has been linked to activation state of macrophages, thus it was examined, whether MEKi affected oxidative phosphorylation in different polarized macrophage subsets. When inhibiting MEK kinases for 2 h, all macrophage subsets showed no difference in basal respiration, spare respiratory capacity and ATP production, indicating no changes in oxidative phosphorylation rate (Fig. 3.15A-C). When macrophages were incubated for 30 h with the MEKi, M0 macrophages showed no difference in basal respiration, but a slight decrease in spare respiratory capacity and ATP production, whereas M1-like macrophages showed no difference between DMSO- and MEKi-treated cells (Fig. 3.15D-F). However, M2-like macrophages showed a reduced basal respiration as well as a strong decrease in spare respiratory capacity. Furthermore, M2-like macrophages produced less ATP, indicating that MEKi results in a reduction in oxidative phosphorylation specifically in anti-inflammatory M2-like macrophages (Fig. 3.15F).

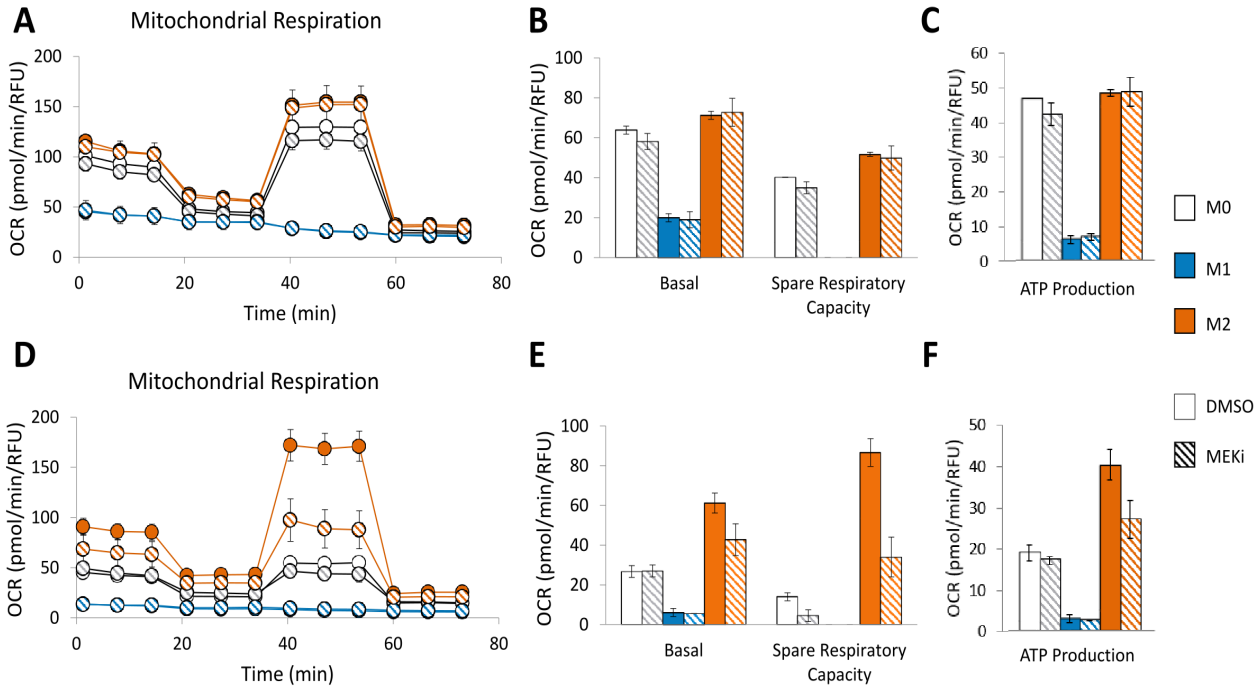

Figure 3.15: MEKi treatment decreased mitochondrial respiration in anti-inflammatory M2-like, but not in M0 and M1-like macrophages. A: Representative experiment showing mitochondrial respiration reflected by oxygen consumption rate (OCR) levels. OCR was detected in murine M0, M1-like and M2-like macrophages, which have been pre-treated for 2 h with vehicle (DMSO) or MEKi (10 nM) under basal conditions followed by addition of oligomycin (2 µM), the uncoupler FCCP (1.5 µM) and the electron transport inhibitor Rotenone/AntimycinA (0.5 µM). B: Determination of basal respiration and spare respiratory capacity by OCR measurement of 2 h vehicle- (DMSO) or MEKi-treated macrophages C: Determination of ATP production by OCR measurement of 2 h vehicle- (DMSO) or MEKi-treated macrophages. D: Representative experiment showing mitochondrial respiration reflected by oxygen consumption rate (OCR) levels. OCR was detected in murine M0, M1-like and M2-like macrophages, which have been pre-treated for 30 h with vehicle (DMSO) or MEKi (10 nM) under basal conditions followed by addition of oligomycin (2 µM), the uncoupler FCCP (1.5 µM) and the electron transport inhibitor Rotenone/AntimycinA (0.5 µM). E: Determination of basal respiration and spare respiratory capacity by OCR measurement of 30 h vehicle- (DMSO) or MEKi-treated macrophages F: Determination of ATP production by OCR measurement of 30 h vehicle- (DMSO) or MEKi-treated macrophages. Cells were fixed and stained with DAPI and values were normalized according to respective cell numbers. White: M0, blue: M1, red: M2, filled bars: DMSO-treated cells, striped bars: MEKi-treated cells (n=2).

Exploration and Characterization of Intratumoral Macrophage Heterogeneity

The *in vitro* generated anti-inflammatory M2-like macrophages showed an increased MEKi sensitivity in comparison to pro-inflammatory M1-like macrophages. However, a growing body of studies has shown that the M1-M2 macrophage dichotomy is likely oversimplified and that macrophages can obtain a plethora of activation states depending on different microenvironmental cues, which are generated by their surrounding tissue e.g. the tumor (Huang et al. 2019).Transcriptomic analysis unraveled the existence of different tumor subtypes in PDAC (Collisson et al. 2011). However, whether macrophages undergo a tumor subtype-specific polarization is still unknown. To investigate potential tumor subtype-specific macrophage activation, macrophages were polarized with tumor-conditioned medium (TCM) from murine PDAC cell lines of different tumor subtypes, namely epithelial and mesenchymal tumor cell lines, to generate tumor-associated macrophages (epiTAMs or mesTAMs), which were characterized by RNA sequencing, followed by gene and protein expression analysis.

TAMs Showed Distinct Gene Expression After Stimulation

To investigate TAM heterogeneity upon culture with conditioned-medium from different PDAC tumor subtypes, TAMs were analyzed by RNAseq analysis. At first, TAMs clustering within the „M1-M2 macrophage frame“ was examined by integrating TAM RNAseq data with previously mentioned RNAseq data from M0, M1-like and M2-like macrophages. Hierarchical clustering revealed that epiTAMs and mesTAMs clustered together and both clustered closer with M0 and M2-like macrophages than with M1-like macrophages (Fig. 3.16).

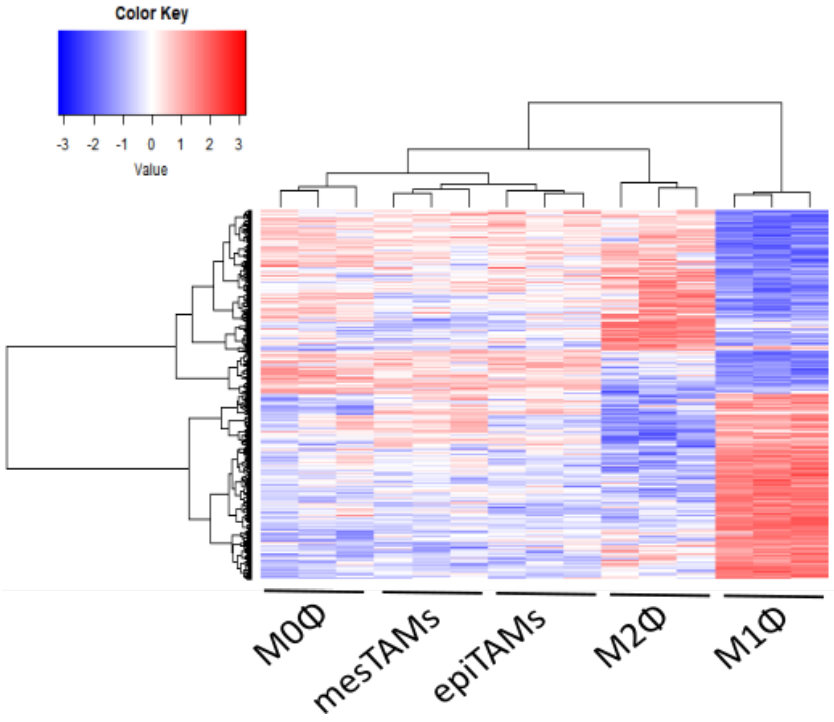

Figure 3.16: TAMs clustered together and were more closely related to anti-inflammatory M2-like than to pro-inflammatory M1-like macrophages. Supervized analysis of RNAseq-derived transcriptomes of M0, M1-like, M2-like, epithelial and mesenchymal tumor-associated macrophages (epiTAMs and mesTAMs). Color scale illustrates the relative expression level of mRNA across samples as a z-score: red represents an expression level above and blue an expression level below the mean (n=3).

Furthermore, investigation of differential gene expression revealed 181 genes, which were differentially expressed between epiTAMs and mesTAMs which included immune-related genes, e.g. *Ccl17* and *Ccl22* (Fig. 3.17).

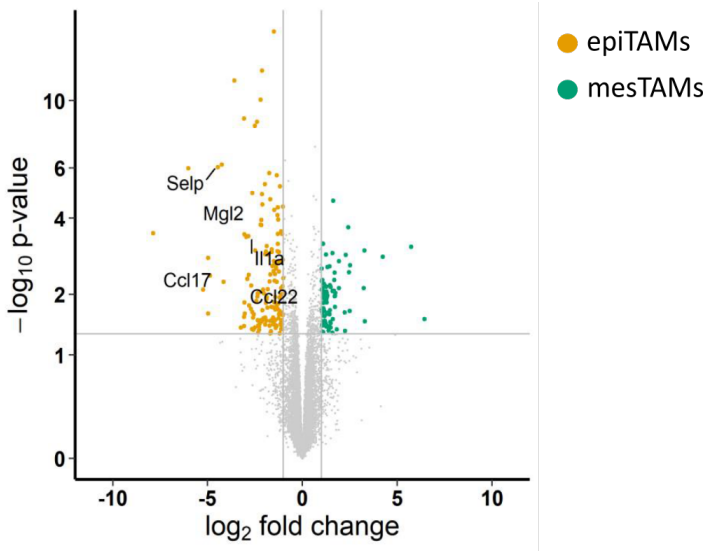

Figure 3.17: epiTAMs and mesTAMs showed distinct gene expression after TCM stimulation. Volcano plot showing fold changes for genes differentially expressed between epiTAMs and mesTAMs. In total, 181 genes were differentially expressed between epiTAMs and mesTAMs. Selected genes of interest are labeled. Orange: epiTAMs, green: mesTAMs ($p<0.05$, $-2 \leq \log_2 FC \geq 2$) (n=3).

For validation of RNAseq results, differentially expressed genes between epiTAMs and mesTAMs were further analyzed by qRT-PCR. Importantly, genes that were upreguated in epiTAMs in the RNAseq (*Selp*, *Il1a*, *Cish*, *Mgl2*) showed increased expression in epiTAMs in the qRT-PCR, supporting the RNAseq data (Fig. 3.18).

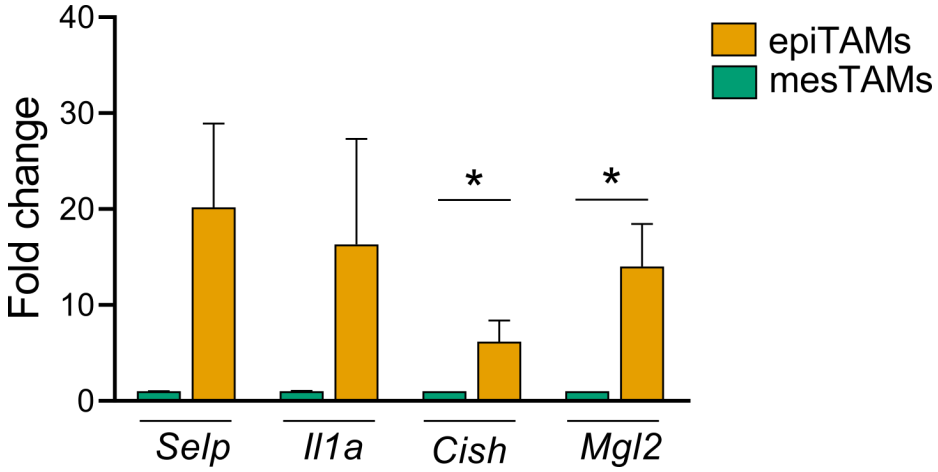

Figure 3.18: Quantitative real-time PCR validated results obtained from RNAseq. Genes, that were differentially expressed (upregulated in epiTAMs) between epiTAMs and mesTAMs were analyzed by qRT-PCR for validation of RNAseq results. Relative mRNA expression was analyzed by calculation of ΔC_t where Cyclophilin A served as reference control for normalization. For fold change expression of selected genes, fold changes of epiTAMs were normalized to mesTAMs. Fold changes were compared between epiTAMs and mesTAMs for each gene. Orange: epiTAMs, green: mesTAMs (Mann-Whitney test; *$p < 0.05$; n=3).

To examine enrichment of gene sets in different TAM subsets, genes were ranked based on $\log_2$ fold change and analyzed by GSEA, which revealed that epiTAMs were enriched for gene sets associated with inflammatory and IFNγ response as well as tumor necrosis factor (TNF) α signaling (Fig. 3.19A). In comparison, mesTAMs were enriched for gene sets associated with hypoxia, IL-4 treated macrophages and protein secretion (Fig. 3.19B). To visualize GSEA results in a network-based manner, results were analyzed with enrichment map (Fig. 3.19C). As depicted, epiTAMs were enriched in gene sets associated with immune response activation, but also in gene sets associated with ATPase activity, chemokine signaling and fatty acid metabolism, particularly cholesterol metabolism. In contrast, mesTAMs showed an enrichment in gene sets associated with nucleotide metabolism.

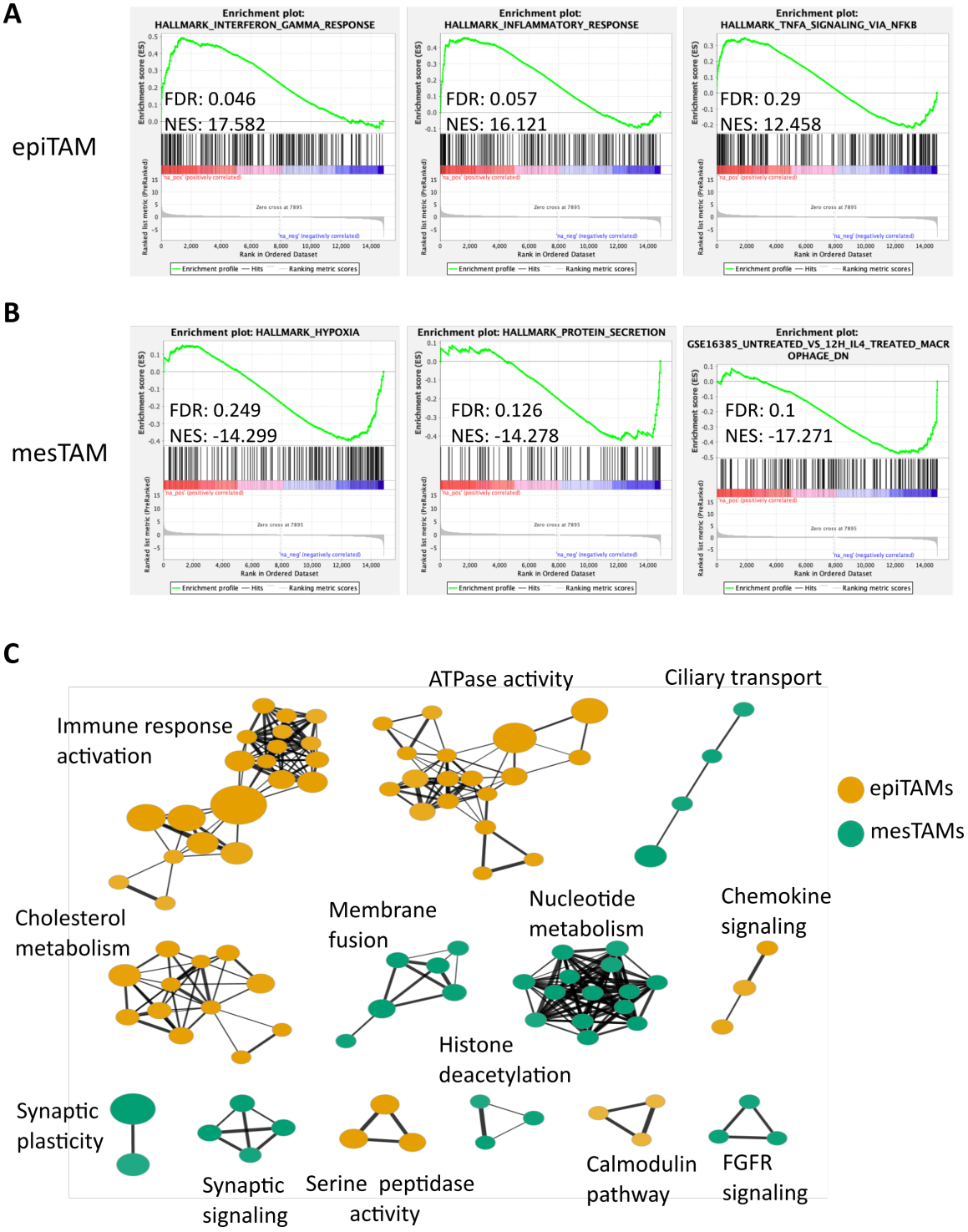

Figure 3.19: epiTAMs showed enrichment of pro-inflammatory activation, while mesTAMs were enriched in an IL-4 associated gene set. A-B: GSEA between epiTAMs and mesTAMs revealed gene sets, which were specifically enriched in (A) epiTAMs and (B) mesTAMs, respectively. (p<0.05, FDR<0.3; n=3). C: Enrichment Map for network-based visualization of enrichment results for epiTAMs and mesTAMs. Clusters were annotated according to corresponding functions of respective gene sets. p-values for node and edge cutoff p<0.05. Orange: epiTAMs, green: mesTAMs.

Next, we performed an upstream regulator prediction, analyzing the differentially expressed genes between TAM subsets using Ingenuity Pathway Analysis to identify potential upstream factors. Upstream regulator prediction revealed that a multitude of molecules was potentially responsible for the observed gene expression changes, with some pro-inflammatory factors, e.g. IFNγ, TNF and IL-2,

as well as factors with anti-inflammatory functions, e.g. IL-10Ra (Fig. 3.20A). To validate one of the predicted upstream regulators on the protein level, we performed an ELISA assay to detect IFNγ within the TCM as well as in TCM incubated with TAMs for 2 days (epiMCM, mesMCM). As depicted, IFNγ was not detectable in the TCM as well as in the TAM incubated TCM, indicating no expression of IFNγ by PDAC tumor cells as well as TCM polarized macrophages (Fig. 3.20B).

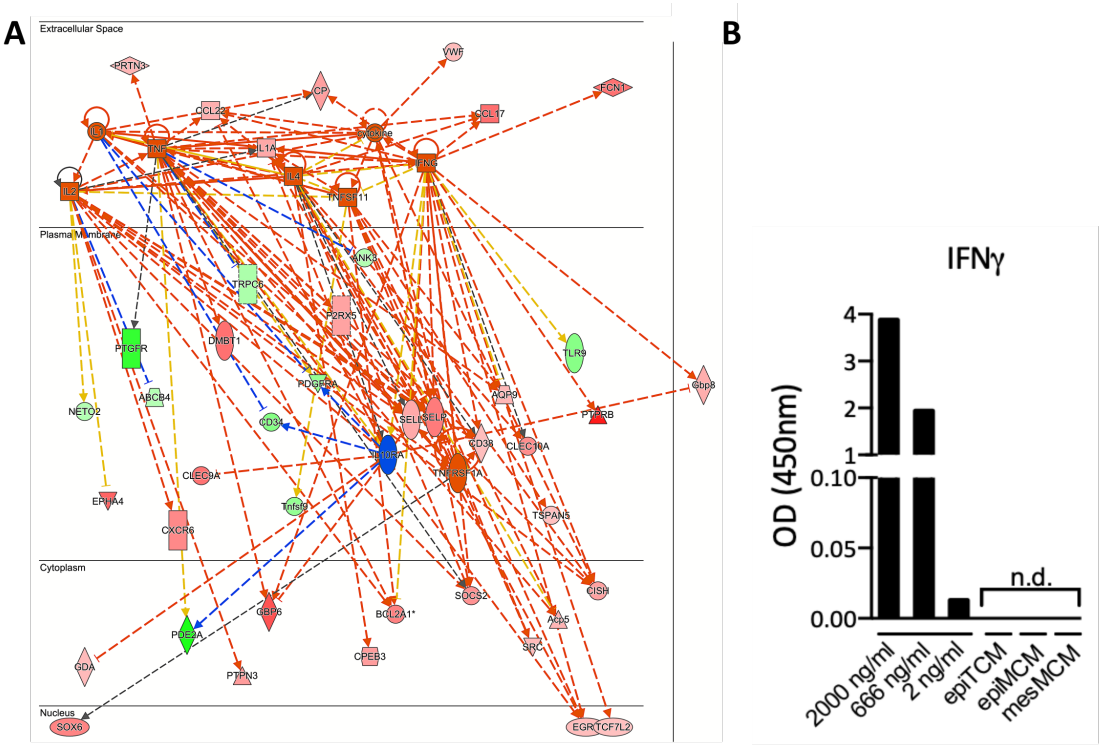

Figure 3.20: A mixture of pro- and anti-inflammatory factors were predicted to be responsible for differential gene expression between TAM subsets. A: Ingenuity Pathway Analysis for identification of upstream transcriptional regulators potentially explaining the observed gene expression changes between epiTAMs and mesTAMs. Predicted factors were organized by subcellular hierarchy to visualise subcellular and extracellular localization. B: Enzyme-linked immunosorbent assay (ELISA) of tumor-conditioned medium derived from murine epithelial PDAC cell lines (epiTCM) and of tumor-conditioned medium incubated for 48 h on epiTAMs (epiMCM) and mesTAMs (mesMCM) for detection of secreted IFNγ. n.d.=not detectable (n=1).

Tumor-Conditioned Medium Upregulated Immunological Gene Expression in TAMs

To analyze, whether TCM affected immunological gene expression in TAMs, TCM stimulated macrophages were analyzed by qRT-PCR. Therefore, macrophages were incubated with TCM from two epithelial and two mesenchymal murine PDAC cell lines to generate two different epiTAMs and two different mesTAMs and gene expression of stimulated TAMs was normalized to the expression of M0 macrophages.

As depicted, the two epiTAMs incubated with epithelial TCM showed a strong induction of pro-inflammatory genes e.g. *Il1β* and *Il6*, while anti-inflammatory gene expression e.g. *Arg1* was upregulated as well (Fig. 3.21A-B). Notably, *Il10* was the only anti-inflammatory gene which remained unchanged or downregulated in epiTAMs. The two different mesTAMs showed an upregulation of pro-inflammatory genes e.g. *Il1*β, while most of the anti-inflammatory genes were upregulated following TCM stimulation as well (Fig. 3.21C-D). Of note, *Arg1* was downregulated in one mesTAM subset, but highly upregulated in the other mesTAM subsets. Additionally, *Il10* was upregulated in the investigated mesTAMs in comparison to the two epiTAMs.

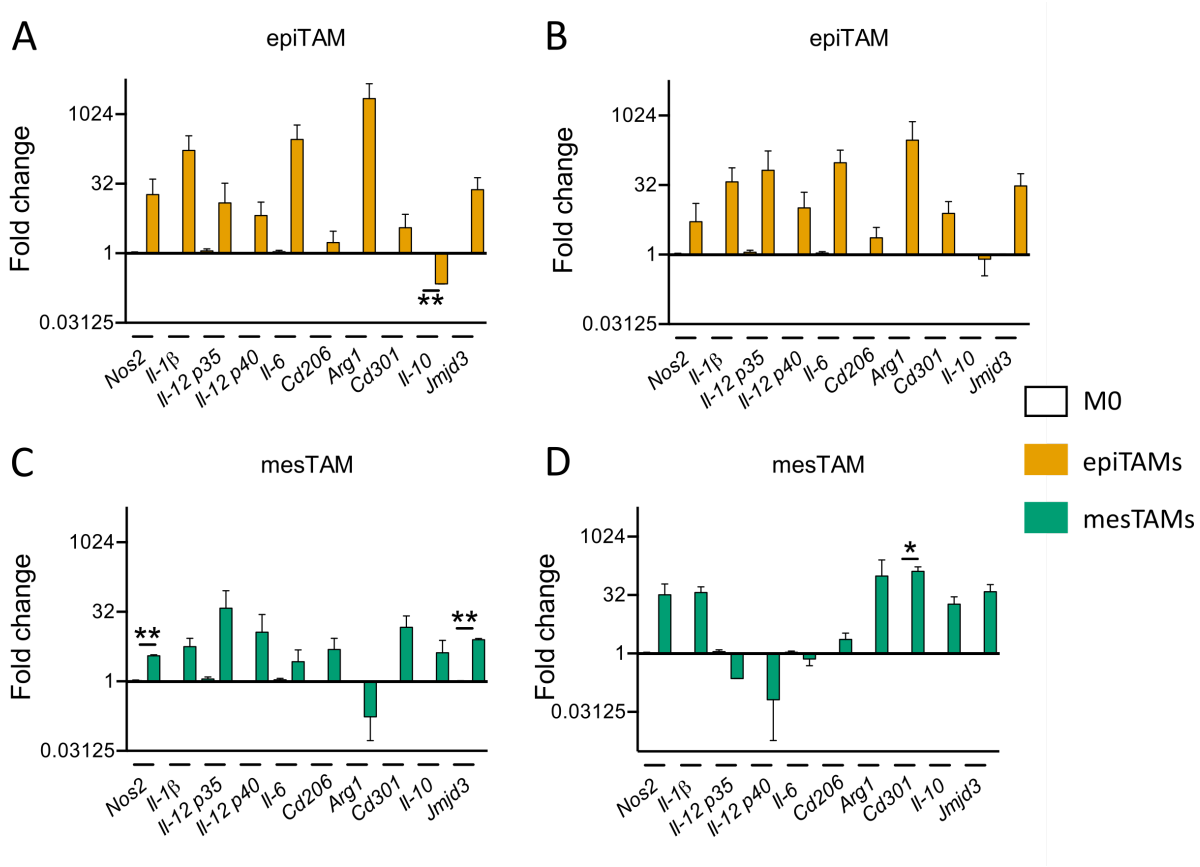

Figure 3.21: Murine TAMs showed induction of pro- and anti-inflammatory gene expression after TCM stimulation. Gene expression analysis of immune-related genes by quantitative real-time PCR. Relative mRNA expression was analyzed by calculation of ΔC_t where Cyclophilin A served as reference control for normalization. A-D: Fold change expression of epi TAMs and mesTAMs were normalized to M0 macrophages. Fold changes were compared between (A-B) epiTAMs and M0 and (C-D) mesTAMs and M0 macrophages for each gene. White: M0, orange: epiTAMs, green: mesTAMs (Mann-Whitney test; *p < 0.05, ** p < 0.01, n=2-3).

TAMs Showed Increased CD206 and CD80 Expression Following TCM Stimulation

To confirm TCM-mediated gene expression induction at protein level, epiTAMs and mesTAMs were analyzed for pro- and anti-inflammatory marker expression by flow cytometry. Following stimulation, expression of pro-inflammatory NOS2 was not affected, whereas CD80 expression was highly upregulated in all TAM subsets (Fig. 3.22A-B). CD80 expression was 10-fold upregulated in both epiTAMs and in one of the mesTAMs, whereas the other mesTAM showed a 20-fold upregulation. In addition, all TAMs showed augmented CD206 expression after TCM stimulation and the two mesTAMs showed a trend for higher upregulation of CD206 in comparison to the investigated epiTAMs (Fig. 3.22C). Furthermore, anti-inflammatory marker CD301 was only slightly upregulated in epiTAMs, while its expression was not affected in the two mesTAMs (Fig. 3.22D). However, it is noteworthy that CD301 was weakly expressed in all TAM subsets.

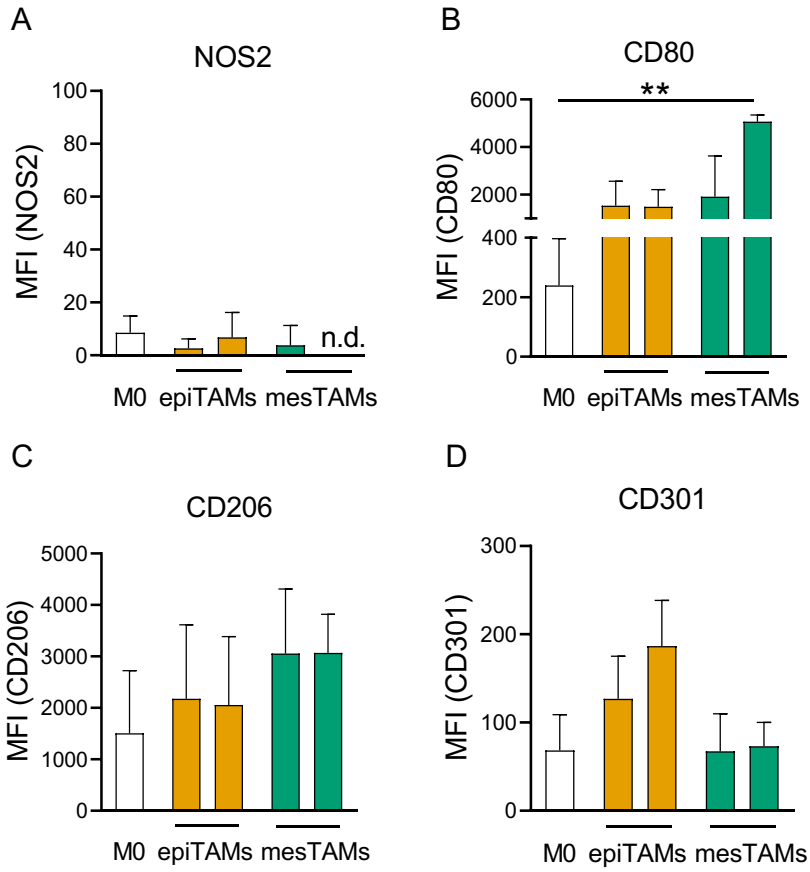

Figure 3.22: TAMs upregulated pro-inflammatory CD80 and anti-inflammatory CD206 protein expression after TCM stimulation. A-D: Protein expression level of pro-inflammatory marker proteins (A) NOS2 and (B) CD80 as well as anti-inflammatory marker proteins (C) CD206 and (D) CD301 were analyzed in M0 macrophages and in epiTAMs and mesTAMs following 48 h TCM stimulation by flow cytometry. Protein expression levels are shown as mean fluorescence intensity (MFI). n.d. = not detectable. White: M0, orange: epiTAMs, green: mesTAMs (Kruskal-Wallis test with Dunn's Post test; ** $p < 0.01$; n=3).

TAMs Showed Metabolic Adaptation After TCM Stimulation

To investigate, whether TCM stimulation interfered with central metabolism of TAMs, OXPHOS was estimated by measuring OCR in two epiTAMs and two mesTAMs. Basal respiration was increased following stimulation in all TAMs (Fig. 3.23A-B). While spare respiratory capacity was only slightly increased in epiTAMs, it was up to 4-fold increased in the two mesTAMs (Fig. 3.23B). Additionally, ATP production increased in one epiTAM and two mesTAMs to 60 pmol/min/RFU, while in one epiTAM ATP production was just slightly increased to 40 pmol/min/RFU (Fig. 3.23C).

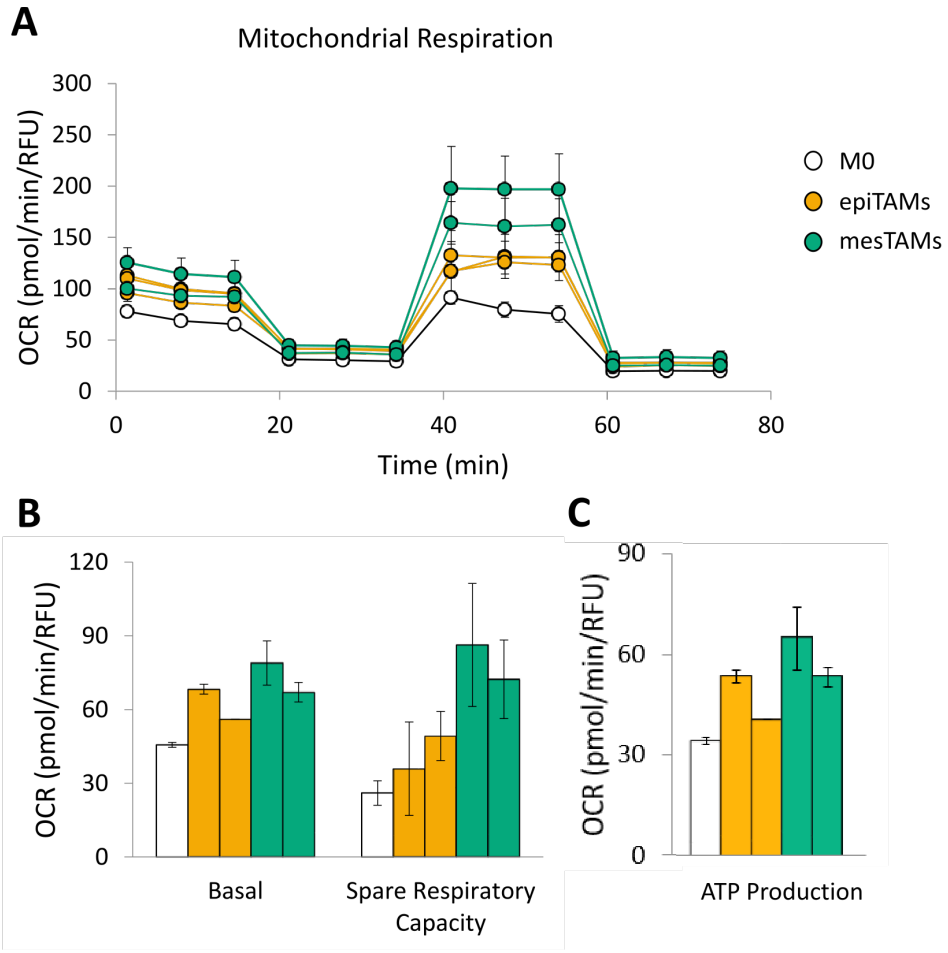

Figure 3.23: epiTAMs and mesTAMs showed increased mitochondrial respiration after TCM stimulation. A: Representative experiment showing mitochondrial respiration reflected by oxygen consumption rate (OCR) levels. OCR was detected in murine M0 macrophages as well as two epiTAMs and two mesTAMs under basal conditions followed by addition of oligomycin (2 µM), the uncoupler FCCP (1.5 µM) and the electron transport inhibitor Rotenone/AntimycinA (0.5 µM). B: Determination of basal respiration and spare respiratory capacity by OCR measurement. C: Determination of ATP production by OCR measurement. Cells were fixed and stained with DAPI and values were normalized according to respective cell numbers. White: M0, orange: epiTAMs, green: mesTAMs (n=2).

Besides determining OXPHOS, glycolytic rate was analyzed in epiTAMs and mesTAMs following TCM stimulation. While TAMs showed a slight decrease in glycolysis in comparison to M0 macrophages, glycolytic capacity of all TAMs was reduced to 20-40 mpH/min/RFU after TCM stimulation (Fig. 3.24A-B). Furthermore, glycolytic reserve of epiTAMs and mesTAMs was slightly decreased after TCM stimulation in comparison to M0 macrophages (Fig. 3.24B).

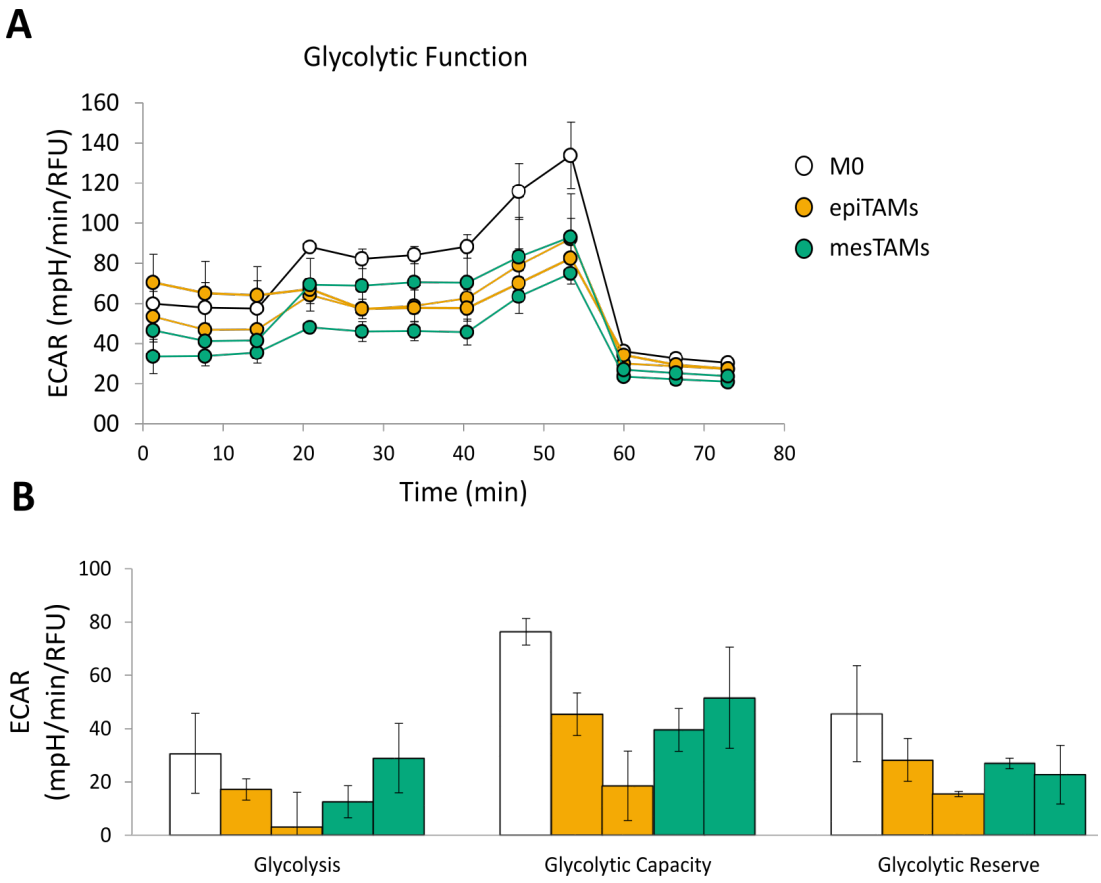

Figure 3.24: epiTAMs and mesTAMs showed decreased glycolysis after TCM stimulation. A: Representative experiment showing glycolytic function reflected by extracellular acidification rate (ECAR) levels. ECAR was detected in murine M0 macrophages as well as two epiTAMs and two mesTAMs under basal conditions followed by addition of glucose (10 mM), oligomycin (1 µM) and 2-deoxyglucose (50 mM). B: Determination of glycolysis, glycolytic capacity and glycolytic reserve by ECAR measurement. Cells were fixed and stained with DAPI and values were normalized according to respective cell numbers. White: M0, orange: epiTAMs, green: mesTAMs (n=2).

Next, we analyzed TCM glucose contents to ensure that the decreased glycolytic rates of TAMs were not due to a lack of glucose within the TCM. As depicted, unconditioned medium contained app. 400 mg/dl glucose (Fig. 3.25). After 3 days of tumor cell incubation, the TCM glucose concentration decreased to app. 120-200 mg/dl in all investigated tumor conditioned media, showing that glucose was still present inside TCM. Importantly, incubation of TAMs for 6 h, 24 h and 48 h in respective TCM did not decrease glucose concentration over time, supporting the observations from the metabolic flux analysis that TAMs preferentially used OXPHOS rather than glycolysis for energy production.

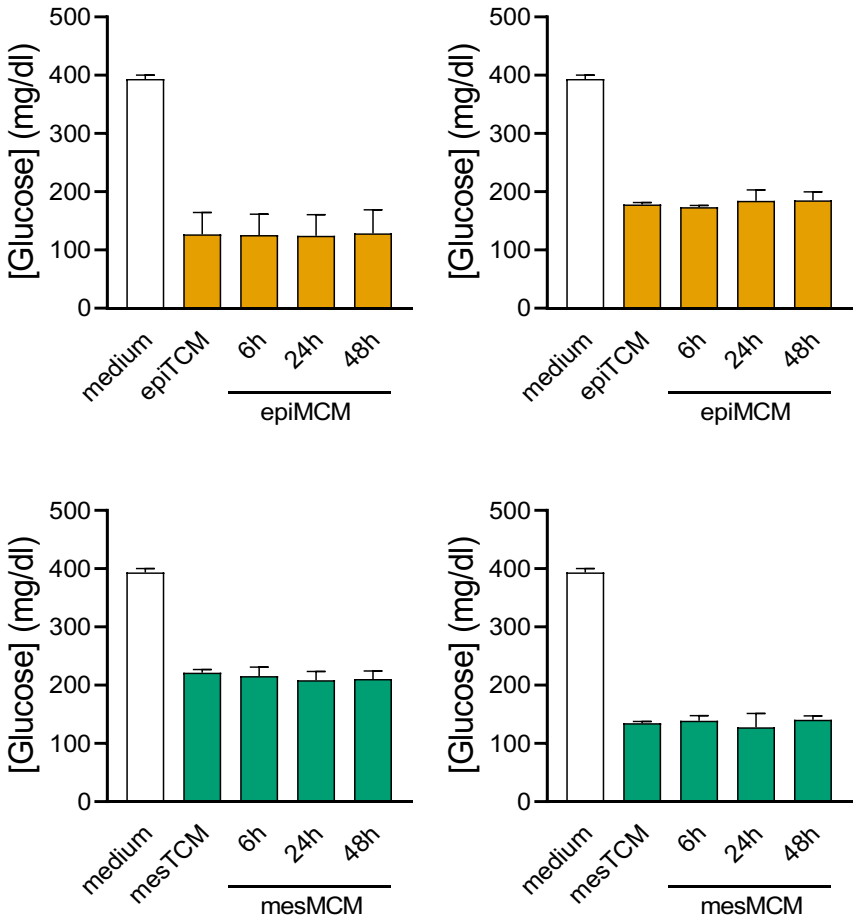

Figure 3.25: Glucose concentrations in macrophage-conditioned medium (MCM) remained constant over time. Glucose concentrations from fresh, unconditioned medium (medium), TCM after 72 h incubation with two epithelial (epiTCM) and two mesenchymal tumor cells (mesTCM) and from TCM after 6 h, 24 h and 48 h of epiTAM and mesTAM incubation (epiMCM, mesMCM) were measured. White: unconditioned medium, orange: TCM of epithelial tumor cells and epiMCM of epiTAMs, green: TCM of mesenchymal tumor cells and mesMCM of mesTAMs (Kruskal-Wallis test with Dunn's Post test; n=3).

Taken together, these results showed that murine macrophages induced pro- and anti-inflammatory gene and protein expression following TCM stimulation. EpiTAMs and mesTAMs could not be distinguished by conventional M1-like and M2-like macrophage markers. However, epiTAMs were enriched in gene sets associated with inflammatory response, while mesTAMs showed enrichment in gene sets associated with hypoxia. Furthermore, epiTAMs and mesTAMs showed increased OXPHOS and decreased glycolytic capacity upon TCM stimulation, although no tumor subtype-specific influence on macrophage metabolism could be observed.

Epithelial TCM Induced HIF1A Protein Stabilization in epiTAMs Without Affecting Pathway Signaling Tumor Subtype-Specifically

To identify potential differentially regulated pathways between epiTAMs and mesTAMs, we focused on the RNAseq results and our attention was drawn to the hypoxia-associated gene set (Fig. 3.19B), which was specifically enriched in mesTAMs. Hypoxic signaling in macrophages is known to be mediated by HIF1A and is associated with anti-inflammatory and pro-angiogenic properties, e.g. increased expression of *Arg1* and *Vegfa* (Colegio et al. 2014). To investigate HIF1A signaling under normoxic conditions in the different TAM subsets, we first analyzed the kinetics of HIF1A protein level following TCM stimulation in one epiTAM and one mesTAM by western blot and normalized the HIF1A protein level of TAMs to the HIF1A protein level of respective M0 macrophages (Fig. 3.26A-B). The data revealed that HIF1A protein level was increased after 4 h of TCM stimulation in epiTAM in comparison to M0 macrophages and mesTAM. Consequently, two epiTAMs and two mesTAMs were incubated for 4 h with TCM and HIF1A protein levels were analyzed by western blot and quantified (Fig. 3.26C-D). The results showed that HIF1A protein levels were upregulated 2-fold in epiTAMs following TCM stimulation, while they remained mostly unchanged in mesTAMs (Fig. 3.26D).

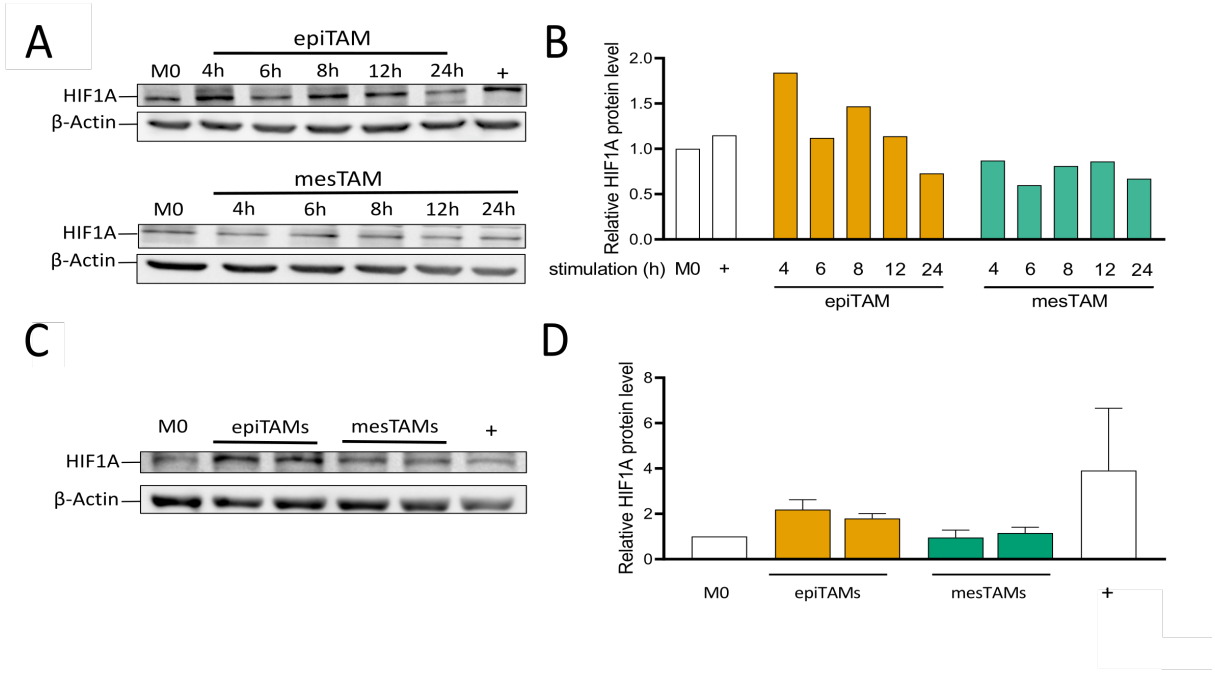

Figure 3.26: HIF1A protein is stabilized after TCM stimulation in murine epiTAMs. A: Western blot of kinetics experiment showing HIF1A protein level of M0 macrophages, one epiTAM and one mesTAM after different time points (4 h, 6 h, 8 h, 12 h and 24 h) of TCM stimulation. Additionally, M0 macrophages were treated with 1 mM DMOG for 2 h as positive control. β–actin served as loading control (n=1). B: Band intensity of western blots was quantified by densitometry and normalized to β–actin. To calculate relative HIF1A protein level, protein levels of TCM stimulated TAMs were normalized to the protein level of M0 macrophages (n=1). C: Representative western blot showing HIF1A protein level of murine M0 macrophages, DMOG treated positive control as well as two epiTAMs and two mesTAMs after 4 h of TCM stimulation. β–actin served as loading control (n=3) D: Quantification of HIF1A protein level of M0 macrophages, DMOG treated positive control as well as two epiTAMs and two mesTAMs after 4 h of TCM stimulation. Band intensity of western blots was quantified by densitometry and normalized to β–actin. To calculate relative HIF1A protein level, protein levels of TCM stimulated TAMs were normalized to the protein level of M0 macrophages. White: M0 and M0 treated with 1 mM DMOG, orange: epiTAMs, green: mesTAMs (Kruskal-Wallis test with Dunn's Post test; n=3).

To further address, whether the increase in HIF1A protein level in epiTAMs resulted in an increased activation of HIF1A signaling, we analyzed the expression of known HIF1A downstream target genes by qRT-PCR. First, we analyzed the kinetics of HIF1A target gene expression following TCM stimulation in one epiTAM and one mesTAM. The kinetics experiment revealed differences in HIF1A target gene expression after 6h of TCM stimulation in *Arg1*, *Vegfa* and *Egln3* between epiTAM and mesTAM (Fig. 3.27A). Following, HIF1A target gene expression was quantified after 6 h of TCM stimulation in two epiTAMs and two mesTAMs (Fig. 3.27B). The results showed that both epiTAMs and mesTAMs showed a strong upregulation of HIF1A target genes *Arg1*, *Egln3* and *Slc2a1* on the transcriptional level. While *Egln3* and *Slc2a1* expression levels increased 8-fold to 64-fold, *Arg1* expression increased 300-fold to 2000-fold in the investigated TAMs. Additionally, *Vegfa* expression levels increased 2-fold to 6-fold in all TAMs after TCM stimulation. However, both epiTAMs and mesTAMs showed an increased expression of HIF1A downstream target genes, indicating that HIF1A signaling is activated in TAMs regardless of tumor subtypes.

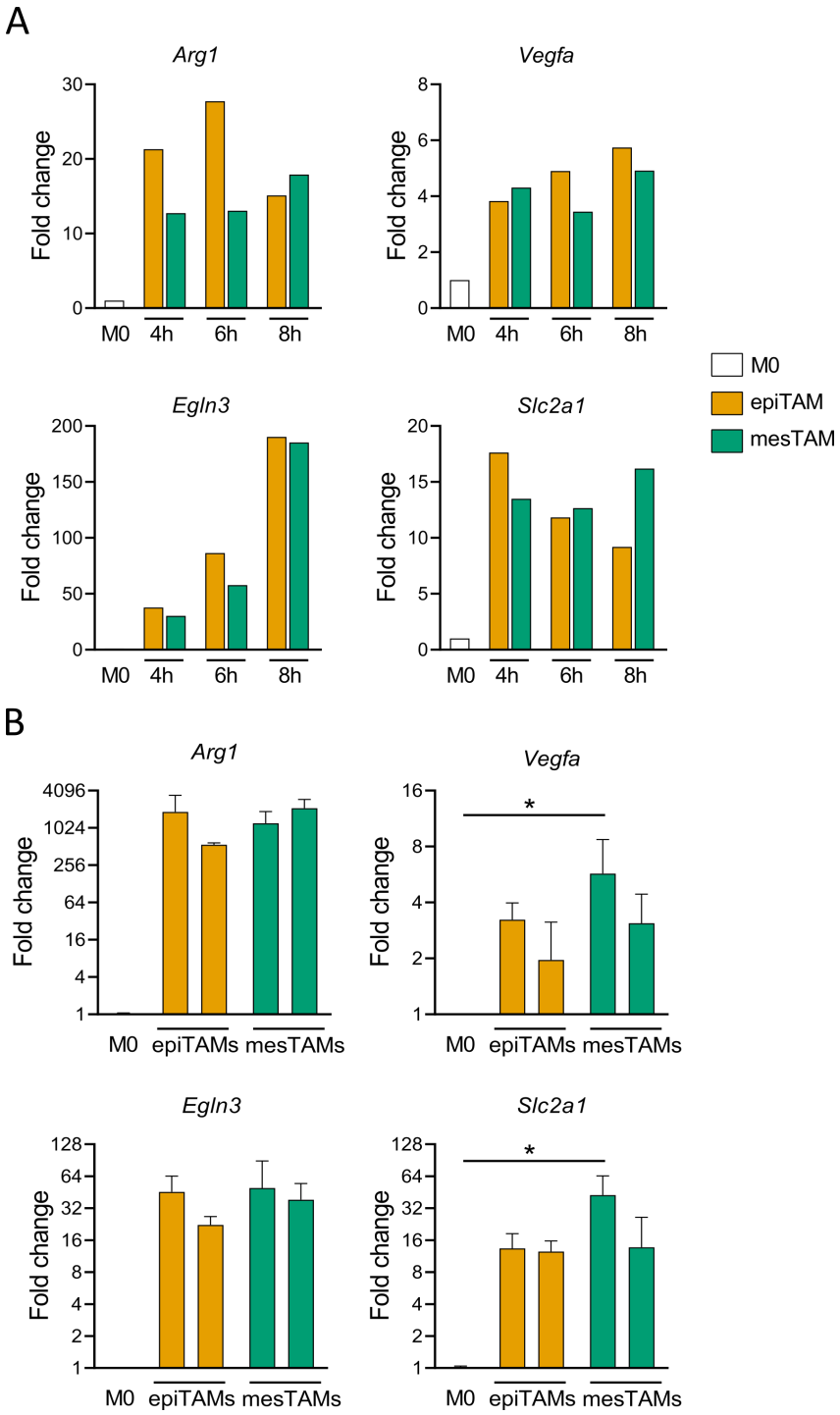

Figure 3.27: TAMs showed increased expression of HIF1A target genes following TCM stimulation tumor subtype-independently. A: M0 macrophages were stimulated for 4 h, 6 h and 8 h with TCM from one epithelial and one mesenchymal PDAC cell line or left unstimulated as control to examine kinetics of HIF1A-mediated downstream target gene expression under normoxic conditions. At indicated time points, RNA was isolated and gene expression of HIF1A target genes was analyzed by calculation of ΔC_t where Cyclophilin A served as reference control for normalization. Fold change expression of epiTAM and mesTAM were normalized to M0 macrophages. Fold changes were compared between epiTAM and mesTAM for each time point and gene. (n=1). B: M0 macrophages were stimulated for 6 h with TCM from two epithelial and two mesenchymal PDAC cell lines or left unstimulated as control. RNA was isolated and gene expression of HIF1A target genes was analyzed by calculation of ΔC_t where Cyclophilin A served as reference control for normalization. . Fold change expression of epiTAMs and mesTAMs were normalized to M0 macrophages. Fold changes were compared between epiTAMs and mesTAMs for each gene. White: M0, orange: epiTAMs, green: mesTAMs (Kruskal-Wallis test with Dunn's Post test, n=3).

Murine mesTAMs Showed Increased Sensitivity Against MEK Inhibition

Because PDAC tumor subtype-specific TAMs could not be distinguished based on previously described surface protein marker panel, we sought to investigate whether epiTAMs and mesTAMs showed differential dependency on intracellular signaling pathways. Since M0, M1-like and M2-like macrophages were already shown to possess differences in sensitivity against MEKi treatment, we decided to investigate potential differences of epiTAMs and mesTAMs regarding MAPK signaling.

First, we performed a leading edge analysis of differentially expressed genes between epiTAMs and mesTAMs from the RNAseq using the reactome gene set database from GSEA. The results showed, that the top genes in the leading edge were associated with MAPK-signaling (*Map2k1, Mapk1, Sos1, Kras, Raf1*) and were enriched in mesTAMs (Fig. 3.28A). MAPK signaling has been shown to be associated with a variety of different biological processes in macrophages, e.g. survival (Wang et al. 2007). Therefore, TAM viability following treatment with pharmacologically relevant MEKi concentrations was examined by IC_{50} determination. Cell viability analysis revealed that TAMs polarized with both conditioned-medium from epithelial and mesenchymal PDAC cell lines showed decreased sensitivity to MEKi-induced cell death in comparison to M0 macrophages (Fig. 3.28B). Furthermore, mesTAMs were more sensitive to higher MEKi concentrations than epiTAMs. At 0.77 µM MEKi concentration, app. 70% of mesTAMs induced cell death, while epiTAMs induced cell death just in 25-30% of the cells (Fig.3.28B).

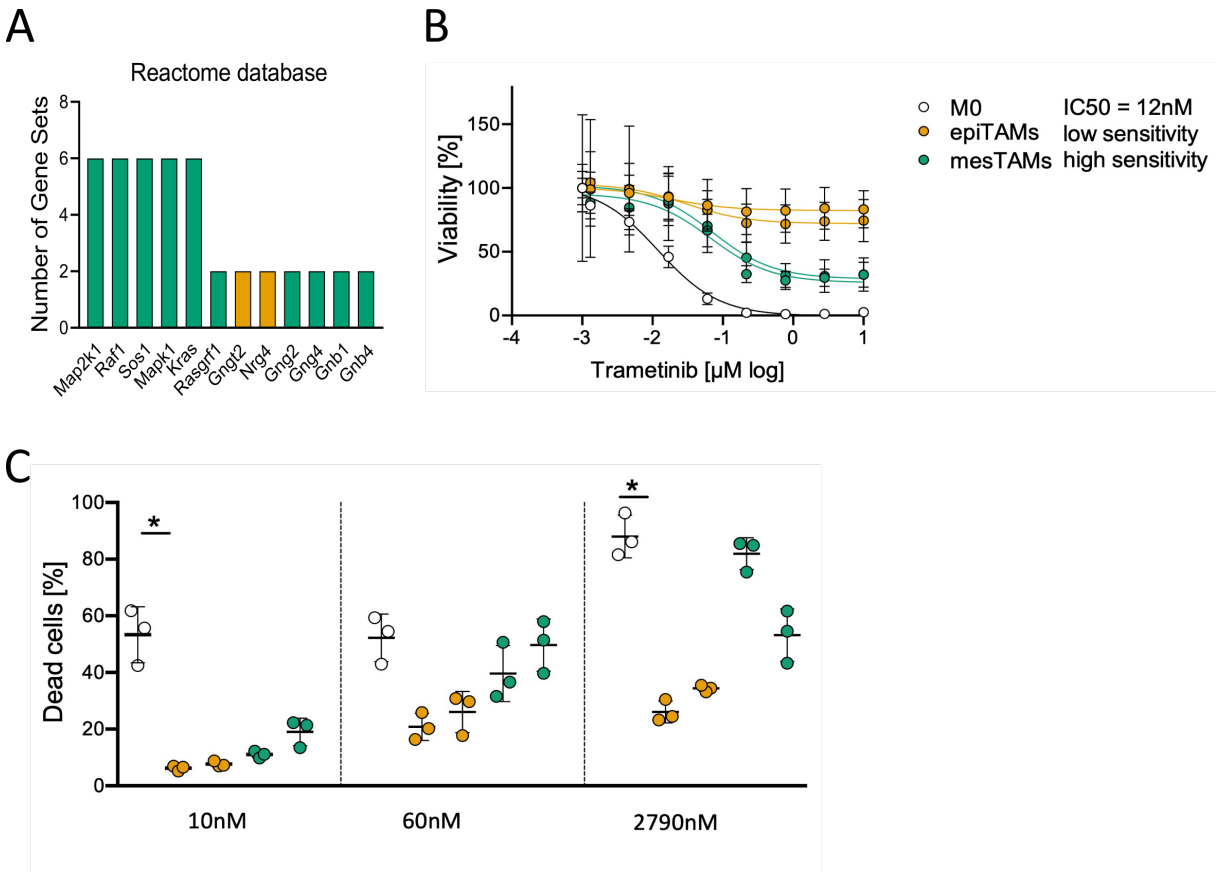

Figure 3.28: Murine mesTAMs showed increased sensitivity against MEKi-induced cell death. A: Leading edge analysis of top enriched genes from reactome gene set database between epiTAMs and mesTAMs. Green bars indicate genes associated with mesTAMs, while orange bars indicate genes associated with epiTAMs ($p<0.05$, FDR<0.25). B: IC_{50} determination of murine M0 macrophages as well as two epiTAMs and two mesTAMs. Polarized cells were seeded on pre-printed 96 well plates containing pharmacologically relevant MEKi concentrations (1.3 nM-10 µM) and incubated for 72 h before measuring cell viability by cell titer glo assay (Kruskal-Wallis test with Dunn's Post test of Area Under Curve; n=3). C: MEKi-induced cell death was determined by propidiumiodide (PI) staining of dead cells by flow cytometry. Polarized cells were treated with different MEKi concentrations (10 nM, 60 nM and 2.79 µM) and incubated for 72 h before PI staining and subsequent flow cytometric analysis. White: M0, orange: epiTAMs, green: mesTAMs (Kruskal-Wallis test with Dunn's Post test; *$p < 0.05$; n=3).

To validate the cell viability results, cell death induction following MEKi treatment was examined by PI staining of dead cells using flow cytometry. Following MEKi treatment, M0 macrophages showed high sensitivity against MEKi-induced cell death with app. 50% dead cells at 10 nM MEKi concentration, while all TAM subsets showed 5-15% of dead cells (Fig. 3.28C). At 60 nM MEKi concentration, the relative amount of dead epiTAMs and mesTAMs increased ranging from 20-45%, with epiTAMs showing a slight tendency to be less sensitive to MEKi-induced cell death than mesTAMs. At 2.79 µM MEKi concentration, app. 90% of M0 macrophages induced cell death. In comparison, mesTAMs induced cell death in 60-90% of the cells, while epiTAMs induced cell death just in 20-30% of the cells.

To investigate, whether the MAPK-dependency of epiTAMs and mesTAMs was reversible, we generated reverted mesTAMs by additionally incubating mesTAMs for 2 days in TCM from epithelial tumor cells before determining cell viability following MEKi treatment by IC_{50} measurement (Fig. 3.29).

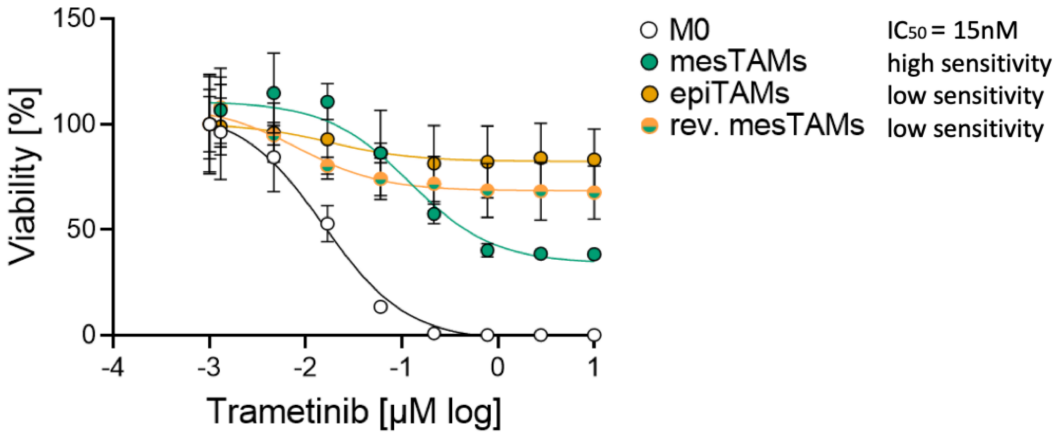

Figure 3.29: MEKi sensitivity of TAMs is reversible. IC_{50} determination of murine M0 macrophages, epiTAMs, mesTAMs and reverted mesTAMs (rev. mesTAMs). Polarized cells were seeded on pre-printed 96 well plates containing pharmacologically relevant MEKi concentrations (1.3 nM-10 µM) and incubated for 72 h before measuring cell viability by cell titer glo assay. For rev. mesTAM generation, mesTCM was removed from mesTAMs and replaced by epiTCM for 48 h prior to IC_{50} determination. White: M0, orange: epiTAMs, green: mesTAMs, green-orange halfdots: reverted mesTAMs (Kruskal-Wallis test with Dunn's Post test of Area Under Curve; n=3).

The results revealed that epiTAMs showed a low sensitivity against MEKi-induced cell death, while mesTAMs were more sensitive to MEKi concentration above 100 nM. Importantly, rev. mesTAMs showed a lower sensitivity against MEKi-induced cell death in comparison to mesTAMs at higher MEKi concentrations. While only 45% of mesTAMs were viable at a MEKi concentration of 2.79 µM, approximately 70% of rev. mesTAMs were viable. In addition, the nonlinear regression curve of rev. mesTAMs closer resembled the curve of epiTAMs than the curve of mesTAMs, indicating a reversibility of MEKi sensitivity between both TAM subsets.

Taken together, these results revealed that murine mesTAMs were more sensitive to MEKi-induced cell death than epiTAMs. Additionally, the results revealed that MEKi sensitivity was reversible, underlining the high plasticity of these cells.

Human TAMs Showed Increased Marker Protein Expression Following TCM Stimulation Tumor Subtype-Independently

We next aimed to validate these findings in human PDAC. Therefore, we incubated human CD14^{+} monocytes with TCM from two human epithelial and mesenchymal PDAC cell lines to generate two human epiTAMs and mesTAMs, respectively. After TCM stimulation, macrophage protein expression was examined by flow cytometry (Fig. 3.30).

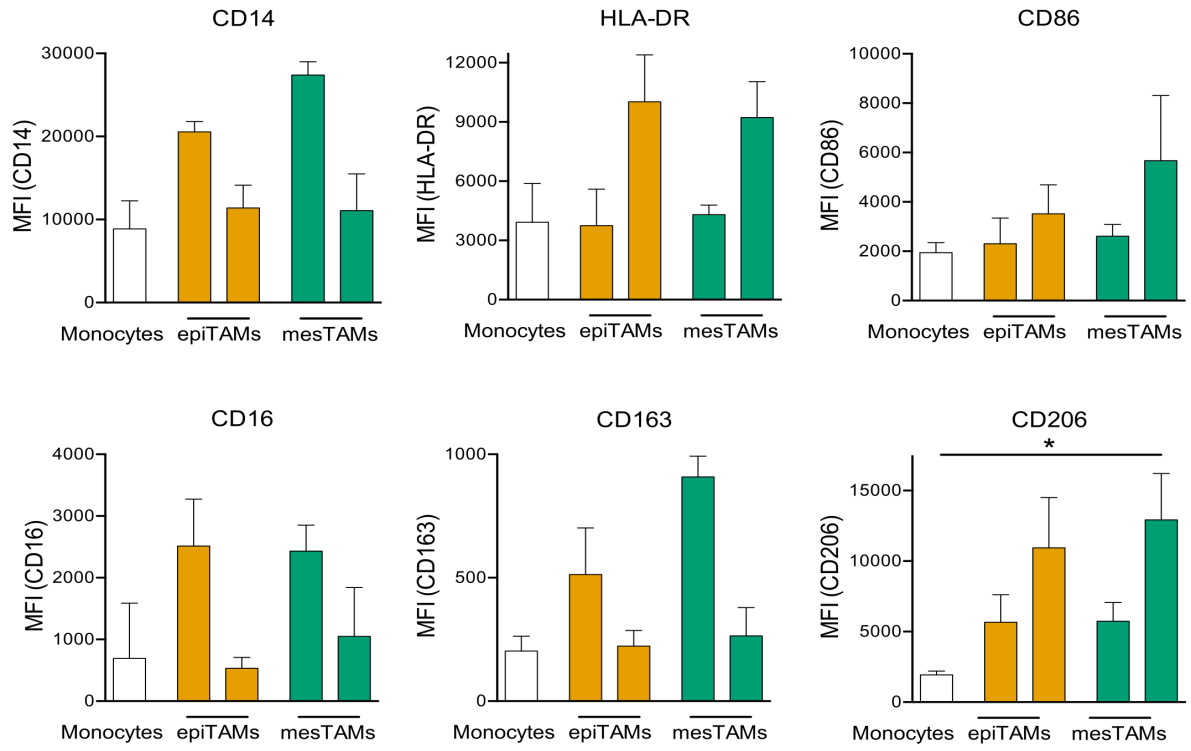

Figure 3.30: Human TAMs induced pro- and anti-inflammatory protein expression after TCM stimulation. CD14+ monocytes were incubated for 72 h with TCM from two epithelial and two mesenchymal human PDAC cell lines or left unstimulated as control. After TCM incubation, expression level of pro-inflammatory (CD14, HLA-DR, CD86) and anti-inflammatory (CD16, CD163, CD206) proteins was investigated by flow cytometry. Protein expression levels are shown as mean fluorescence intensity (MFI). White: monocytes, orange: epiTAMs, green: mesTAMs (Kruskal-Wallis test with Dunn's Post test; n=3).

Flow cytometry revealed an increased expression of pro- and anti-inflammatory marker proteins following TCM stimulation. While one epiTAM and one mesTAM were characterized by an upregulated protein expression of CD16, CD163 and CD14 after TCM stimulation, the other epiTAM and mesTAM were characterized by an upregulated expression of CD206, HLA-DR and CD86. Importantly, immunophenotypes of epiTAMs and mesTAMs could not be distinguished based on conventional pro- and anti-inflammatory marker proteins, supporting the observations made from mice.

Human mesTAMs Showed Increased Sensitivity to MEK Inhibition

Since we observed tumor subtype-specific differences in murine epiTAMs and mesTAMs regarding MEKi sensitivity, we asked whether human TAMs also showed PDAC subtype-specific MEKi sensitivity. Therefore, human monocytes were incubated with TCM from three different epithelial and mesenchymal human PDAC cell lines and cell viability was analyzed by IC_{50} determination (Fig. 3.31).

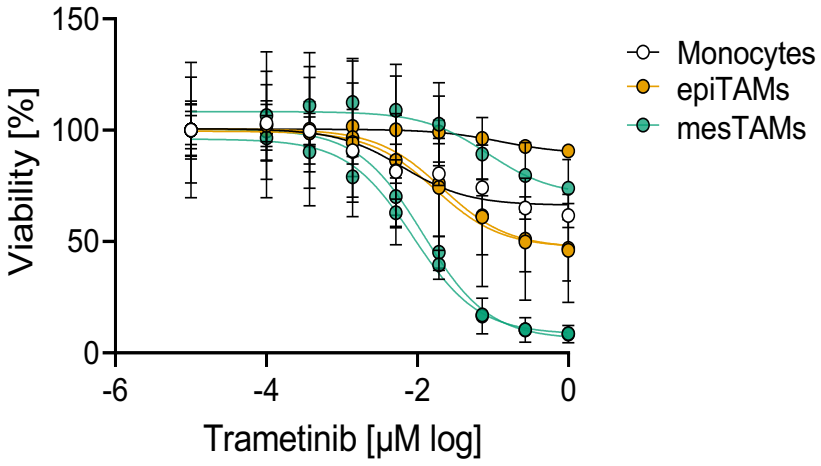

Figure 3.31: Human mesTAMs showed decreased viability following MEKi treatment. IC_{50} determination of human monocytes, three epiTAMs and three mesTAMs. Polarized cells were seeded on pre-printed 96 well plates containing pharmacologically relevant MEKi concentrations (0.1 nM-1 µM) and incubated for 72 h before measuring cell viability by cell titer glo assay. White: monocytes, orange: epiTAMs, green: mesTAMs (Kruskal-Wallis test with Dunn's Post test of Area Under Curve; n=3).

Cell viability analysis revealed that human monocytes and epiTAMs were less sensitive to MEKi-induced cell death than mesTAMs. While two epiTAMs showed approximately 50% viable cells at 1 µM MEKi concentration, one epiTAM showed viability of approximately 90%. In comparison, two mesTAMs were more sensitive to MEKi than epiTAMs with only approximately 5% of the cells being viable at a MEKi concentration of 1 µM. However, not all investigated mesTAMs showed a high MEKi sensitivity, since one mesTAM revealed approximately 80% viability at high MEKi concentrations.

Taken together, these results supported the trend observed from the previous mouse data that mesTAMs showed an increased sensitivity against MEKi in comparison to epiTAMs.

Mesenchymal Tumor Cell-Surrounding Microenvironment Showed Increased MAPK Signaling

To investigate, whether the difference regarding MAPK signaling between epithelial and mesenchymal TAMs may be present *in situ*, resected primary human PDAC tissue was stained by multiplex immunofluorescence (Figure 3.32). Different tumor subtypes were classified based on previously published tumor subtype-enriching marker expression of GATA6 for epithelial tumor areas (Fig. 3.32A) and KRT81 for mesenchymal tumor areas, respectively (Fig 3.32B) (Martinelli et al. 2017; Muckenhuber et al. 2018). In addition, resected tissue was stained for $CD68^{+}$ macrophages and Phospho-ERK (pERK) as indicator for MAPK signaling activity.

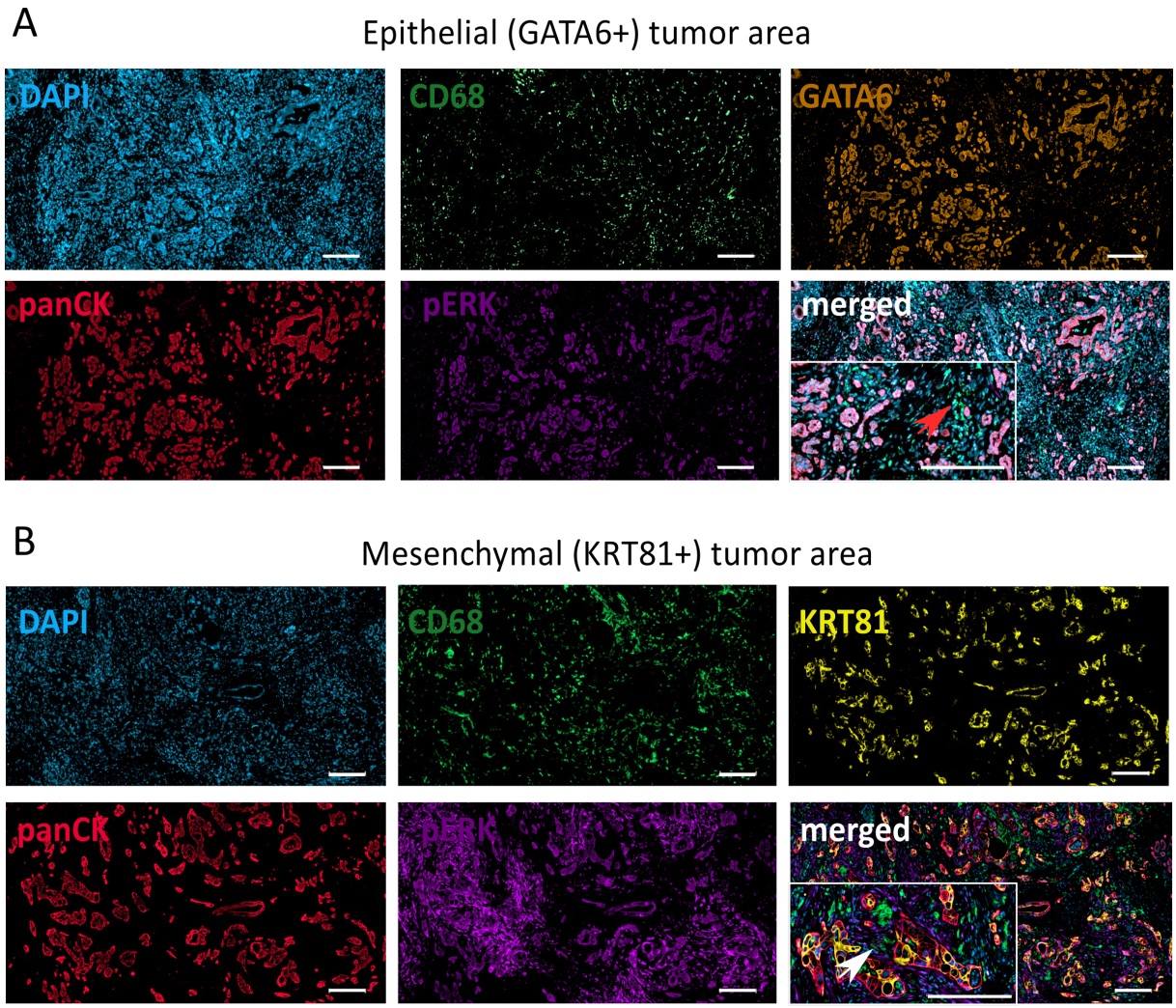

Figure 3.32: Mesenchymal tumor areas showed increased MAPK signaling in the stroma. A: Multiplex immunofluorescence staining of an epithelial (nuclear GATA6+) tumor area for DAPI, macrophages (CD68+), epithelial tumor cells (GATA6+), tumor cells (panCK+) and MAPK signaling (pERK+) from one resected primary human PDAC. B: Multiplex immunofluorescence staining of a mesenchymal (KRT81+) tumor area for DAPI, macrophages (CD68+), mesenchymal tumor cells (KRT81+), tumor cells (panCK+) and MAPK signaling (pERK+) from a resected primary human PDAC. Red arrowhead: Macrophages in epithelial tumor area. White arrowhead: Macrophages in mesenchymal tumor area. Magnification: 25x, 100x. Scale bars represent 100 µm.

Multiplex immunofluorescence staining identified tumor infiltrating $CD68^+$ macrophages in both epithelial and mesenchymal tumor areas at comparable frequencies. Tumor cells in epithelial tumor areas were identified as $panCK^+$/nuclear-$GATA6^+$ (classical PDAC). pERK signals were mainly detected within the tumor cell compartment with only a few stromal cells showing pERK signal.

Mesenchymal tumor areas (quasi-mesenchymal PDAC) were identified by $panCK^+$/$KRT81^+$ cells. In contrast to epithelial tumor areas, pERK signals in mesenchymal tumor areas mainly derived from the tumor microenvironment, which surrounded $panCK^+$/$KRT81^+$ tumor cells. Importantly stainings of CD68 and pERK, at least partially, co-localized, indicating an increased MAPK signaling activity of $CD68^+$ macrophages in mesenchymal tumor areas when compared to epithelial area.

Taken together, these results are in concordance with human mesTAMs being likely more sensitive to MEKi-induced cell death than epiTAMs. Importantly, multiplex immunofluorescence staining revealed a co-localization of macrophages with increased pERK signal within the microenvironment of human mesenchymal tumor areas, indicative of an increased MAPK signaling in macrophages residing in these tumor areas *in vivo*.

Discussion

MEK Inhibition Depletes M2-like Macrophages From PDAC Tumor Microenvironment

Molecular targeted therapies have demonstrated improved treatment efficacy and have expanded the spectrum of treatment modalities for cancer patients. Besides targeting malignant cells directly, evidence points towards therapeutic benefits for therapies targeting the tumor microenvironment. In this work, we sought to investigate the effect of MAPK pathway inhibition by the MEK inhibitor trametinib on anti-inflammatory M2-like macrophages, which frequently infiltrate the microenvironment of murine and human PDAC tumors and have been shown to be involved in a multitude of tumor-promoting processes (Candido et al. 2018; Cheung et al. 2018; Gardian et al. 2012; Zhu et al. 2017). The data revealed that MEKi-treated genetic mouse model of spontaneous PDAC, *CKP*, showed a downregulation of M2-like macrophages at the transcriptomic and protein level. Quantification of immunohistochemical staining of *CKP* control- and MEKi-treated tumors highlighted that the quantity of M2-like macrophages was strongly decreased after MEKi treatment, while flow cytometry showed that the remaining macrophages did not show an upregulation of pro-inflammatory marker proteins following MEKi treatment. Furthermore, flow cytometry revealed that $CD206^+$ macrophages decreased in relative number and that CD206 protein expression level was decreased, whereas $CD301^+$ macrophages increased in relative number and protein expression level. These data suggested that macrophages did not repolarize towards a pro-inflammatory M1-like macrophage phenotype upon MEKi treatment, even though the frequency and expression levels of different anti-inflammatory marker proteins changed following MEKi treatment.

Interestingly, $CD11b^+$ myeloid cells were restored after long-term MEKi, while $F4/80^+$ macrophage numbers were still suppressed, pointing towards a tumor infiltration of myeloid cells other than macrophages. Nywening et al. showed that targeting macrophage recruitment by CCR2 receptor inhibition improves anti-tumor immunity in a preclinical model of PDAC, albeit with a compensatory infiltration of tumor-associated neutrophils (TANs) resulting in a persistent immunosuppressive microenvironment, which led to therapy resistance (Nywening et al. 2018). However, whether the recruited myeloid cell population following long-term MEK inhibition consists, at least in part, of TANs and how these cells might influence tumor progression and drug resistance still needs to be determined.

Before dissecting potential effects of MEK inhibition on macrophage polarization, pro- and anti-inflammatory macrophages were generated *in vitro* and polarization states were confirmed on transcriptomic, protein and metabolic level. Transcriptionally, while there were trends of

downregulation of anti-inflammatory genes in M0 and M1-like macrophages following MEKi treatment, slight upregulation was observed in M2-like macrophages. However, MEKi treatment had only minimal effects on the protein level of the investigated marker proteins, indicating that MEKi did not affect macrophage polarization *in vitro*. In comparison to the *in vitro* experiments, CD206 and CD301 protein expression was influenced on the protein level following MEKi treatment *in vivo*. A possible explanation for the difference between *in vitro* and *in vivo* results might be that M2-like macrophages were polarized solely with IL-4 and IL-13 *in vitro*, whereas M2-like macrophages were exposed to a plethora of different stimuli *in vivo*, thereby showing differences in their polarization state, which might influence cellular response to MEKi. Another possible reason might be that the marker protein expression changes observed *in vivo* were not due to a direct effect of the MEKi treatment on M2-like macrophages, but due to the effect of MEKi on cells other than macrophages, which theirselfs affected protein expression in M2-like macrophages.

MAPK signaling is known to be involved in a variety of processes in macrophage biology, ranging from regulation of differentiation, survival and proliferation to immune responses (Gosse et al. 2005; Neamatallah 2019; Yu et al. 2012). It is mediated by different canonical pathways, e.g. via ERK1/2, ERK5, JNK1/2/3 and p38, which get activated by various stimuli, including growth factors and different cytokines (Rao 2001). Cell viability analysis revealed an increased sensitivity of M0 and M2-like macrophages against MEKi, while M1-like macrophages showed a low sensitivity to MEKi-induced cell death. ERK1/2 signaling has been shown to be essential for macrophage development, since MCSF-dependent ERK1/2 activation promotes proliferation of bone marrow-derived progenitors for macrophage production (Richardson et al. 2015). This results might explain the high sensitivity of M0 macrophages in the abovementioned cell viability experiments, since the M0 macrophages have been cultivated in M-CSF containing medium. Furthermore, ERK1/2 signaling is associated with M2-like macrophage polarization. It was shown that ROS-mediated ERK activation specifically affected M2-like, but not M1-like macrophage polarization in primary human monocytes. ERK inhibition blocked the expression of M2-associated protein CD163 and M2-associated cytokines CCL17, CCL18 and CCL24, while only minimaly affecting pro-inflammatory protein and cytokine expression (Zhang et al. 2013). In addition to playing a role in M2-like macrophage polarization, ERK1/2 signaling has also been associated with pro-inflammatory M1-like macrophage polarization, where LPS-induced ERK1/2 activation in GM-CSF differentiated macrophages through TLR-4, highlighting the context-dependent influence of ERK1/2 signaling on macrophage phenotype (Biswas and Mantovani 2010).

Besides cell viability, MEKi affected cellular metabolism by decreasing OCR in M2-like macrophages *in vitro*. ERK1/2 signaling has been shown to regulate cellular metabolism in human alveolar

macrophages by controlling ATP production and mitochondrial integrity. In this study, inhibition of ERK activity resulted in mitochondrial dysfunction by inducing loss of mitochondrial transmembrane potential, thereby promoting cell death (Monick et al. 2008). Another study revealed that LPS-induced ERK1/2 activation in murine RAW 264.7 cells promoted glucose consumption, glycolytic flux, lactate production and pentose phosphate pathway, indicating that regulation of cellular metabolism by ERK1/2 signaling might be context-dependent (Traves et al. 2012). However, direct comparison of the studies regarding the role of ERK1/2 signaling in macrophage metabolism should be done cautiously, since the investigated macrophages were derived from different ontogenic origin and species and it was shown that MAPK activation can differ between macrophages originating from different compartments (Rao 2001).

Tumor-Associated Macrophages Show Pro- and Anti-Inflammatory Phenotypes

The M1-M2 macrophage dichotomy is likely oversimplified and does not reflect the plethora of polarization states that can be observed *in vivo*, e.g. in solid tumors. Transcriptomic analysis stratified PDAC into different tumor subtypes, which differed in clinical outcomes and therapeutic responses (Collisson et al. 2011).However, until now it is unknown how different tumor subtypes influence the polarization of tumor-associated macrophages. To investigate this, we polarized macrophages with conditioned-medium from different epithelial and mesenchymal PDAC tumor cell lines to generate epithelial and mesenchymal TCM-stimulated macrophages (epiTAMs and mesTAMs) and performed immunophenotypic characterization based on transcriptomics and marker protein expression *in vitro*. Characterization of tumor-associated macrophages (TAMs) on the transcriptomic level revealed a closer clustering of TAMs with M0 and M2-like macrophages than with M1-like macrophages. This result was in accordance with recent findings, showing that TAMs shared phenotypical and functional features with an anti-inflammatory M2-like macrophage polarization state (Cheung et al. 2018; Hsieh, Tai, and Yang 2018; Tariq et al. 2017).

Furthermore, gene expression analysis by qRT-PCR revealed an upregulation of pro- and anti-inflammatory genes in epiTAMs and mesTAMs, indicating that TAMs were not exclusively characterized by the expression of anti-inflammatory genes, but rather showed a phenotype consistent of both pro- and anti-inflammatory marker genes. In accordance with this, flow cytometry revealed that murine TAMs were characterized by an increased protein expression of anti-inflammatory CD206 and pro-inflammatory CD80 following TCM stimulation *in vitro*, further supporting the existence of TAM phenotypes, which not exclusively expressed anti-inflammatory genes. Even though TAMs are often referred to be M2-like, TAMs were shown to exhibit pro- and

anti-inflammatory properties in PDAC (Helm et al. 2014). Helm et al. phenotypically characterized freshly isolated human PDAC TAMs and showed that TAMs expressed both pro-inflammatory HLA-DR, IL-1β and TNF-α and anti-inflammatory CD163 and IL-10 proteins and contributed to EMT induction in PDAC cells. Furthermore, direct co-culture of human TAMs with HER2-positive breast cancer and lymphoma cell lines resulted in increased gene expression of anti-inflammatory IL-10 and CD206 with concomitant upregulation of pro-inflammatory Il-6 and iNOS genes (Benner et al. 2019). In our study, flow cytometric observation obtained in murine TAMs could be validated in human TAMs *in vitro*, which also showed concomitant expression of pro- and anti-inflammatory proteins, e.g. CD206 and CD86. However, the applied marker protein panels were not able to separate epiTAMs and mesTAMs both in mouse and human model, highlighting the difficulty to determine a tumor subtype-specific macrophage polarization state in a continuum of highly plastic polarization states based on a limited amount of marker proteins.

Tumor-Conditioned Medium Stimulation Increases OXPHOS in Tumor-Associated Macrophages

Immune cell activation is associated with distinct metabolic adaptations, which impact cellular functions and phenotypes. In tumors, macrophages undergo metabolic reprogramming, which can subsequently contribute to cancer progression by supporting their pro-tumorigenic properties (Penny et al. 2016). Liu et al. reported that tumor extract-stimulated macrophages showed an increased glycolysis and expression of glycolytic proteins following stimulation. Importantly, the authors observed a mixed M1/M2 phenotype of TAMs with pro-inflammatory cytokine expression, while concomitantly expressing ARG1, IL4Rα and PLIN2 (Liu et al. 2017). Another study revealed that human macrophages co-cultured with thyroid carcinoma cells showed increased pro-inflammatory cytokine expression and glycolysis, which was mediated by tumor-derived lactate (Arts et al. 2016). The tumor microenvironment has been frequently shown to be enriched for lactic acid, which polarizes TAMs by induction of HIF1A (Colegio et al. 2014). In general, HIF1A signaling in TAMs has been associated with a glycolytic TAM phenotype (Wang et al. 2017). However, in our study we observed an induction of HIF1A downstream target genes on the transcriptional level in TAMs, while TAMs showed a decreased glycolysis. These results might be explained by the different measurement time points of HIF1A signaling and metabolic flux assays. While HIF1A signaling was examined 6 h after TCM stimulation, the metabolic flux assays were investigated after 48 h of TCM induction. In pancreatic cancer, human TAMs showed an increased aerobic glycolysis which was associated with invasion and metastasis (Penny et al. 2016). In this study, the authors compared human TAMs, which were cultivated with tumor-conditioned medium from human PDAC cell lines, with macrophages

cultured in normal pancreatic cell medium and revealed that TAMs had a prominent glycolytic signature on the transcriptional and metabolic flux level. Additionally, TAMs increased epithelial-mesenchymal transition and promoted tumor metastasis.

In comparison to the aforementioned studies, the results of this work demonstrated that TAMs showed an increased oxidative phosphorylation and a decreased glycolysis following TCM stimulation. Importantly, glucose concentration measurement of TCM and TCM incubated for different time points on TAMs revealed that glucose was present in TCM and that glucose concentrations remained constant during incubation with TAMs, indicating that TAMs preferentially used OXPHOS for energy production. The contradictory results between this and the abovementioned studies might be explained by differences between human and murine macrophages investigated in the respective studies. Furthermore, Liu et al. investigated glycolytic changes following tumor extract stimulation in murine tumor-associated macrophages mostly on the transcriptomic level and only sparsely on the protein level. Therefore, we can not exclude the possibility that changes on the transcriptomic and protein level of a few selected proteins might not be translated to changes in the metabolic flux (Liu et al. 2017).

Investigation of Functional Differences in Tumor-Associated Macrophages

In immunology, macrophage activation states have been conventionally determined based on expression of specific inflammatory marker proteins. In the context of tumor biology, macrophages have been considered to be pro-tumorigenic when expressing high levels of, e.g. CD206, CD163 and ARG1, while being anti-tumorigenic when expressing high levels of, e.g. NOS2, TNF and MHC molecules. If the expression of a marker protein changed, e.g. after cellular stimulation or treatment, it was assumed that macrophages underwent a repolarization from an anti-inflammatory towards a pro-inflammatory phenotype or vice versa (Firouzi-Amandi et al. 2018). However, macrophage polarization states represent a continuum, which makes the exclusive application of marker proteins to dissect cellular functional state delicate and results solely based on protein marker changes should be interpreted cautiously. Therefore, we investigated additionally on cellular processes that might impact TAM function tumor subtype-specifically by focusing on biological processes shown to be differentially enriched between epiTAMs and mesTAMs from RNAseq. Comparison of tumor subtype-specific gene expression in epiTAMs and mesTAMs identified differentially expressed genes, which were enriched in gene sets associated with inflammatory response via IFNγ as well as with hypoxia.

In general, IFNγ is reported to contribute to tumor immune surveillance by direct and indirect mechanisms on tumor cells. IFNγ directly elicited cPLA2-dependent autophagy-associated apoptosis through reactive oxygen species (ROS) induction in colorectal cancer cells (Wang et al. 2018). In TAMs, IFNγ has been shown to induce nitric oxide production, resulting in increased tumor cell lysis and promoting tumor elimination (Spear et al. 2012).

Furthermore, IFNγ induced epithelial-mesenchymal transition in human papillary thyroid cancer cells and induced expression of immune checkpoint molecules CTLA-4 and PD-L1 on tumor cells, contributing to inhibition of an effective anti-tumor T cell response (Lv et al. 2015; Mo et al. 2018; Zou, Wolchok, and Chen 2016).

Despite an enrichment in IFNγ signaling response in epiTAMs, IFNγ secretion by epithelial tumor cells and epiTAMs could not be validated at the protein level. A possible explanation for this observation could be that the amount of cells used in the experiments was insufficient to produce and secrete detectable levels of this extremely potent cytokine. Furthermore, it was shown that IFNγ release was significantly lower in cells cultured with FCS-supplemented medium in comparison to serum-free cell culture medium, potentially contributing to the observed ELISA results (Silberer, Ihorst, and Kopp 2008). However, whether IFNγ signaling is differentially regulated between epiTAMs and mesTAMs has to be further investigated. To examine this, one could investigate the expression level of known IFNγ targets, e.g. interferon regulatory factor 1 (IRF1) and IRF8, by qRT-PCR and by western blot (Dror et al. 2007).

In comparison to epiTAMs, mesTAMs were enriched in a gene set associated with hypoxia. Hypoxia is a common feature of advanced tumors and is the result of aberrant tumor vascularization and insufficient blood supply (Pouyssegur, Dayan, and Mazure 2006). The hypoxic response is, in part, mediated by hypoxia-inducible factor 1α (HIF1A) signaling, which promotes metabolic adaptation of tumor and immune cells, e.g. by increasing glycolytic rates (Wang et al. 2017). However, HIF1A signaling is not exclusively restricted to hypoxia, but can also be induced under normoxic conditions by a variety of microenvironmental cues, e.g. lactic acid and pyruvate (Colegio et al. 2014; Jung et al. 2011). In TAMs, lactic acid was reported to promote the induction of an immunosuppressive TAM phenotype by increasing the expression of *Arg1* and *Vegfa* in a HIF1A-dependent manner (Colegio et al. 2014). Since mesenchymal PDAC tumors were shown to be strongly associated with glycolysis and lactic acid production, we wanted to investigate whether mesenchymal tumor cells can induce an immunosuppressive mesTAM phenotype in a HIF1A-dependent manner (Daemen et al. 2015). Surprisingly, and contradictory to the GSEA results, western blot analysis revealed an increased HIF1A protein level in epiTAMs following TCM stimulation, while HIF1A levels in mesTAMs remained largely unchanged after TCM stimulation. Importantly, gene expression analysis revealed an

upregulation of HIF1A target genes on the transcriptional level in epiTAMs and mesTAMs following TCM stimulation. However, HIF1A signaling activity in TAMs was not related to a specific PDAC tumor subtype, since HIF1A target genes were upregulated in both epiTAMs and mesTAMs

The discrepancy between GSEA and western blot results might be explained by the different duration of TCM stimulation between the experiments, since HIF1A signaling is a tightly regulated process with distinct kinetics. Under hypoxic conditions, HIF1A was transiently stabilized after 6 h-8 h, while the protein level almost declined to baseline levels after 12 h of hypoxia (Nguyen et al. 2013). Under normoxia, HIF1A protein stability was increased within the first 24 h after respective stimulation. It was shown that Oncostatin M upregulated HIF1A in breast cancer TAMs oxygen concentration-independently, showing the highest accumulation after 24 h, while declining to baseline levels after 48 h of treatment (Shrivastava et al. 2018). Besides solely focusing on the transcriptional level of HIF1A target genes, one could also investigate target gene expression on the protein level by western blot. Furthermore, secreted HIF1A target proteins, e.g. VEGFA, could be examined by ELISA.

In addition to IFNγ and HIF1A, RNAseq revealed differences in gene sets associated with cholesterol metabolism and recently, Goossens et al. provided evidence that ovarian cancer cells promoted membrane cholesterol efflux in macrophages by secretion of hyaluronic acid. Cholesterol efflux depleted lipid rafts in macrophages and resulted in macrophage reprogramming towards an immunosuppressive phenotype by promoting anti-inflammatory IL-4 signaling, (Goossens et al. 2019). However, whether cholesterol metabolism was affected in epiTAMs by epithelial PDAC cells and whether this potential changes in cholesterol metabolism result in phenotypic differences promoting tumor progression need to be further investigated.

Outlook

IFNγ and HIF1A signaling were not associated with a specific TAM subtype. However, leading edge analysis of the RNAseq data from epiTAMs and mesTAMs revealed that leading edge genes were associated with MAPK signaling and mesTAMs. Murine mesTAMs were more sensitive to MEK inhibitor-induced cell death at higher MEK inhibitor concentrations than epiTAMs. Importantly, the same trend was observed in human mesTAMs and primary resected PDAC revealed an increased pERK signal in the microenvironment of mesenchymal tumor areas, which partially co-localized with $CD68^{+}$ macrophages. Future work should focus on the identification of functional differences between epiTAMs and mesTAMs, since the results of this work are descriptive to date. It would be interesting to investigate potential differences in the cytokine profile of epiTAMs and mesTAMs by performing a cytokine array. Importantly, MAPK signaling has previously been shown to regulate

cytokine expression in macrophages and our RNAseq data revealed an increased gene expression of *Ccl17* and *Ccl22*, which have been associated with an accumulation of regulatory T cells in gastric cancer (Lim et al. 2014; Mizukami et al. 2008). Furthermore, co-culture experiments with epiTAMs or mesTAMs and different immune cell types, e.g. T cells and dendritic cells could be performed to investigate potential differences of epiTAM- or mesTAM-related immune activation or repression. To identify tumor-derived factors, which might be responsible for the differences in MAPK pathway dependency of epiTAMs and mesTAMs, one could perform a cytokine array of tumor-conditioned medium of different epithelial and mesenchymal PDAC cell lines In addition to studying this, it is also interesting to focus more on the tumor subtype-specific TAM heterogeneity. To investigate tumor subtype-specific TAM heterogeneity, one could establish a patient-derived xenograft cohort from PDAC patients, whereby transplanted tumors subsequently could be analyzed by RNAseq for their respective tumor subtype. In addition to characterizing the tumor subtype, RNAseq data could also be used for a deconvolution to investigate differences in the murine tumor-infiltrating immune cells and the activation states of particular cells, e.g. TAMs. Furthermore, formalin-fixed paraffin-embedded tissue sections of known PDAC tumor subtypes could be analyzed by Digital Spatial Imaging (DSP) to assess the heterogeneity of proteins and RNAs of PDAC tumor cells and their surrounding microenvironmental cells, including macrophages in a multiplexed manner, while concomitantly preserving the morphological context.

Conclusion & Study Limitations

In the past, MEK inhibitors were investigated in different tumor entities as a therapeutic treatment option, focusing mainly on the effects of MEK inhibition on tumor cells. However, it is also important to investigate the effects of MEK inhibition on other cells present in the tumor bulk, e.g. infiltrating immune cells. In this work, we aimed at investigating the effects of MEK inhibition on the PDAC tumor microenvironment with particular focus on tumor-associated macrophages. Importantly, MEKi treatment decreased macrophages and the M2-like macrophage marker CD206. Based on our previous data, we assumed that the majority of macrophages inside the tumor microenvironment consisted of M2-like macrophages, which were characterized by the expression of CD206. However, MEKi treatment of genetic mouse model of spontaneous PDAC, *CKP*, revealed that a population of macrophages remained, which were CD206 negative. Based on this finding, we assumed the existence of a TAM heterogeneity. To investigate a potential tumor subtype-specific macrophage polarization, macrophages were stimulated with tumor-conditioned medium from the different tumor subtypes, epithelial and mesenchymal, *in vitro* to generate epiTAMs and mesTAMs. epiTAMs and mesTAMs could not be distinguished from each other based on marker protein expression,

however, epiTAMs and mesTAMs showed a difference in MEK inhibitor sensitivity. This result demonstrated that the effects of MEK inhibitor treatment should be considered not only on malignant tumor cells, but also on other cell types in the tumor stroma, which may also show different responses to the treatment. Taken together, the present study provided evidence that 1) MEK inhibition depletes M2-like macrophages from PDAC tumor microenvironment 2) Tumor-associated macrophages display phenotypes which are distinct from the classically-defined M1 and M2 macrophage phenotypes 3) Tumor-associated macrophages show a tumor subtype specific MEKi sensitivity. Despite new insights provided, there are several limitations, which have to be taken into consideration when interpreting and integrating these results into the existing data in immune-oncological landscape.

First, immediate and sustained MEK inhibition in *CKP* mice was achieved by application of two different MEK inhibitors, namely trametinib for the short-term treatment and refametinib for the long-term treatment. *In vitro* studies revealed differences in the sensitivity of low-grade serous ovarian cancer cell lines (LGSC) to different MEK inhibitors, including refametinib and trametinib (Fernández et al. 2016). Fernández et al. showed that different MEK inhibitors possessed different IC_{50} values in LGSC cell lines and showed that the MEK inhibitors differed in their efficacy to block ERK1/2 phosphorylation and cell proliferation. This results have to be taken into consideration when directly comparing the immunohistochemical results between immediate and sustained treatment, since differences in pathway inhibition efficacy might result in differences in MAPK pathway activity between different MEK inhibitors.

Second, the *in vitro* investigated macrophage heterogeneity does not completely reflect the full spectrum of intratumoral macrophage heterogeneity present *in vivo*. TAM polarization was achieved by tumor-conditioned medium, however, *in vivo* direct cell-cell interactions between macrophages and tumor cells, has been shown to contribute to TAM polarization (Barclay and Brown 2006; Takenaka et al. 2007). Furthermore, macrophage and non-tumor cell interactions were not addressed in the above experiments, since also other non-tumor cell macrophage interactions, e.g. cancer-associated fibroblasts (CAFs) have been shown to promote anti-inflammatory macrophage polarization in PDAC, adding another layer of interaction important for driving macrophage polarization status (A. Zhang et al. 2017).

Third, TAMs in PDAC were shown to be derived from different ontogenic backgrounds. While tissue-resident TAMs were derived from an embryonic origin and expanded through *in situ* proliferation during PDAC progression, the majority of TAMs was derived from hematopoietic stem cell-derived monocytes (Zhu et al. 2017). Importantly, the heterogeneity of TAM origin could be linked to differences in TAM function with monocyte-derived TAMs showing prominent role in antigen-

presentation, while tissue-resident TAMs revealed a transcriptional profile associated with shaping of fibrotic response.

Fourth, a limited the number of murine epithelial and mesenchymal tumor cell lines was used to determine tumor subtype-specific effects on TAM polarization. For generalization of tumor subtype-specific influences on TAM polarization, a higher number of epithelial and mesenchymal tumor cells should be used to generate a higher number of different epiTAMs and mesTAMs. Furthermore, polarization of TAMs with conditioned-medium from patient-derived xenograft (PDX) would give an additional layer of information, since PDX tumor cells were reported to represent the heterogeneity and complexity of malignant diseases more accurately than commercial tumor cell lines, which have been cultivated for longer times and underwent adaptation under cell culture conditions (Collins and Lang 2018).

Fifth, the MEK inhibitor concentration used in the *in vitro* experiments to investigate, e.g. marker protein expression changes, was 10nM. This concentration was selected, since it was below the $subIC_{50}$ concentration of the most sensitive investigated macrophage subset and the same concentration was used to treat M0, M1-like and M2-like macrophages. A more appropriate experimental condition would be to use, for example, an IC_{20} specific for each macrophage subset to have the same MEKi influence in each macrophage subset.

Last but not least, the protein marker panel applied in this study to investigate tumor subtype-specific marker expression on TAMs was limited to 4-6 markers. Other studies examined intratumoral macrophage heterogeneity by using mass cytometry (CyTOF) applying an antibody panel targeting multiple marker proteins or single cell RNAseq (scRNAseq) in lung adenocarcinoma and clear cell renal cell carcinoma (Chevrier et al. 2017; Lavin et al. 2017).

Future studies are needed to translate the new insights in tumor-associated macrophage biology of PDAC to clinical application. Hopefully, the novel insights provided by this study will contribute to construction of an effective treatment for pancreatic cancer patients in the future

Literature

Aichler, Michaela et al. 2012. “Origin of Pancreatic Ductal Adenocarcinoma from Atypical Flat Lesions: A Comparative Study in Transgenic Mice and Human Tissues.” *Journal of Pathology*.

Allard, Benoit, Alice Panariti, and James G. Martin. 2018. “Alveolar Macrophages in the Resolution of Inflammation, Tissue Repair, and Tolerance to Infection.” *Frontiers in immunology*.

Angell, Trevor E. et al. 2016. “Circulating Myeloid-Derived Suppressor Cells Predict Differentiated Thyroid Cancer Diagnosis and Extent.” *Thyroid*.

Apte, M. V. et al. 2004. “Desmoplastic Reaction in Pancreatic Cancer: Role of Pancreatic Stellate Cells.” *Pancreas*.

Ardito, Christine M et al. 2012. “EGF Receptor Is Required for KRAS-Induced Pancreatic Tumorigenesis.” *Cancer cell* 22(3): 304–17.

Arihara, Fumitaka et al. 2013. “Increase in CD14+HLA-DR-/Low Myeloid-Derived Suppressor Cells in Hepatocellular Carcinoma Patients and Its Impact on Prognosis.” *Cancer Immunology, Immunotherapy*.

Arts, Rob J.W. et al. 2016. “Transcriptional and Metabolic Reprogramming Induce an Inflammatory Phenotype in Non-Medullary Thyroid Carcinoma-Induced Macrophages.” *OncoImmunology*.

Bailey, Peter et al. 2016. “Genomic Analyses Identify Molecular Subtypes of Pancreatic Cancer.” *Nature*.

Bain, Calum C., and Anika Schridde. 2018. “Origin, Differentiation, and Function of Intestinal Macrophages.” *Frontiers in Immunology*.

Barclay, A. Neil, and Marion H. Brown. 2006. “The SIRP Family of Receptors and Immune Regulation.” *Nature Reviews Immunology*.

Bardeesy, Nabeel, and Ronald A. DePinho. 2002. “Pancreatic Cancer Biology and Genetics.” *Nature Reviews Cancer*.

Bardi, Gina T., Mary Ann Smith, and Joshua L. Hood. 2018. “Melanoma Exosomes Promote Mixed M1 and M2 Macrophage Polarization.” *Cytokine*.

Beatty, Gregory L et al. 2013. “A Phase I Study of an Agonist CD40 Monoclonal Antibody (CP-870,893) in Combination with Gemcitabine in Patients with Advanced Pancreatic Ductal Adenocarcinoma.” *Clinical cancer research : an official journal of the American Association for Cancer Research* 19(22): 6286–95.

Benner, Brooke et al. 2019. “Generation of Monocyte-Derived Tumor-Associated Macrophages Using Tumor-Conditioned Media Provides a Novel Method to Study Tumor-Associated Macrophages in Vitro.” *Journal for ImmunoTherapy of Cancer*.

Bhatia, Shikha et al. 2011. “Rapid Host Defense against Aspergillus Fumigatus Involves Alveolar Macrophages with a Predominance of Alternatively Activated Phenotype.” *PLoS ONE*.

Biswas, Subhra K., and Alberto Mantovani. 2010. “Macrophage Plasticity and Interaction with Lymphocyte Subsets: Cancer as a Paradigm.” *Nature Immunology*.

Borges Da Silva, Henrique et al. 2015. “Splenic Macrophage Subsets and Their Function during Blood-Borne Infections.” *Frontiers in Immunology*.

Van den Bossche, Jan, Jeroen Baardman, and Menno P.J. de Winther. 2015. “Metabolic Characterization of Polarized M1 and M2 Bone Marrow-Derived Macrophages Using Real-Time Extracellular Flux Analysis.” *Journal of Visualized Experiments*.

Candido, Juliana B. et al. 2018. “CSF1R+ Macrophages Sustain Pancreatic Tumor Growth through T Cell Suppression and Maintenance of Key Gene Programs That Define the Squamous Subtype.” *Cell Reports*.

Cekay, Michael John et al. 2017. “Smac Mimetics and Type II Interferon Synergistically Induce Necroptosis in Various Cancer Cell Lines.” *Cancer Letters*.

El Chartouni, Carol, Lucia Schwarzfischer, and Michael Rehli. 2010. “Interleukin-4 Induced Interferon Regulatory Factor (Irf) 4 Participates in the Regulation of Alternative Macrophage Priming.” *Immunobiology*.

Cheung, Phyllis F. et al. 2018. “Notch-Induced Myeloid Reprogramming in Spontaneous Pancreatic Ductal Adenocarcinoma by Dual Genetic Targeting.” *Cancer Research*.

Chevrier, Stéphane et al. 2017. “An Immune Atlas of Clear Cell Renal Cell Carcinoma.” *Cell*.

Chu, Gerald C., Alec C. Kimmelman, Aram F. Hezel, and Ronald A. DePinho. 2007. “Stromal Biology of Pancreatic Cancer.” *Journal of Cellular Biochemistry*.

Clark, Carolyn E. et al. 2007. “Dynamics of the Immune Reaction to Pancreatic Cancer from Inception to Invasion.” *Cancer Research*.

Clayton, Kalum et al. 2017. “Langerhans Cells-Programmed by the Epidermis.” *Frontiers in Immunology*.

Colegio, Oscar R. et al. 2014. “Functional Polarization of Tumour-Associated Macrophages by Tumour-Derived Lactic Acid.” *Nature*.

Collins, Anne T., and Shona H. Lang. 2018. “A Systematic Review of the Validity of Patient Derived Xenograft (PDX) Models: The Implications for Translational Research and Personalised Medicine.” *PeerJ*.

Collisson, Eric A. et al. 2011. “Subtypes of Pancreatic Ductal Adenocarcinoma and Their Differing Responses to Therapy.” *Nature Medicine*.

Condamine, Thomas et al. 2016. “Lectin-Type Oxidized LDL Receptor-1 Distinguishes Population of Human Polymorphonuclear Myeloid-Derived Suppressor Cells in Cancer Patients.” *Science Immunology*.

Corcoran, Ryan B. et al. 2015. “Combined BRAF and MEK Inhibition with Dabrafenib and Trametinib in BRAF V600-Mutant Colorectal Cancer.” In *Journal of Clinical Oncology*,.

Curiel, Tyler J. et al. 2004. “Specific Recruitment of Regulatory T Cells in Ovarian Carcinoma Fosters Immune Privilege and Predicts Reduced Survival.” *Nature Medicine*.

Daemen, Anneleen et al. 2015. “Metabolite Profiling Stratifies Pancreatic Ductal Adenocarcinomas into Subtypes with Distinct Sensitivities to Metabolic Inhibitors.” *Proceedings of the National Academy of Sciences of the United States of America*.

Darnell, James E., Ian M. Kerr, and George R. Stark. 1994. “Jak-STAT Pathways and Transcriptional Activation in Response to IFNs and Other Extracellular Signaling Proteins.” *Science*.

DeNardo, David G., and Brian Ruffell. 2019. “Macrophages as Regulators of Tumour Immunity and Immunotherapy.” *Nature Reviews Immunology*.

Diaz-Montero, C. Marcela et al. 2009. “Increased Circulating Myeloid-Derived Suppressor Cells Correlate with Clinical Cancer Stage, Metastatic Tumor Burden, and Doxorubicin-Cyclophosphamide Chemotherapy.” *Cancer Immunology, Immunotherapy*.

Dixon, Laura J. et al. 2013. “Kupffer Cells in the Liver.” *Comprehensive Physiology*.

Dror, Natalie et al. 2007. “Identification of IRF-8 and IRF-1 Target Genes in Activated Macrophages.” *Molecular immunology* 44(4): 338–46.

Ebert, Peter J.R. et al. 2016. “MAP Kinase Inhibition Promotes T Cell and Anti-Tumor Activity in Combination with PD-L1 Checkpoint Blockade.” *Immunity*.

Edlund, Helena. 2002. “Pancreatic Organogenesis - Developmental Mechanisms and Implications for Therapy.” *Nature Reviews Genetics*.

Engblom, Camilla, Christina Pfirschke, and Mikael J. Pittet. 2016. “The Role of Myeloid Cells in Cancer Therapies.” *Nature Reviews Cancer*.

Fernández, Marta Llauradó et al. 2016. “Differences in MEK Inhibitor Efficacy in Molecularly Characterized Low-Grade Serous Ovarian Cancer Cell Lines.” *American Journal of Cancer Research*.

Firouzi-Amandi, Akram et al. 2018. “Chrysin-Nanoencapsulated PLGA-PEG for Macrophage Repolarization: Possible Application in Tissue Regeneration.” *Biomedicine and Pharmacotherapy*.

Freemerman, Alex J. et al. 2014. “Metabolic Reprogramming of Macrophages: Glucose Transporter 1 (GLUT1)-Mediated Glucose Metabolism Drives a Proinflammatory Phenotype.” *Journal of Biological Chemistry*.

Fujioka, S. et al. 2004. “NF- B and AP-1 Connection: Mechanism of NF- B-Dependent Regulation of AP-1 Activity.” *Molecular and Cellular Biology*.

Gabrilovich, Dmitry I. et al. 2007. “The Terminology Issue for Myeloid-Derived Suppressor Cells [1].” *Cancer Research*.

Gabrilovich, Dmitry I., and Srinivas Nagaraj. 2009. “Myeloid-Derived Suppressor Cells as Regulators of the Immune System.” *Nature Reviews Immunology*.

Gabrilovich, Dmitry I., Suzanne Ostrand-Rosenberg, and Vincenzo Bronte. 2012. “Coordinated Regulation of Myeloid Cells by Tumours.” *Nature Reviews Immunology*.

Gardian, Katarzyna, Sława Janczewska, Waldemar L. Olszewski, and Marek Durlik. 2012. “Analysis of Pancreatic Cancer Microenvironment: Role of Macrophage in-Filtrates and Growth Factors Expression.” *Journal of Cancer*.

Geiger, Roger et al. 2016. “L-Arginine Modulates T Cell Metabolism and Enhances Survival and Anti-Tumor Activity.” *Cell*.

Ginhoux, Florent et al. 2010. “Fate Mapping Analysis Reveals That Adult Microglia Derive from Primitive Macrophages.” *Science*.

Goossens, Pieter et al. 2019. “Membrane Cholesterol Efflux Drives Tumor-Associated Macrophage Reprogramming and Tumor Progression.” *Cell Metabolism*.

Gordon, Siamon. 2003. “Alternative Activation of Macrophages.” *Nature reviews. Immunology* 3(1): 23–35.

Gordon, Siamon, and Philip R. Taylor. 2005. “Monocyte and Macrophage Heterogeneity.” *Nature Reviews Immunology*.

Gosse, Stéphanie Gobert et al. 2005. “M-CSF Stimulated Differentiation Requires Persistent MEK Activity and MAPK Phosphorylation Independent of Grb2-Sos Association and Phosphatidylinositol 3-Kinase Activity.” *Cellular Signalling*.

Gray, Elizabeth E., and Jason G. Cyster. 2012. “Lymph Node Macrophages.” *Journal of Innate Immunity*.

Guilliams, Martin et al. 2013. “Alveolar Macrophages Develop from Fetal Monocytes That Differentiate into Long-Lived Cells in the First Week of Life via GM-CSF.” *Journal of Experimental Medicine*.

Habbe, Nils et al. 2008. “Spontaneous Induction of Murine Pancreatic Intraepithelial Neoplasia (MPanIN) by Acinar Cell Targeting of Oncogenic Kras in Adult Mice.” *Proceedings of the National Academy of Sciences of the United States of America*.

Helm, Ole et al. 2014. “Tumor-Associated Macrophages Exhibit pro- and Anti-Inflammatory Properties by Which They Impact on Pancreatic Tumorigenesis.” *International Journal of Cancer*.

Hezel, Aram F et al. 2006. “Genetics and Biology of Pancreatic Ductal Adenocarcinoma.” *Genes & development* 20(10): 1218–49.

Hidalgo, Manuel. 2010. “Pancreatic Cancer.” *The New England journal of medicine* 362(17): 1605–17.

Hoeffel, Guillaume et al. 2012. “Adult Langerhans Cells Derive Predominantly from Embryonic Fetal Liver Monocytes with a Minor Contribution of Yolk Sac-Derived Macrophages.” *Journal of Experimental Medicine*.

Hsieh, Chia Hsin, Shyh Kuan Tai, and Muh Hwa Yang. 2018. “Snail-Overexpressing Cancer Cells Promote M2-Like Polarization of Tumor-Associated Macrophages by Delivering MiR-21-Abundant Exosomes.” *Neoplasia (United States)*.

Huang, Yu-Kuan et al. 2019. “Macrophage Spatial Heterogeneity in Gastric Cancer Defined by Multiplex Immunohistochemistry.” *Nature communications* 10(1): 3928.

Infante, Jeffrey R. et al. 2014. “A Randomised, Double-Blind, Placebo-Controlled Trial of Trametinib, an Oral MEK Inhibitor, in Combination with Gemcitabine for Patients with Untreated Metastatic Adenocarcinoma of the Pancreas.” *European Journal of Cancer*.

Ip, W. K.Eddie et al. 2017. “Anti-Inflammatory Effect of IL-10 Mediated by Metabolic Reprogramming of Macrophages.” *Science*.

Jackson, E L et al. 2001. “Analysis of Lung Tumor Initiation and Progression Using Conditional Expression of Oncogenic K-Ras.” *Genes & development* 15(24): 3243–48.

Jemal, Ahmedin et al. 2008. “Cancer Statistics, 2008.” *Cancer Journal for Clinicians*.

Jung, Seung Youn et al. 2011. “Pyruvate Promotes Tumor Angiogenesis through HIF-1-Dependent PAI-1 Expression.” *International Journal of Oncology*.

Kawane, Kohki et al. 2006. “Chronic Polyarthritis Caused by Mammalian DNA That Escapes from Degradation in Macrophages.” *Nature*.

Kessenbrock, Kai, Vicki Plaks, and Zena Werb. 2010. “Matrix Metalloproteinases: Regulators of the Tumor Microenvironment.” *Cell*.

Klug, Felix et al. 2013. “Low-Dose Irradiation Programs Macrophage Differentiation to an INOS+/M1 Phenotype That Orchestrates Effective T Cell Immunotherapy.” *Cancer Cell*.

Koster, Johannes, and Sven Rahmann. 2018. “Snakemake-a Scalable Bioinformatics Workflow Engine.” *Bioinformatics (Oxford, England)* 34(20): 3600.

Kryczek, Ilona et al. 2006. “B7-H4 Expression Identifies a Novel Suppressive Macrophage Population in Human Ovarian Carcinoma.” *Journal of Experimental Medicine*.

Kuang, Dong Ming et al. 2009. “Activated Monocytes in Peritumoral Stroma of Hepatocellular Carcinoma Foster Immune Privilege and Disease Progression through PD-L1.” *Journal of Experimental Medicine*.

Kumar, Vinit et al. 2016. “CD45 Phosphatase Inhibits STAT3 Transcription Factor Activity in Myeloid Cells and Promotes Tumor-Associated Macrophage Differentiation.” *Immunity*.

Kusmartsev, Sergei, and Dmitry I. Gabrilovich. 2005. “STAT1 Signaling Regulates Tumor-Associated Macrophage-Mediated T Cell Deletion.” *The Journal of Immunology*.

Van Laethem, Jean-Luc et al. 2017. “Phase I/II Study of Refametinib (BAY 86-9766) in Combination with Gemcitabine in Advanced Pancreatic Cancer.” *Targeted oncology* 12(1): 97–109.

Lavin, Yonit et al. 2017. “Innate Immune Landscape in Early Lung Adenocarcinoma by Paired Single-Cell Analyses.” *Cell*.

Lawrence, Toby, and Gioacchino Natoli. 2011. “Transcriptional Regulation of Macrophage Polarization: Enabling Diversity with Identity.” *Nature Reviews Immunology*.

Li, Jing et al. 2018. “Co-Inhibitory Molecule B7 Superfamily Member 1 Expressed by Tumor-Infiltrating Myeloid Cells Induces Dysfunction of Anti-Tumor CD8+ T Cells.” *Immunity*.

Lim, Mei Xing et al. 2014. “Differential Regulation of Proinflammatory Cytokine Expression by Mitogen-Activated Protein Kinases in Macrophages in Response to Intestinal Parasite Infection.” *Infection and immunity* 82(11): 4789–4801.

Lin, Heng et al. 2018. “Host Expression of PD-L1 Determines Efficacy of PD-L1 Pathway Blockade–Mediated Tumor Regression.” *Journal of Clinical Investigation*.

Liu, Di et al. 2017. “Comprehensive Proteomics Analysis Reveals Metabolic Reprogramming of Tumor-Associated Macrophages Stimulated by the Tumor Microenvironment.” *Journal of Proteome Research*.

Lv, Nannan et al. 2015. "Inflammatory mediators, tumor necrosis factor-α and interferon-γ, induce EMT in human PTC cell lines." *Oncol Lett*. 10(4): 2591-2597.

Ma, Yuting et al. 2013. “Anticancer Chemotherapy-Induced Intratumoral Recruitment and Differentiation of Antigen-Presenting Cells.” *Immunity*.

Marigo, Ilaria et al. 2016. “T Cell Cancer Therapy Requires CD40-CD40L Activation of Tumor Necrosis Factor and Inducible Nitric-Oxide-Synthase-Producing Dendritic Cells.” *Cancer Cell*.

Marino, S et al. 2000. “Induction of Medulloblastomas in P53-Null Mutant Mice by Somatic Inactivation of Rb in the External Granular Layer Cells of the Cerebellum.” *Genes & development* 14(8): 994–1004.

Martinelli, Paola et al. 2017. “GATA6 Regulates EMT and Tumour Dissemination, and Is a Marker of Response to Adjuvant Chemotherapy in Pancreatic Cancer.” *Gut* 66(9): 1665–76.

Martinez, Fernando O., and Siamon Gordon. 2014. “The M1 and M2 Paradigm of Macrophage Activation: Time for Reassessment.” *F1000Prime Reports*.

Maurer, Carlo et al. 2019. “Experimental Microdissection Enables Functional Harmonisation of Pancreatic Cancer Subtypes.” *Gut*.

Mazur, Pawel K., and Jens T. Siveke. 2012. “Genetically Engineered Mouse Models of Pancreatic Cancer: Unravelling Tumour Biology and Progressing Translational Oncology.” *Gut*.

Mazur, Pawel K et al. 2015. “Combined Inhibition of BET Family Proteins and Histone Deacetylases as a Potential Epigenetics-Based Therapy for Pancreatic Ductal Adenocarcinoma.” *Nature medicine* 21(10): 1163–71.

McGrath, Kathleen E., Anne D. Koniski, Jeffrey Malik, and James Palis. 2003. “Circulation Is Established in a Stepwise Pattern in the Mammalian Embryo.” *Blood*.

McGuigan, Andrew et al. 2018. “Pancreatic Cancer: A Review of Clinical Diagnosis, Epidemiology, Treatment and Outcomes.” *World Journal of Gastroenterology*.

Mitchem, Jonathan B. et al. 2013. “Targeting Tumor-Infiltrating Macrophages Decreases Tumor-Initiating Cells, Relieves Immunosuppression, and Improves Chemotherapeutic Responses.” *Cancer Research*.

Mizukami, Yoshiki et al. 2008. “CCL17 and CCL22 Chemokines within Tumor Microenvironment Are Related to Accumulation of Foxp3+ Regulatory T Cells in Gastric Cancer.” *International journal of cancer* 122(10): 2286–93.

Mo, Xuan et al. 2018. “Interferon-γ Signaling in Melanocytes and Melanoma Cells Regulates Expression of CTLA-4.” *Cancer Research*.

Moffitt, Richard A. et al. 2015. “Virtual Microdissection Identifies Distinct Tumor- and Stroma-Specific Subtypes of Pancreatic Ductal Adenocarcinoma.” *Nature Genetics*.

Monick, Martha M. et al. 2008. “Constitutive ERK MAPK Activity Regulates Macrophage ATP Production and Mitochondrial Integrity.” *The Journal of Immunology*.

Morris IV, John P. et al. 2010. “β-Catenin Blocks Kras-Dependent Reprogramming of Acini into Pancreatic Cancer Precursor Lesions in Mice.” *Journal of Clinical Investigation*.

Morris, John P., Sam C. Wang, and Matthias Hebrok. 2010. “KRAS, Hedgehog, Wnt and the Twisted Developmental Biology of Pancreatic Ductal Adenocarcinoma.” *Nature Reviews Cancer*.

Mosser, David M., and Justin P. Edwards. 2008. “Exploring the Full Spectrum of Macrophage Activation.” *Nature Reviews Immunology*.

Movahedi, Kiavash et al. 2010. “Different Tumor Microenvironments Contain Functionally Distinct Subsets of Macrophages Derived from Ly6C(High) Monocytes.” *Cancer Research*.

Muckenhuber, Alexander et al. 2018. “Pancreatic Ductal Adenocarcinoma Subtyping Using the Biomarkers Hepatocyte Nuclear Factor-1A and Cytokeratin-81 Correlates with Outcome and Treatment Response.” *Clinical cancer research : an official journal of the American Association for Cancer Research* 24(2): 351–59.

Mulkeen, Abby L., Peter S. Yoo, and Charles Cha. 2006. “Less Common Neoplasms of the Pancreas.” *World Journal of Gastroenterology*.

Munder, Markus et al. 2005. “Arginase I Is Constitutively Expressed in Human Granulocytes and Participates in Fungicidal Activity.” *Blood*.

Murphy, Craig A. et al. 2003. “Divergent Pro- and Antiinflammatory Roles for IL-23 and IL-12 in Joint Autoimmune Inflammation.” *Journal of Experimental Medicine*.

Murray, Peter J., and Thomas A. Wynn. 2011. “Protective and Pathogenic Functions of Macrophage Subsets.” *Nature Reviews Immunology*.

Nakhai, Hassan et al. 2007. “Ptf1a Is Essential for the Differentiation of GABAergic and Glycinergic Amacrine Cells and Horizontal Cells in the Mouse Retina.” *Development (Cambridge, England)* 134(6): 1151–60.

Nathan, Carl F., Henry W. Murray, Imichael E. Wlebe, and Berish Y. Rubin. 1983. “Identification of Interferon-γ, as the Lymphokine That Activates Human Macrophage Oxidative Metabolism and Antimicrobial Activity.” *Journal of Experimental Medicine*.

Neamatallah, Thikryat. 2019. “Mitogen-Activated Protein Kinase Pathway: A Critical Regulator in Tumor-Associated Macrophage Polarization.” *Journal of Microscopy and Ultrastructure*.

Nguyen, Lan K. et al. 2013. “A Dynamic Model of the Hypoxia-Inducible Factor 1α(HIF-1α) Network.” *Journal of Cell Science*.

Nielsen, Sebastian R. et al. 2016. “Macrophage-Secreted Granulin Supports Pancreatic Cancer Metastasis by Inducing Liver Fibrosis.” *Nature Cell Biology*.

Noy, Roy, and Jeffrey W. Pollard. 2014. “Tumor-Associated Macrophages: From Mechanisms to Therapy.” *Immunity*.

Nywening, Timothy M. et al. 2018. “Targeting Both Tumour-Associated CXCR2+ Neutrophils and CCR2+ Macrophages Disrupts Myeloid Recruitment and Improves Chemotherapeutic Responses in Pancreatic Ductal Adenocarcinoma.” *Gut*.

Nywening, Timothy M et al. 2016. “Targeting Tumour-Associated Macrophages with CCR2 Inhibition in Combination with FOLFIRINOX in Patients with Borderline Resectable and Locally Advanced Pancreatic Cancer: A Single-Centre, Open-Label, Dose-Finding, Non-Randomised, Phase 1b Trial.” *The Lancet. Oncology* 17(5): 651–62.

Odegaard, Justin I., and Ajay Chawla. 2011. “Alternative Macrophage Activation and Metabolism.” *Annual Review of Pathology: Mechanisms of Disease*.

Olazabal, Isabel María et al. 2008. “Activation Outcomes Induced in Naïve CD8 T-Cells by Macrophages Primed via ‘Phagocytic’ and Nonphagocytic Pathways.” *Molecular Biology of the Cell*.

Olson, Oakley C. et al. 2017. “Tumor-Associated Macrophages Suppress the Cytotoxic Activity of Antimitotic Agents.” *Cell Reports*.

Pan, Fong Cheng, and Chris Wright. 2011. “Pancreas Organogenesis: From Bud to Plexus to Gland.” *Developmental Dynamics*.

Panni, Roheena Z et al. 2019. “Agonism of CD11b Reprograms Innate Immunity to Sensitize Pancreatic Cancer to Immunotherapies.” *Science translational medicine* 11(499).

Paolicelli, Rosa C. et al. 2011. “Synaptic Pruning by Microglia Is Necessary for Normal Brain Development.” *Science*.

Patro, Rob et al. 2017. “Salmon Provides Fast and Bias-Aware Quantification of Transcript Expression.” *Nature methods* 14(4): 417–19.

Pavlou, Sofia, Luxi Wang, Heping Xu, and Mei Chen. 2017. “Higher Phagocytic Activity of Thioglycollate-Elicited Peritoneal Macrophages Is Related to Metabolic Status of the Cells.” *Journal of Inflammation (United Kingdom)*.

Penny, Hweixian Leong et al. 2016. “Warburg Metabolism in Tumor-Conditioned Macrophages Promotes Metastasis in Human Pancreatic Ductal Adenocarcinoma.” *OncoImmunology*.

Pouyssegur, Jacques, Frederic Dayan, and Nathalie M Mazure. 2006. “Hypoxia Signalling in Cancer and Approaches to Enforce Tumour Regression.” *Nature* 441(7092): 437–43.

Prior, Ian A., Paul D. Lewis, and Carla Mattos. 2012. “A Comprehensive Survey of Ras Mutations in Cancer.” *Cancer Research*.

Puleo, Francesco et al. 2018. “Stratification of Pancreatic Ductal Adenocarcinomas Based on Tumor and Microenvironment Features.” *Gastroenterology*.

Pyonteck, Stephanie M. et al. 2013. “CSF-1R Inhibition Alters Macrophage Polarization and Blocks Glioma Progression.” *Nature Medicine*.

Rahib, Lola et al. 2014. “Projecting Cancer Incidence and Deaths to 2030: The Unexpected Burden of Thyroid, Liver, and Pancreas Cancers in the United States.” *Cancer Research*.

Rao, K M. 2001. “MAP Kinase Activation in Macrophages.” *Journal of leukocyte biology*.

Raphael, Benjamin J. et al. 2017. “Integrated Genomic Characterization of Pancreatic Ductal Adenocarcinoma.” *Cancer Cell*.

Ribechini, Eliana et al. 2017. “Novel GM-CSF Signals via IFN-ΓR/IRF-1 and AKT/MTOR License Monocytes for Suppressor Function.” *Blood Advances*.

Richardson, Edward T. et al. 2015. “ERK Signaling Is Essential for Macrophage Development.” *PLoS ONE*.

Ricote, Mercedes et al. 1998. “The Peroxisome Proliferator-Activated Receptor-γ Is a Negative Regulator of Macrophage Activation.” *Nature*.

Ruffell, Brian et al. 2014. “Macrophage IL-10 Blocks CD8+ T Cell-Dependent Responses to Chemotherapy by Suppressing IL-12 Expression in Intratumoral Dendritic Cells.” *Cancer Cell*.

Ruffell, Brian, and Lisa M. Coussens. 2015. “Macrophages and Therapeutic Resistance in Cancer.” *Cancer Cell*.

Ryan, David P, Theodore S Hong, and Nabeel Bardeesy. 2014. “Pancreatic Adenocarcinoma.” *The New England journal of medicine* 371(11): 1039–49.

Satoh, Takashi et al. 2010. “The Jmjd3-Irf4 Axis Regulates M2 Macrophage Polarization and Host Responses against Helminth Infection.” *Nature Immunology*.

Schafer, Dorothy P. et al. 2012. “Microglia Sculpt Postnatal Neural Circuits in an Activity and Complement-Dependent Manner.” *Neuron*.

Schindler, C, and J E Jr Darnell. 1995. “Transcriptional Responses to Polypeptide Ligands: The JAK-STAT Pathway.” *Annual review of biochemistry* 64: 621–51.

Shiao, Stephen L. et al. 2015. “T H 2-Polarized CD4 + T Cells and Macrophages Limit Efficacy of Radiotherapy.” *Cancer Immunology Research*.

Shrivastava, Richa et al. 2018. “Oncostatin M Upregulates HIF-1α in Breast Tumor Associated Macrophages Independent of Intracellular Oxygen Concentration.” *Life Sciences*.

Sica, Antonio, Tiziana Schioppa, Alberto Mantovani, and Paola Allavena. 2006. “Tumour-Associated Macrophages Are a Distinct M2 Polarised Population Promoting Tumour Progression: Potential Targets of Anti-Cancer Therapy.” *European Journal of Cancer*.

Siegel, Rebecca L, Kimberly D Miller, and Ahmedin Jemal. 2017. “Cancer Statistics, 2017.” *CA: a cancer journal for clinicians* 67(1): 7–30.

Silberer, Jutta, Gabriele Ihorst, and Matthias Volkmar Kopp. 2008. “Cytokine Levels in Supernatants of Whole Blood and Mononuclear Cell Cultures in Adults and Neonates Reveal Significant Differences with Respect to Interleukin-13 and Interferon-Gamma.” *Pediatric Allergy and Immunology*.

Sipos, B. et al. 2009. “Pancreatic Intraepithelial Neoplasia Revisited and Updated.” *Pancreatology*.

Smith, Andrew M. et al. 2009. “Disordered Macrophage Cytokine Secretion Underlies Impaired Acute Inflammation and Bacterial Clearance in Crohn’s Disease.” *Journal of Experimental Medicine*.

Smith, Logan K. et al. 2018. “Interleukin-10 Directly Inhibits CD8+ T Cell Function by Enhancing N-Glycan Branching to Decrease Antigen Sensitivity.” *Immunity*.

Spear, Paul, Amorette Barber, Agnieszka Rynda-Apple, and Charles L Sentman. 2012. “Chimeric Antigen Receptor T Cells Shape Myeloid Cell Function within the Tumor Microenvironment through IFN-Gamma and GM-CSF.” *Journal of immunology (Baltimore, Md. : 1950)*.

Stein, Michael, Satish Keshav, Neil Harris, and Siamon Gordon. 1992. “Interleukin 4 Potently Enhances Murine Macrophage Mannose Receptor Activity: A Marker of Alternative Immunologic Macrophage Activation.” *Journal of Experimental Medicine*.

Stolarski, Bartosz et al. 2010. “IL-33 Exacerbates Eosinophil-Mediated Airway Inflammation.” *The Journal of Immunology*.

Su, Shicheng et al. 2018. “Immune Checkpoint Inhibition Overcomes ADCP-Induced Immunosuppression by Macrophages.” *Cell*.

Sun, Hong Li et al. 2012. “Increased Frequency and Clinical Significance of Myeloidderived Suppressor Cells in Human Colorectal Carcinoma.” *World Journal of Gastroenterology*.

Tada, Kohei et al. 2016. “Pretreatment Immune Status Correlates with Progression-Free Survival in Chemotherapy- Treated Metastatic Colorectal Cancer Patients.” *Cancer Immunology Research*.

Takahashi, K., F. Yamamura, and M. Naito. 1989. “Differentiation, Maturation, and Proliferation of Macrophages in the Mouse Yolk Sac: A Light-Microscopic, Enzyme-Cytochemical, Immunohistochemical, and Ultrastructural Study.” *Journal of Leukocyte Biology*.

Takaoka, Akinori et al. 2005. “Integral Role of IRF-5 in the Gene Induction Programme Activated by Toll-like Receptors.” *Nature*.

Takenaka, Katsuto et al. 2007. “Polymorphism in Sirpa Modulates Engraftment of Human Hematopoietic Stem Cells.” *Nature Immunology*.

Tariq, Muhammad et al. 2017. “Gefitinib Inhibits M2-like Polarization of Tumorassociated Macrophages in Lewis Lung Cancer by Targeting the STAT6 Signaling Pathway.” *Acta Pharmacologica Sinica*.

Toshchakov, Vladimir et al. 2002. “TLR4, but Not TLR2, Mediates IFN-Beta-Induced STAT1alpha/Beta-Dependent Gene Expression in Macrophages.” *Nature immunology* 3(4): 392–98.

Traves, Paqui G et al. 2012. “Relevance of the MEK/ERK Signaling Pathway in the Metabolism of Activated Macrophages: A Metabolomic Approach.” *Journal of immunology (Baltimore, Md. : 1950)* 188(3): 1402–10.

Umansky, Viktor, Carolin Blattner, Christoffer Gebhardt, and Jochen Utikal. 2016. “The Role of Myeloid-Derived Suppressor Cells (MDSC) in Cancer Progression.” *Vaccines*.

Vats, Divya et al. 2006. “Oxidative Metabolism and PGC-1β Attenuate Macrophage-Mediated Inflammation.” *Cell Metabolism*.

Wang, Jinhu, and Jianhong Yang. 2016. “Identification of CD4+CD25+CD127- Regulatory t Cells and CD14+HLA-DR-/Low Myeloid-Derived Suppressor Cells and Their Roles in the Prognosis of Breast Cancer.” *Biomedical Reports*.

Wang, Qiu Shuang et al. 2018. “Interferon-Gamma Induces Autophagy-Associated Apoptosis through Induction of CPLA2-Dependent Mitochondrial ROS Generation in Colorectal Cancer Cells.” *Biochemical and Biophysical Research Communications*.

Wang, Ting et al. 2017. “HIF1 α -Induced Glycolysis Metabolism Is Essential to the Activation of Inflammatory Macrophages.” *Mediators of Inflammation*.

Wang, Yijie et al. 2007. “The Role of the NADPH Oxidase Complex, P38 MAPK, and Akt in Regulating Human Monocyte/Macrophage Survival.” *American journal of respiratory cell and molecular biology* 36(1): 68–77.

Witkiewicz, Agnieszka K. et al. 2015. “Whole-Exome Sequencing of Pancreatic Cancer Defines Genetic Diversity and Therapeutic Targets.” *Nature Communications*.

Woollard, Kevin J, and Frederic Geissmann. 2010. “Monocytes in Atherosclerosis: Subsets and Functions.” *Nature reviews. Cardiology* 7(2): 77–86.

Wynn, Thomas A., and Luke Barron. 2010. “Macrophages: Master Regulators of Inflammation and Fibrosis.” *Seminars in Liver Disease*.

Xu, Feng, and Steven L. Teitelbaum. 2013. “Osteoclasts: New Insights.” *Bone Research*.

Youn, Je-In et al. 2012. “Characterization of the Nature of Granulocytic Myeloid-Derived Suppressor Cells in Tumor-Bearing Mice.” *Journal of Leukocyte Biology*.

Yu, Wenfeng et al. 2012. “Macrophage Proliferation Is Regulated through CSF-1 Receptor Tyrosines 544, 559, and 807.” *Journal of Biological Chemistry*.

Zea, Arnold H. et al. 2005. “Arginase-Producing Myeloid Suppressor Cells in Renal Cell Carcinoma Patients: A Mechanism of Tumor Evasion.” *Cancer Research*.

Zhang, Aibin et al. 2017. “Cancer-Associated Fibroblasts Promote M2 Polarization of Macrophages in Pancreatic Ductal Adenocarcinoma.” *Cancer Medicine*.

Zhang, Yan et al. 2013. “ROS Play a Critical Role in the Differentiation of Alternatively Activated Macrophages and the Occurrence of Tumor-Associated Macrophages.” *Cell Research*.

Zhang, Yifan, Shuai Gao, Jun Xia, and Feng Liu. 2018. “Hematopoietic Hierarchy – An Updated Roadmap.” *Trends in Cell Biology*.

Zhu, Yu et al. 2014. “CSF1/CSF1R Blockade Reprograms Tumor-Infiltrating Macrophages and Improves Response to T-Cell Checkpoint Immunotherapy in Pancreatic Cancer Models.” *Cancer research* 74(18): 5057–69.

Zhu Yu et al. 2017. “Tissue-Resident Macrophages in Pancreatic Ductal Adenocarcinoma Originate from Embryonic Hematopoiesis and Promote Tumor Progression.” *Immunity*.

Zou, Weiping, Jedd D. Wolchok, and Lieping Chen. 2016. “PD-L1 (B7-H1) and PD-1 Pathway Blockade for Cancer Therapy: Mechanisms, Response Biomarkers, and Combinations.” *Science Translational Medicine*.

Danksagung

An dieser Stelle gilt mein Dank zahlreichen Personen für Ihre Unterstützung während dieser Arbeit:

Zuallererst bedanke ich mich bei Prof. Jens Siveke für die Vergabe dieses spannenden Forschungsthemas, sowie für die finanzielle und wissenschaftliche Unterstützung und die Möglichkeit meine Arbeit in seinem Institut durchzuführen.

Des Weiteren bedanke ich mich bei den beiden Gutachtern für Ihr Mitwirken und bei Herrn Prof. Bauer und Herrn Prof. Scheffler für Ihr Mitwirken im Thesis Advisory Committee.

Ein spezieller Dank gilt auch Dr. Phyllis Cheung und Dr. Sven Liffers und Daniel Picard, die für mich in jeglicher Lage als Ansprechpartner mit einer helfenden Hand zur Verfügung standen und immer ein offenes Ohr für Fragen und Probleme hatten.

Des Weiteren bedanke ich mich bei meinen Mit-PhD Studenten und Konstantinos Savvatakis für die hervorragende Arbeitsathmosphäre und die zahlreichen Erinnerungen, die ich mit dieser Zeit assoziieren werde.

Zu allerletzt möchte ich mich bei meiner Familie und meinen Freunden bedanken, die mir in allen Zeiten Rückhalt und Vertrauen geschenkt hat.

Curriculum Vitae

Der Lebenslauf ist in der Online-Version aus Gründen des Datenschutzes nicht enthalten.

Der Lebenslauf ist in der Online-Version aus Gründen des Datenschutzes nicht enthalten.

Der Lebenslauf ist in der Online-Version aus Gründen des Datenschutzes nicht enthalten.

Erklärungen

Erklärung:

Hiermit erkläre ich, gem. § 7 Abs. (2) d) + f) der Promotionsordnung der Fakultät für Biologie zur Erlangung des Dr. rer. nat., dass ich die vorliegende Dissertation selbständig verfasst und mich keiner anderen als der angegebenen Hilfsmittel bedient, bei der Abfassung der Dissertation nur die angegeben Hilfsmittel benutzt und alle wörtlich oder inhaltlich übernommenen Stellen als solche gekennzeichnet habe.

Essen, den _____ _____

Erklärung:

Hiermit erkläre ich, gem. § 7 Abs. (2) e) + g) der Promotionsordnung der Fakultät für Biologie zur Erlangung des Dr. rer. nat., dass ich keine anderen Promotionen bzw. Promotionsversuche in der Vergangenheit durchgeführt habe und dass diese Arbeit von keiner anderen Fakultät/Fachbereich abgelehnt worden ist.

Essen, den _____ _____

Erklärung:

Hiermit erkläre ich, gem. § 6 Abs. (2) g) der Promotionsordnung der Fakultät für Biologie zur Erlangung der Dr. rer. nat., dass ich das Arbeitsgebiet, dem das Thema „Exploring Tumor-Associated Macrophage Heterogeneity and Their Response to MEK Inhibition in Pancreatic Ductal Adenocarcinoma“ zuzuordnen ist, in Forschung und Lehre vertrete und den Antrag v*on* Herrn Christian Neander befürworte und die Betreuung auch im Falle eines Weggangs, wenn nicht wichtige Gründe dem entgegenstehen, weiterführen werde.

_____

Name des Mitglieds der Universität Duisburg-Essen in Druckbuchstaben

Essen, den _____ _____

Unterschrift eines Mitglieds der Universität Duisburg-Essen